Systematic analysis of inelastic alpha scattering off self-conjugate $A = 4n$ nuclei

Satoshi Adachi

Doctoral Dissertation

Department of Physics, Kyoto University

January, 2018

Abstract

Strength distributions in excitation-energy spectra of atomic nuclei provide insights into the nuclear structure because they directly reflect nuclear wave functions. The multipole decomposition analysis (MDA) for the inelastic alpha scattering is very useful to determine the strength distribution in excitation-energy region where several states overlap each other, and widely used to study the nuclear incompressibility and the cluster structures in nuclei. However, the reliability of the MDA was shaken by the puzzle of the missing monopole strength in ^{12}C.

Therefore, it is very important to examine and solve this puzzle of the inelastic alpha scattering, but no systematic measurement of the inelastic alpha scattering to examine the reliability of the theoretical calculation used in the MDA has been carried out until now. In the present work, we systematically measured the cross sections of the inelastic alpha scattering at E_α = 130 and 386 MeV exciting low-lying discrete states in ^{12}C, ^{16}O, ^{20}Ne, ^{24}Mg, ^{28}Si and ^{40}Ca for the first time. In addition, the comparison of the measured cross sections with the "parameter-free" distorted-wave Born-approximation (DWBA) calculation was carried out. All of the adjustable parameters in the DWBA calculation were determined by the electromagnetic transition strengths and the elastic alpha scattering, therefore there is no room for so-called "the puzzle of missing monopole strength" if the consistency between the measured cross sections and the present DWBA calculations is confirmed.

It was found that the DWBA calculation with the density-independent effective αN interaction at E_α = 386 MeV was better than that with the density-dependent effective αN interaction, and thus the inadequate density dependence in the effective αN interaction caused so-called "puzzle of missing monopole strength" by overestimating the cross sections for the $\Delta L = 0$ transition. This puzzle was not specific to the Hoyle state in ^{12}C but universally observed in all of the $\Delta L = 0$ transitions. We also studied ambiguities of the DWBA calculation from the distorting potentials, phenomenological interaction, transition densities, and coupled-channel effects.

The present results should provide the unique and important information for theoretical studies to develop a new reliable αN interaction.

Contents

Chapter 1

Introduction

1.1 Inelastic alpha scattering as an useful probe to examine nuclear structures

Strength distributions in excitation-energy spectra of atomic nuclei provide insights into the nuclear structure because they directly reflect nuclear wave functions. An excitation strength is fundamentally the overlap between wave functions of ground and excited states, and an energy is an eigenvalue of a nuclear Hamiltonian associated with the wave function. The excitation strength and energy are experimental observables, and can be directly compared with theoretical calculations of the nuclear structures. Therefore, the determination of the strength distribution is important to study the nuclear structure. For example, the strength distributions of the isoscalar monopole transition in which the transferred angular momentum (ΔL), spin (ΔS), and isospin (ΔT) are zero provide important information on the incompressibility of the nuclear matter [1–10] and the nuclear cluster structures [11–13].

In order to deduce the strength distribution in atomic nuclei, several experimental probes are proposed and utilized. Inelastic electron scattering is one of the useful probes to determine the excitation strength distribution [14]. Since there is little theoretical ambiguity in the interpretation of the experimental data obtained by electromagnetic probes due to the well-known property of the electromagnetic interaction, the inelastic electron scattering is very useful for measuring the excitation energies and strengths to the discrete states. However, the inelastic electron scattering induces transitions with various spin, parity, and isospin transfers, and thus this feature makes difficult to explore

excited states and to determine their spins, parities, and isospins in excitation-energy region where several states overlap each other. The typical excitation energies of low-lying discrete states are less than 10 MeV below particle-decay thresholds. The isoscalar giant monopole resonances (see Sec. 1.2.1) are known to appear around $80A^{-1/3}$ MeV with a width of several MeV [15], and the alpha condensed states (see Sec. 1.2.2) are predicted to appear at a few-MeV above the $n\alpha$ decay threshold in the self-conjugate $A = 4n$ nuclei, for example around 33 MeV in ^{24}Mg.

In contrast to the inelastic electron scattering, inelastic alpha scattering is useful in such excitation-energy region. The inelastic alpha scattering has selectivity to isoscalar natural-parity transitions where transferred spin and isospin are $\Delta S = 0$ and $\Delta T = 0$ since both spin and isospin of the alpha particle are zero. Therefore, the inelastic alpha scattering at $E_\alpha > 100$ MeV has been extensively measured to extract the strength distribution of the isoscalar natural-parity transitions at KVI in the Netherlands ($E_\alpha = 120$ MeV) [1, 2], at Texus A&M University in the United States ($E_\alpha = 96$–240 MeV) [3–5], and at the Research Center for Nuclear Physics (RCNP), Osaka University in Japan ($E_\alpha = 386$ MeV) [6–13, 16, 17]. The reaction mechanism of the inelastic alpha scattering is relatively simple, and the cross sections are reasonably reproduced by a simple folding-model calculation, and approximately proportional to the relevant nuclear transition strengths. The angular distribution of the cross sections depends on the transferred angular momentum, but is not sensitive to details of nuclear wave functions. Therefore, the multipole decomposition analysis (MDA) works well to obtain the strength distribution of the isoscalar natural-parity excitations even from continuous excitation-energy spectra where many states with large widths overlap each other if the theoretical calculation correctly describes the measured cross sections.

Figure 1.1 shows the cross sections for the ^{208}Pb(α, α') reaction at $E_\alpha = 386$ MeV calculated by the distorted-wave Born-approximation (DWBA) calculation with the single folding-model potential assuming that a single state at $E_x = 14.5$ MeV exhausts the total energy-weighted sum-rule (EWSR) strength. Experimental double differential cross sections $[d^2\sigma/d\Omega dE_x]^{\rm exp}$ are fitted by the calculated cross sections of transitions with various transferred angular momenta $[d^2\sigma/d\Omega dE_x]^{\rm DWBA}_{\Delta L}$ to search for the best parameters $a_{\Delta L}(E_x)$ in the MDA as,

$$\left[\frac{d^2\sigma(\theta_{\rm c.m.}, E_x)}{d\Omega dE_x}\right]^{\rm exp} = \sum_{\Delta L} a_{\Delta L}(E_x) \left[\frac{d^2\sigma(\theta_{\rm c.m.}, E_x)}{d\Omega dE_x}\right]^{\rm DWBA}_{\Delta L}. \tag{1.1}$$

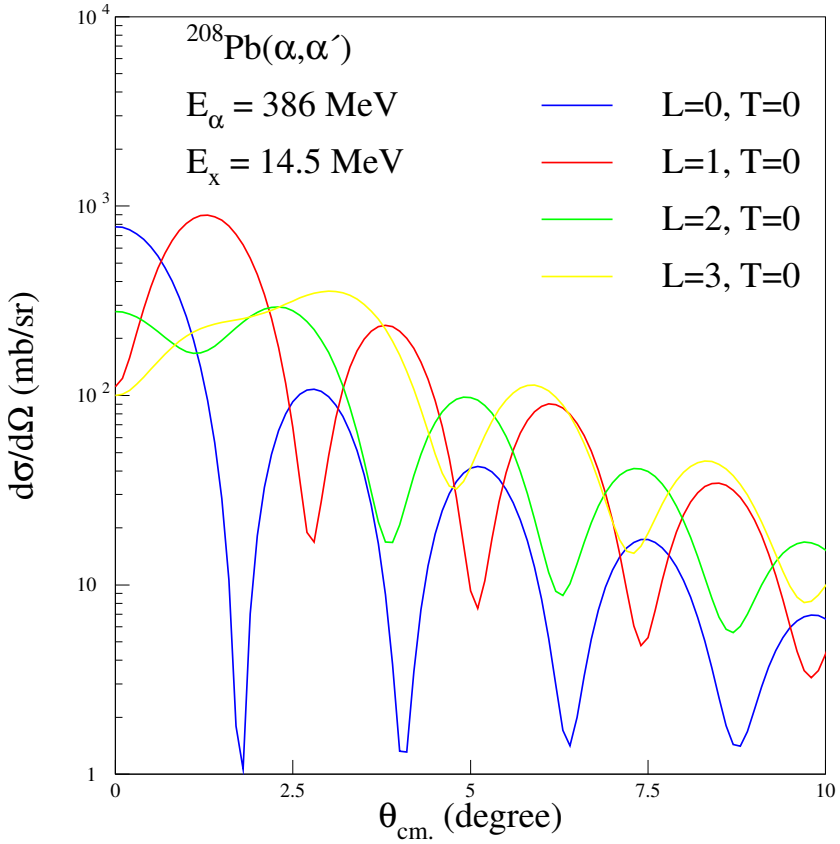

Figure 1.1: The DWBA calculations of the differential cross sections for various transitions in $^{208}\mathrm{Pb}(\alpha, \alpha')$ reaction at $E_\alpha = 386$ MeV. Taken from Fig. 1.3 in Ref. [18]. The blue, red, green, and yellow lines show the angular distribution of the cross sections with different transferred angular momentum ΔL and transferred isospin ΔT, respectively. Note that ΔL and ΔT are denoted by L and T.

The determined $a_{\Delta L}(E_x)$ corresponds to the fraction of the EWSR strength for each transferred angular momentum ΔL, and thus the strength distribution is obtained as a function of the excitation energy. Figure 1.2 shows examples of the MDA for the ^{208}Pb(α, α') reaction in Ref. [18]. The differential cross section at each excitation energy

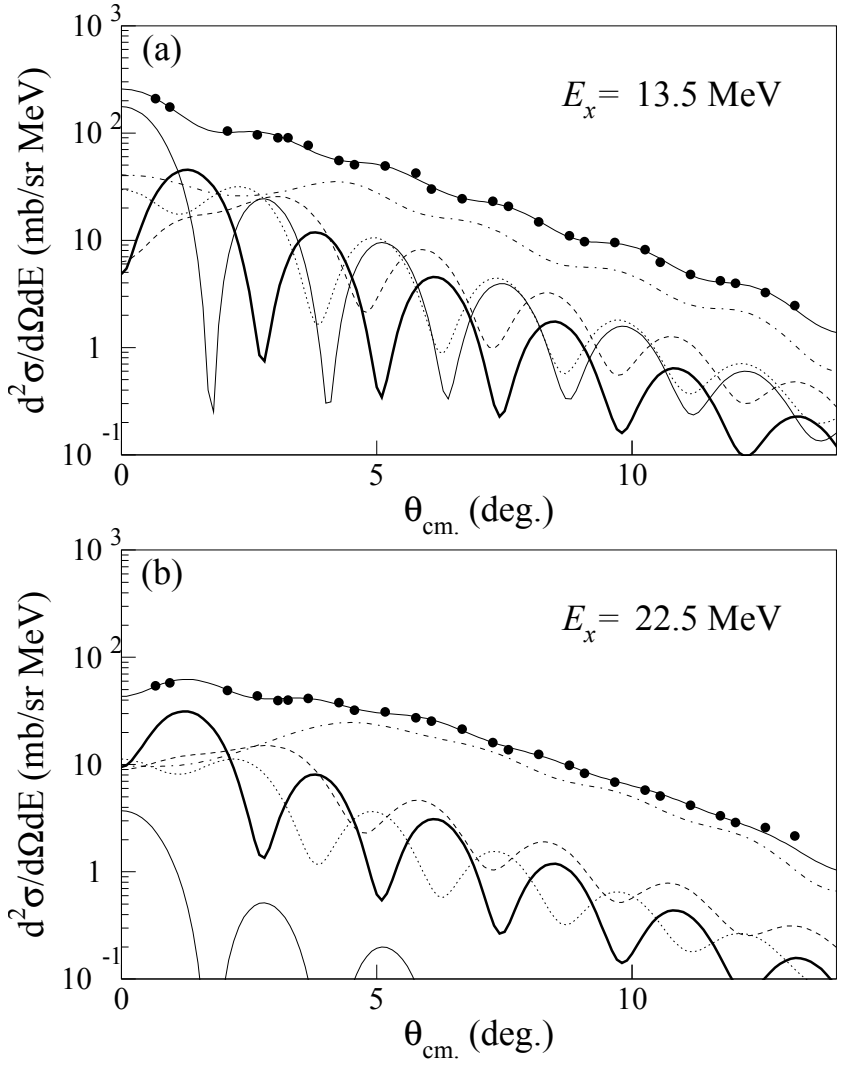

Figure 1.2: Examples of the MDA for the ^{208}Pb(α, α') reaction at $E_\alpha = 386$ MeV. Taken from Fig. 4.5 in Ref. [18]. The solid circles show the experimental cross sections. The solid lines near the measured cross sections are the sum of the calculated DWBA cross sections. The thick and thin-solid, dotted, and dashed curves are the DWBA cross sections for $\Delta L = 1$, $\Delta L = 0$, $\Delta L = 2$, and $\Delta L = 3$, whereas the sum of the cross sections for $\Delta L > 3$ is shown by the dot-dashed line. (a) The result of the MDA at $E_x = 13.5$ MeV. (b) The result of the MDA at $E_x = 22.5$ MeV.

was well reproduced by the sum of the calculated cross sections, and the strength distributions of the isoscalar natural-parity transitions were successfully obtained as shown in Fig. 1.3.

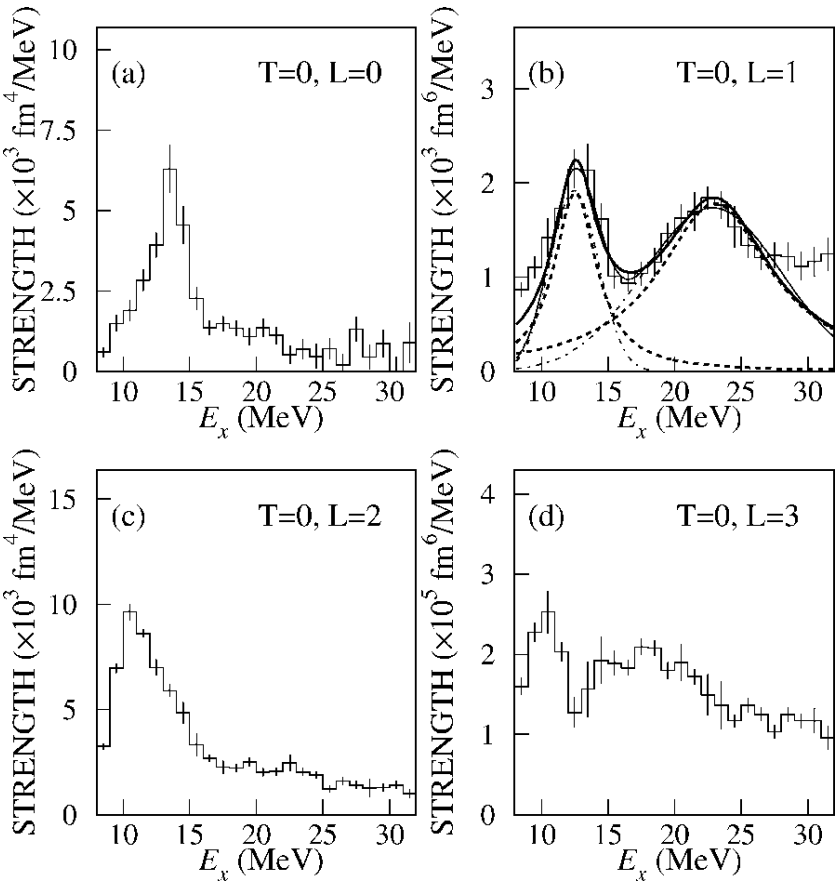

Figure 1.3: Strength distributions for the $\Delta L = 0, 1, 2$ and 3 transitions in ^{208}Pb by the inelastic alpha scattering at $E_\alpha = 400$ MeV. Taken from Fig. 3 in Ref. [19]. Note that ΔL is denoted by L. The lines in (b) show the fit to the strength distribution.

In Secs. 1.2.1 and 1.2.2 we briefly describe several examples of the application of the inelastic alpha scattering to the giant resonances and the cluster structures in nuclei.

1.2 Application of inelastic alpha scattering

1.2.1 Giant resonances in nuclei

The isoscalar giant monopole resonances (ISGMR) and the isoscalar giant dipole resonances (ISGDR) are extensively examined by means of the MDA for the inelastic alpha scattering [3–13, 17, 20]. The strength distributions of the ISGMR and the ISGDR were successfully extracted from the continuous excitation-energy spectra by the MDA, and these analyses precisely determined the nuclear incompressibility of the symmetric nuclear matter [5–7]. Incompressibility of the nuclear matter is of fundamental importance in nuclear physics to define the equation of state for the nuclear matter, which describes a number of interesting phenomena from collective excitations of nuclei to supernova explosions and radii of neutron stars.

The infinite nuclear matter incompressibility K_∞ is defined by the second derivative of the energy per particle E/A with respect to the density ρ at the saturation point $\rho_{\rm nm}$,

$$K_\infty = 9\rho^2 \frac{d^2}{d\rho^2}\left(\frac{h}{\rho}\right)_{\rho=\rho_{\rm nm}}, \tag{1.2}$$

where h is the isoscalar part of the Hamiltonian density for the nuclear matter [21]. The infinite nuclear matter does not exist on earth, therefore K_∞ can not be measured directly. However, the centroid energy of the ISGMR $E_{\rm ISGMR}$ is related to the incompressibility of the finite nucleus K_A as

$$E_{\rm ISGMR} = \sqrt{\frac{\hbar^2 K_A}{m\langle r^2\rangle_m}}, \tag{1.3}$$

where m is the nucleon mass and $\langle r^2\rangle_m$ is the mean square mass radius of the ground state, and the incompressibility of the finite nucleus can be parameterized using K_A as follows [22],

$$K_A = K_\infty + K_{\rm surf}A^{-1/3} + K_\tau[(N-Z)/A]^2 + K_{\rm Coul}Z^2A^{-4/3}. \tag{1.4}$$

The nuclear matter incompressibility K_∞ was previously deduced from the systematic measurements of the K_A values in various medium-heavy nuclei. For example, K_A in ^{208}Pb was determined from $E_{\rm ISGMR}$ according to Eq. (1.3), and $E_{\rm ISGMR}$ in ^{208}Pb was obtained as the averaged excitation energy of the isoscalar monopole-strength distribution

shown in Fig. 1.3(a) which exhausted most of the EWSR strength.

Nowadays, the K_∞ is theoretically estimated from various energy functionals of the nuclear matter with different parameters, and the ISGMR strength distributions are also calculated for different energy functionals with a self-consistent RPA framework [23, 24]. The energy functional which gives the best description of the ISGMR strength distribution is considered to be the most appropriate, and it gives the reliable value of K_∞. The presently accepted value of K_∞ is 240 ± 10 MeV [25–27] as introduced in Ref. [28].

The asymmetry term K_τ in Eq. (1.4) is also important in addition to K_∞ because K_τ is crucial for the asymmetric nuclear matter like neutron stars. The inelastic alpha scattering off the Sn isotopes provides information for K_τ [7]. Figure 1.4 shows the strength distributions of the isoscalar monopole transition obtained for the Sn isotopes with the MDA. The difference $K_A - K_{\rm Coul} Z^2 A^{-4/3}$ for the Sn isotopes as a function of

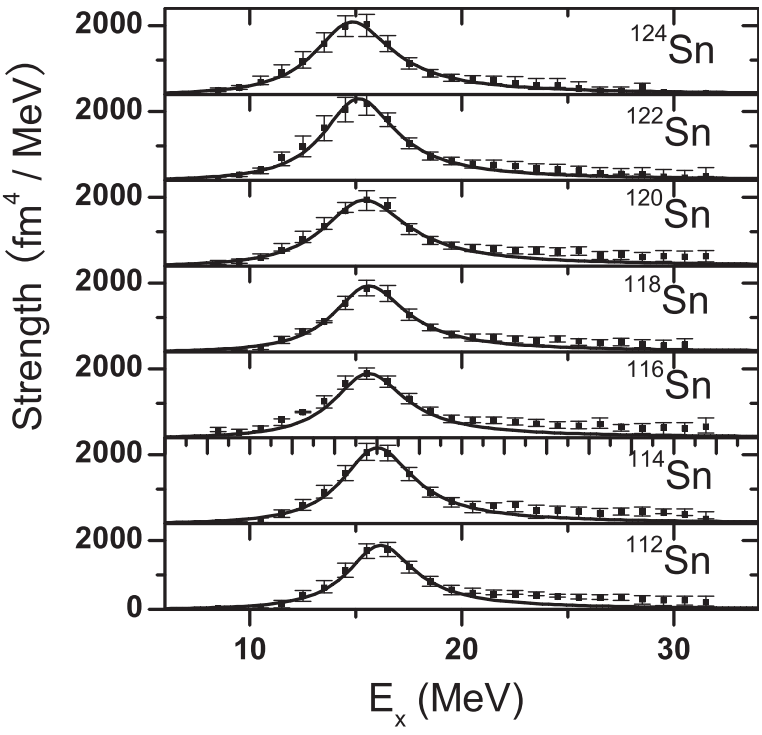

Figure 1.4: Strength distributions obtained by inelastic alpha scattering of the Sn isotopes at $E_\alpha = 400$ MeV. Taken from Fig. 2 in Ref. [7]. Error bars represent the uncertainty in the MDA. The solid lines show Lorentzian fits to the data.

the asymmetry parameter $[(N - Z)/A]$ are shown in Fig. 1.5. The values of K_A was

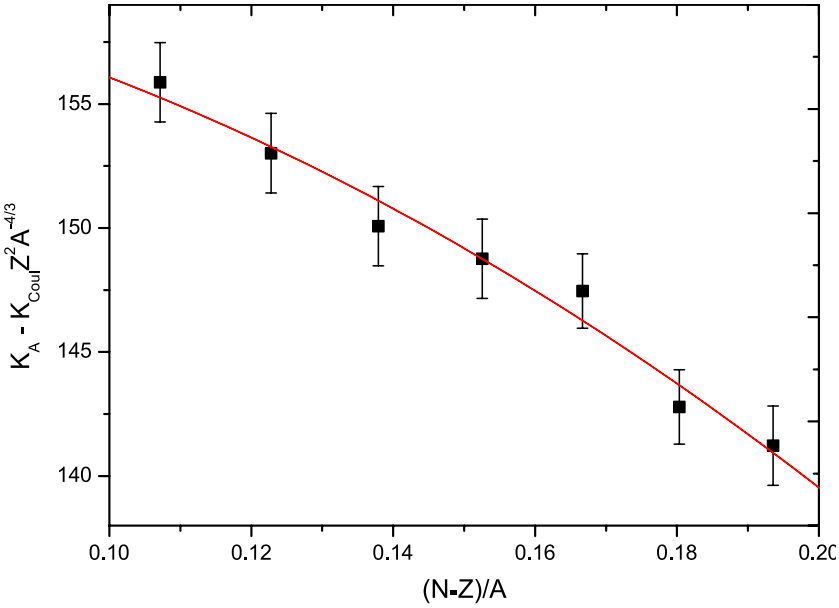

Figure 1.5: Systematics of the difference $K_A - K_{\rm Coul}Z^2A^{-4/3}$ in the Sn isotopes as a function of "asymmetry parameter" $[(N-Z)/A]$. $K_{\rm Coul}$ was fixed at -5.2 MeV [21]. Taken from Fig. 4 in Ref. [7].

derived from the strength distribution of the isoscalar monopole transition, and $K_{\rm Coul}$ was fixed at -5.2 MeV. As expressed in Eq. (1.4), the term with K_∞ is independent from the mass number A, and the surface term with $K_{\rm surf}$ is also almost independent from A because the mass range of the measured Sn isotopes is as narrow as $A = 114$–124. Therefore, $K_A - K_{\rm Coul}Z^2A^{-4/3}$ approximately has a quadratic relationship with the asymmetry parameter. Finally, the value of $K_\tau = -550 \pm 100$ MeV was obtained in Ref. [7].

In addition to the stable nuclei, inelastic alpha scattering off unstable nuclei comes to be measured recently [29, 30] because the ISGMR in unstable nuclei attracts interest in nuclear physics to examine the nuclear incompressibility of the asymmetric nuclear matter.

As described above, the reliable determination of the strength distribution of the isoscalar monopole transition in stable and unstable nuclei by the MDA of the inelastic alpha scattering is crucial to establish the equation of state for the nuclear matter.

1.2.2 Cluster structure in nuclei

Alpha clustering phenomena in atomic nuclei have been studied for long time as an interesting research field in nuclear physics since the Gamow's α-decay theory [31, 32]. Many theoretical and experimental efforts have been devoted since 1930, although there still remain many hot topics to be discussed from both the experimental and theoretical sides.

The Bloch-Brink model developed in 1950s and 1960s is one of the famous microscopic theories to describe the cluster structures [33]. This model was originated from the consideration for the 2α cluster system in Ref. [34], and is generalized for the multi-α system. The multi-α system is described as an antisymmetrized wave function consisting of wave functions of alpha clusters at different position, and each alpha -cluster wave function consists of four Gaussian single-particle wave functions at the same position. Moreover, Ikeda *et al.* proposed that the cluster structures would appear near alpha-decay threshold energies. This is known as "threshold rule" [35] and schematically represented by Ikeda diagram as shown in Fig. 1.6.

One of the most famous alpha cluster states is the 0_2^+ state at $E_x = 7.65$ MeV in ^{12}C. This excitation energy of 7.65 MeV is only 0.38 MeV above the 3α decay threshold energy in ^{12}C. This state is called as the Hoyle state, and plays a very important role in the nucleosynthesis in the universe [37]. ^{12}C is the doorway nucleus in the heavy-elements synthesis, and ^{12}C is synthesized by the triple α reaction via the Hoyle state. The Hoyle state is formed by the alpha capture reaction following the ^{8}Be formation due to the collision of two alpha particles. ^{12}C is synthesized by the radiative decay of the Hoyle state with a probability of $(\Gamma_\gamma + \Gamma_\pi)/(\Gamma_\alpha + \Gamma_\gamma + \Gamma_\pi) \sim 4{\times}10^{-4}$. The level diagram in ^{12}C is shown in Fig. 1.7

Recently, the MDA for the inelastic alpha scattering is extensively carried out to search for the α cluster states. For example, the missing 2_2^+ state in ^{12}C was found at $E_x = 9.84 \pm 0.04$ MeV in ^{12}C with a width of 1.01 ± 0.15 MeV by the MDA of the ^{12}C(α, α') reaction as shown in Fig. 1.8. Although this 2_2^+ state in ^{12}C was incontrovertibly predicted by the 3α cluster model as an excited state of the Hoyle state [38–40], no experimental attempts to search for this state had been successful for a long time [41–43]. The MDA of the inelastic alpha scattering worked well to extract the $\Delta L = 2$ transition strength in the broad bump around $E_x = 10$ MeV in ^{12}C as seen in Figs. 1.8(c) and (d) and to find the missing 2_2^+ state for the first time.

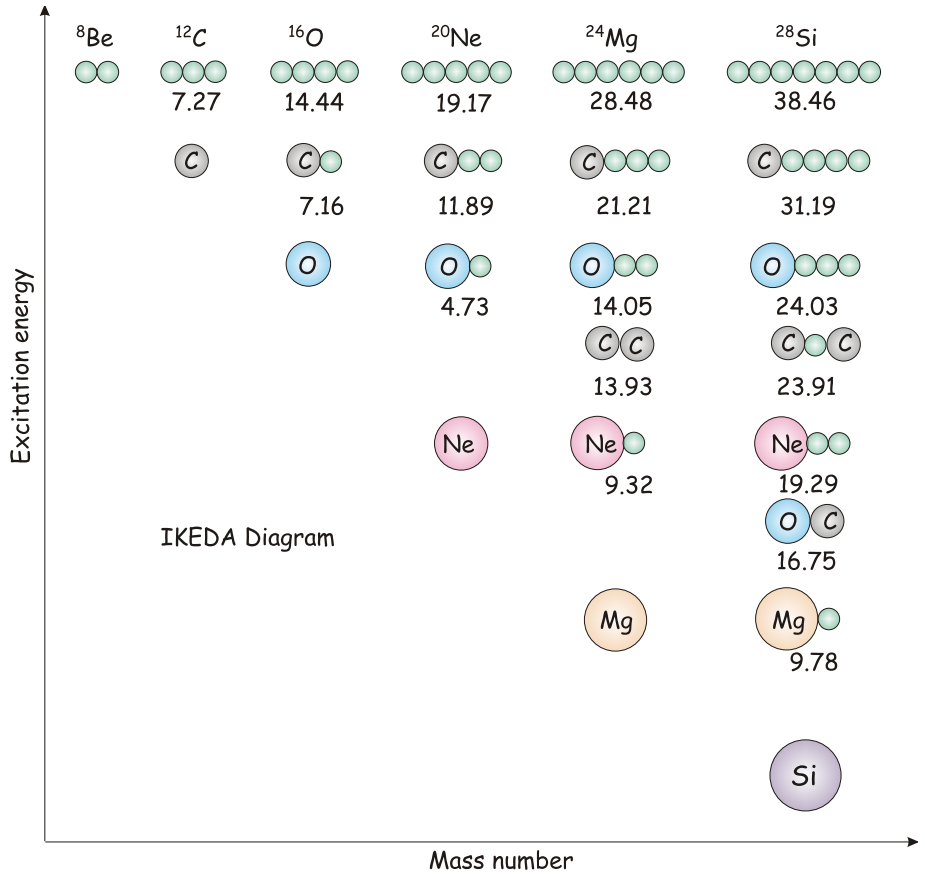

Figure 1.6: Ikeda diagram showing the relation between threshold energy to each decay mode and the cluster structure. Taken from Fig. 1 in Ref. [36]. The small circles without alphabets show alpha particles. The threshold energy to decay to each configuration from the ground state is shown in the unit of MeV below the drawing.

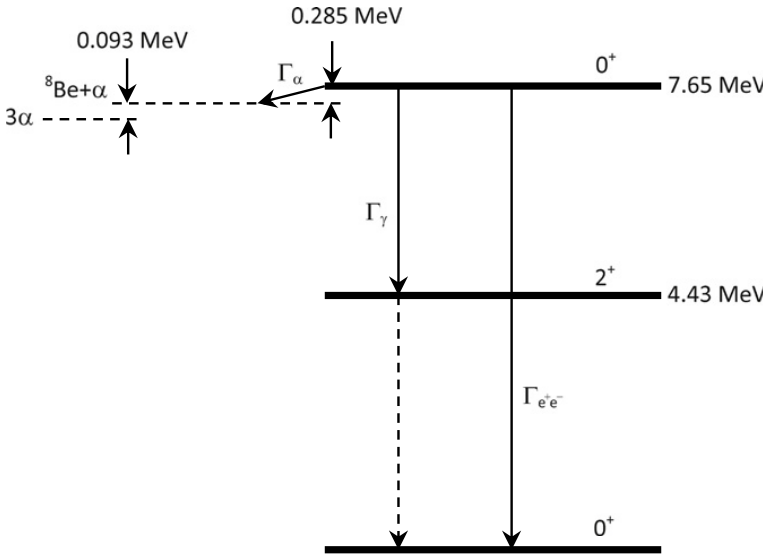

Figure 1.7: Level diagram in ^{12}C related to the triple α reaction. Taken from Fig. 2 in Ref. [36].

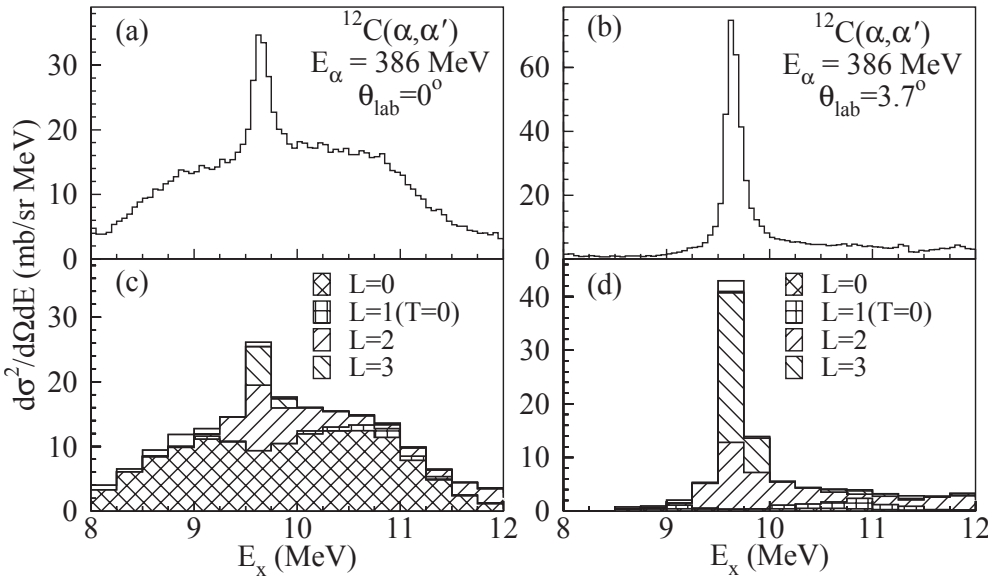

Figure 1.8: Taken from Ref. [16]. (a) and (b) Excitation energy spectra of the ^{12}C(α, α') reaction at $E_\alpha = 386$ MeV at $\theta_{\rm lab} = 0.0°$ and 3.7°, respectively. (c) and (d) Decomposition to the cross sections with various transferred angular momenta by the MDA. A broad bump around 10.0 MeV for $L = 2$ component was observed.

It was pointed out that large isoscalar monopole transition strengths are a signature of cluster excitation in atomic nuclei [44]. This was theoretically explained by using the Bayman-Bohr theorem [45] in Ref. [46]. The clustering degrees of freedom are inherently possessed even by simple shell-model wave functions and can be activated by the monopole excitation. As an example, the Hoyle state, which has a spatially developed 3α cluster structure, is excited with a large isoscalar monopole strength of $B(E0; IS) = 121 \pm 9$ fm^4 [47]. This strength is about three times larger than the single-particle limit in ^{12}C [47]. For ^{24}Mg, several 0^+ states are strongly excited by isoscalar monopole transitions in the inelastic alpha scattering as reported in Ref. [11]. The strength distribution of the isoscalar monopole transition was extracted as shown in Fig. 1.9. Several discrete peaks due to the 0^+ state near the threshold energies for ^{20}Ne+α, ^{12}C+^{12}C, and ^{16}O+2α were observed in the $\Delta L = 0$ strength distribution. Actually, the theoretical calculation suggests these 0^+ states have spatially developed cluster structures [48]. Figure 1.10 shows the theoretical calculation for the strength functions of the isoscalar monopole excitations in ^{24}Mg. The β and γ deformations, the isoscalar transitions, and the many particle-hole configurations in ^{24}Mg are taken into account in the basis set (c) of the wave function. The gray thick line in the right panel shows the strength function smeared by a Lorentzian with a width of 0.8 MeV. The vertical dashed lines indicate cluster decay threshold energies. The smeared strength function shows similar structure to the measured $\Delta L = 0$ strength distribution in the top panel of Fig. 1.9.

Recently it is suggested that the Hoyle state is a 3α condensed state, where the 3 alpha particles are condensed into the lowest s orbit [49]. The authors claimed that this state is a gas-like state of alpha clusters and is akin to the Bose-Einstein condensate. Figure 1.11 shows the theoretically calculated occupation of the alpha-particle orbitals associated with the Hoyle state in ^{12}C compared with the ground state. The occupation probability of the $0s$ (S_1) orbital is more than 70% in the Hoyle state.

It is expected that such alpha condensed states exist not only in ^{12}C but also in other self-conjugate $A = 4n$ nuclei. It was predicted in Ref. [51] that the $n\alpha$ condensed states with $J^\pi = 0^+$ appear above $n\alpha$ decay threshold energies in the heavier self-conjugate $A = 4n$ nuclei up to $n = 10$. Figure 1.12 shows the predicted excited energies and root-mean-square radii of the $n\alpha$ condensed states with $J^\pi = 0^+$ in the self-conjugate $A = 4n$ nuclei.

At present, the candidates of the alpha condensed states are proposed and widely

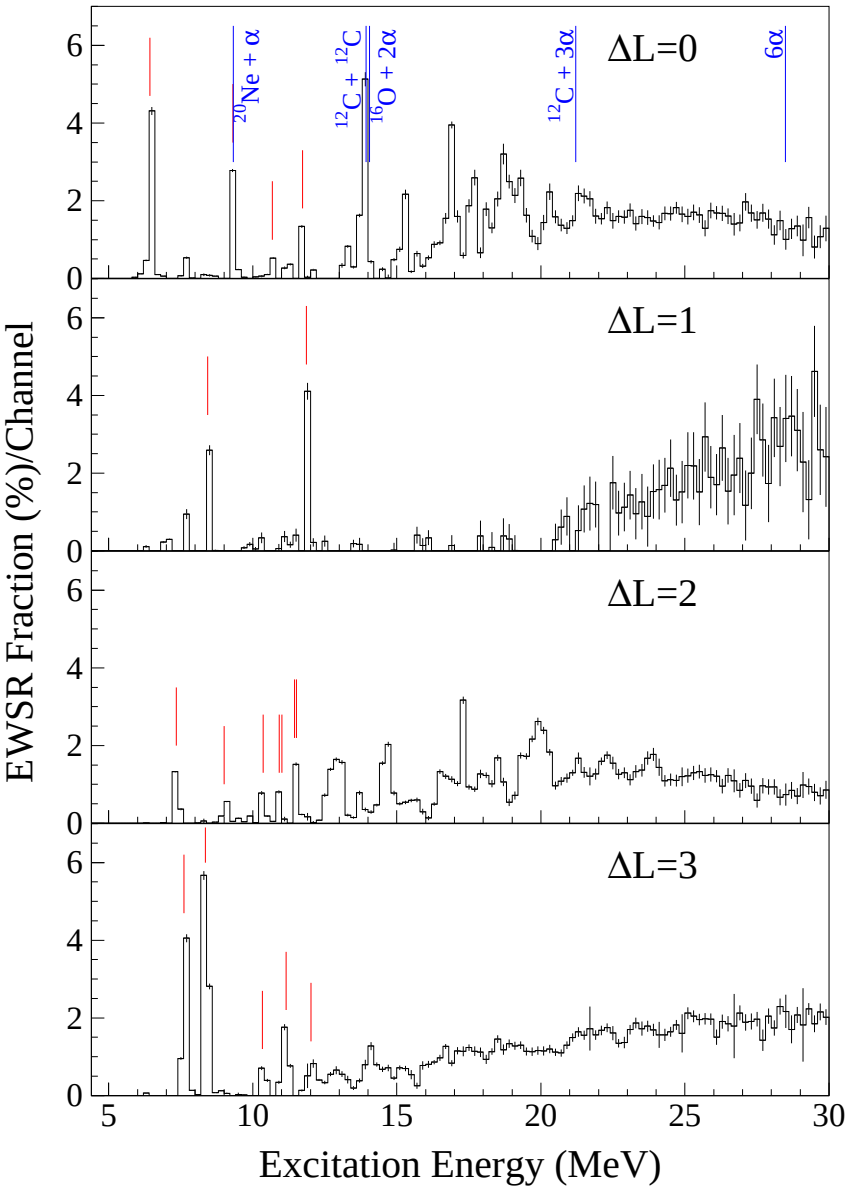

Figure 1.9: Strength distributions for the $\Delta L = 0$–3 transitions obtained from the MDA for the ^{24}Mg(α, α') reaction [11]. Taken from Fig. 3 in Ref. [11]. The blue vertical line with each configuration show the threshold energy to decay into its configuration. The red vertical lines show the excited energies of the known states in ^{24}Mg.

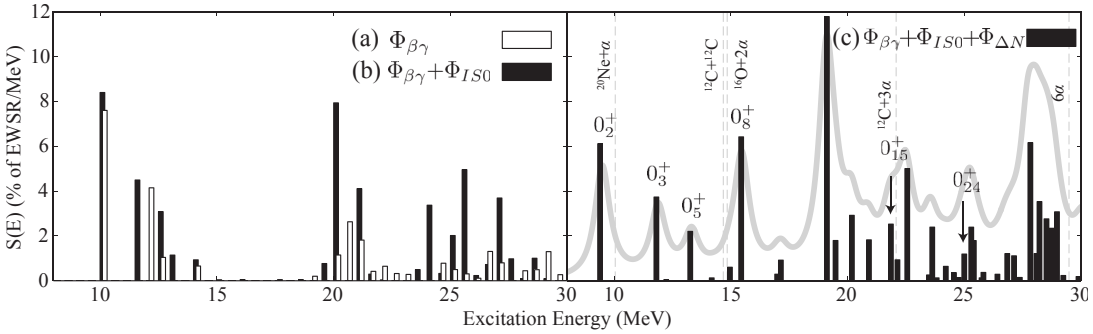

Figure 1.10: Strength functions of the isoscalar monopole excitations in ^{24}Mg calculated in Ref. [48]. Taken from Fig. 2 in Ref. [48]. Three Calculated strength functions (a), (b), and (c) are obtained by different AMD variational wave function. See text and Ref. [48] for more details.

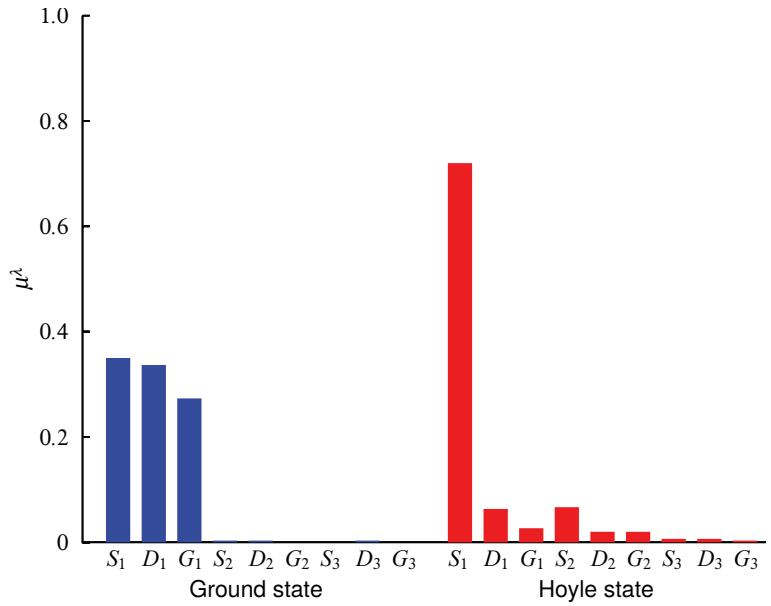

Figure 1.11: Occupation of the alpha-particle orbitals associated with the Hoyle state in ^{12}C compared with the ground state. Taken from Fig. 7 in Ref. [50].

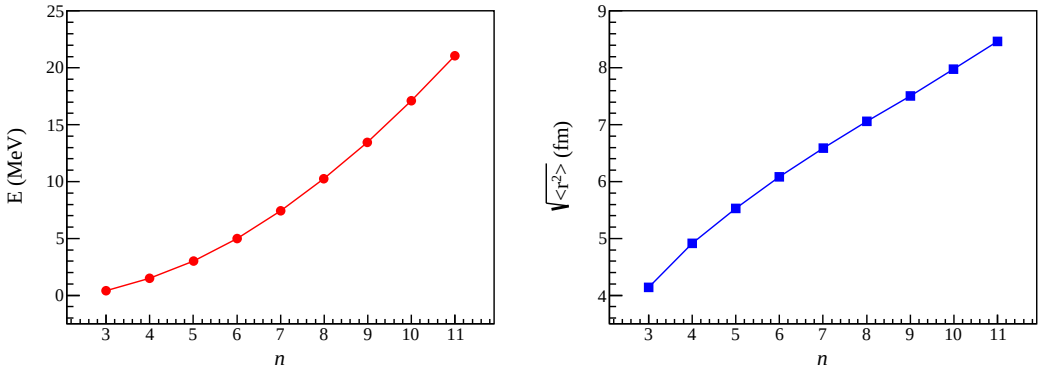

Figure 1.12: The theoretically predicted excited energies (left) and root-mean-square radii (right) of the $n\alpha$ condensed states with $J^\pi = 0^+$ in the self-conjugate $A = 4n$ nuclei. Taken from Fig. 2 in Ref. [51]. The excited energies are measured from the $n\alpha$ decay threshold energies.

accepted in ^{8}Be and ^{12}C only. The ground state in ^{8}Be and the Hoyle state in ^{12}C are successfully described by the alpha condensed wave functions [51, 52]. The alpha condensed states in other nuclei are still being experimentally searched for and much effort is devoted to find out these states [11, 12]. We recently proposed to search for α condensed states in heavier self-conjugate $A = 4n$ nuclei by measuring the isoscalar monopole transition to the highly excited states above the $n\alpha$ decay threshold in the inelastic alpha scattering. The reliable determination of the transition strength of the isoscalar monopole transition for the highly excited states is crucial to search for the α condensed states.

In addition to the alpha condensed states, there are theoretical predictions of the cluster states called "molecular states" to exist, and these states are experimentally searched for. A typical example is reported in ^{10}Be. Several excited states in ^{10}Be are suggested to have a unique α-2n-α configuration. Two excess neutrons play a role of covalent particles in molecular orbits among the two alpha clusters and behave like a valence electron pair bonding two atoms [53–55]. The density distributions of the single-particle wave functions for valence neutrons in the 0^+_1 and 0^+_2 states in ^{10}B are shown in Fig. 1.13. From the experimental point of view, the measurement of the transition strength of the isoscalar monopole transition in ^{10}Be is strongly desired to compare the theoretical prediction with the experiment. However, the inelastic electron scattering off ^{10}Be cannot be measured because ^{10}Be is unstable. A new measurement of the inelastic alpha scattering off ^{10}Be and the MDA of the measured data should be done.

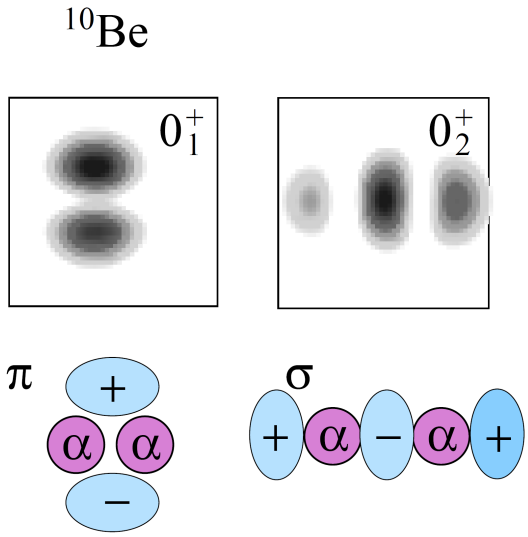

Figure 1.13: Density distributions of the single-particle wave functions for valence neutrons in ^{10}B(0_1^+) and ^{10}B(0_2^+). Schematic figure of the molecular orbitals; π and σ orbitals around the 2α core are also shown at the bottom. Taken from Fig. 3(a) in Ref. [55].

1.3 Missing monopole strength of the Hoyle state

The MDA is established on the assumption that the cross sections of the inelastic alpha scattering are reasonably well described by the DWBA calculation and are approximately proportional to the relevant transition strengths. However, a result contradictory to the linear dependence was reported in the monopole excitation to the Hoyle state from the ground state in ^{12}C. The isoscalar monopole strength determined from the inelastic electron scattering exhausts about 15% of the energy-weighted sum-rule (EWSR) strength [47, 56, 57], but that from the inelastic alpha scattering exhausts as small as 7.6% [20]. This discrepancy is called as "missing monopole strength of the Hoyle state".

The cross sections of the inelastic electron scattering for the Hoyle state was measured over a wide range of the momentum transfer q [56, 57]. From Fig. 1.14, the electromagnetic transition matrix element between the ground state and the Hoyle state in ^{12}C was determined as $M_\pi = 5.37 \pm 0.22$ fm^2 [56]. Recently, the cross sections for the Hoyle state were measured at a very small q region, and the matrix element was updated to be $M_\pi = 5.29 \pm 0.14$ fm^2 as shown in Fig. 1.15 [57]. The black circles and the solid line show the previous experimental data and the global fit to the data. The red solid

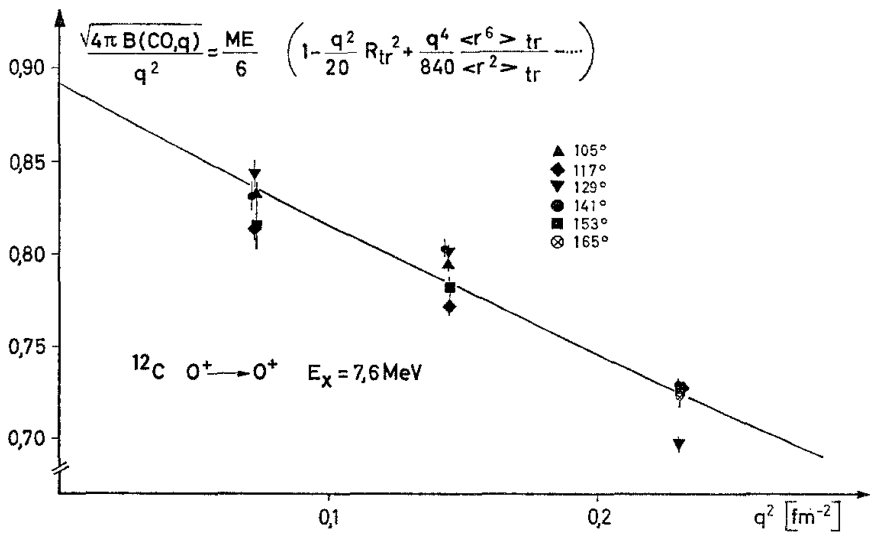

Figure 1.14: The square root of the reduced transition probability $B(C0, q)$ multiplied by $\sqrt{4\pi}/q^2$ as a function of the square of the momentum transfer q [56]. The experimental data were obtained by the inelastic electron scattering at $E = 28$–60 MeV and the scattering angles $\theta_{\rm lab} = 105°$–$165°$. The experimental data and the theoretical calculation fitted to the data are shown by the points and solid line, respectively. Note that the intercept at $q = 0$ corresponds to the electromagnetic matrix element M_π divided by 6.

squares and the dashed line show the new experimental data taken in Ref. [57] and the new fit to the data. The theoretical predictions by different cluster models are shown by the dotted and dash-dotted lines.

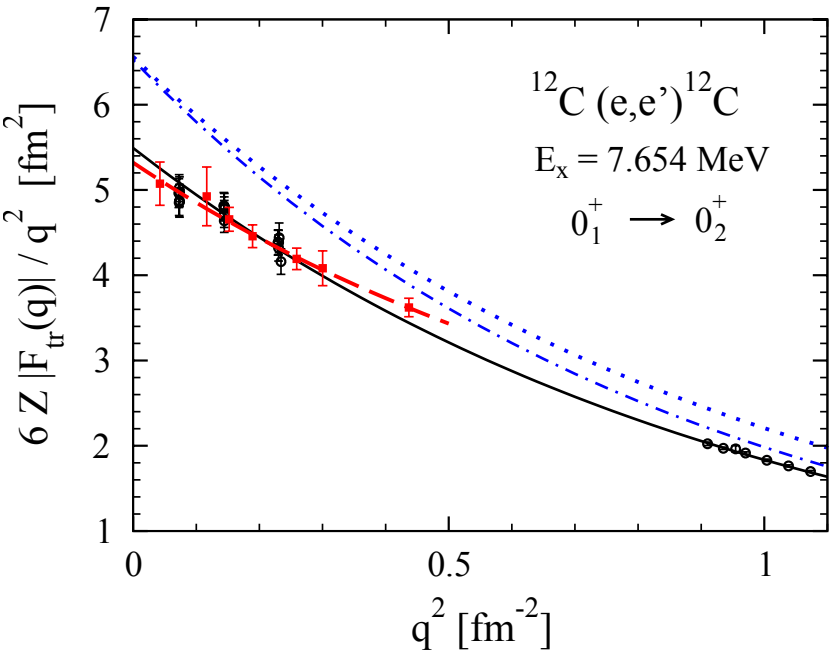

Figure 1.15: The charge transition form factor $F_{tr}(q)$ multiplied by $6Z/q^2$ as a function of the square of the momentum transfer q. Taken from Fig. 4 in Ref. [57]. The experimental data were obtained by the inelastic electron scattering at E = 29–78 MeV and the scattering angles $\theta_{\rm lab}$ = 69°–141°. See text and Ref. [57] for more details. Note that the intercept at $q = 0$ corresponds to the matrix element.

If one state at an excitation energy E_x exhausts 100% of the EWSR strength for the isoscalar monopole transition, the matrix element M_π for the transition follows the relation,

$$E_x|M_\pi|^2 = \frac{\hbar^2}{2m} A\langle r^2\rangle, \tag{1.5}$$

where m, A, and $\langle r^2\rangle$ denotes the mass of the nucleon, the mass number of the considered nucleus, and the square of the charge root-mean-square radius of the nucleus. Therefore, the matrix element $M_\pi = 5.29$ fm^2 corresponds to 14% of the EWSR strength.

The inelastic alpha scattering from ^{12}C at $E_\alpha = 240$ MeV was measured in Ref. [20]. The authors of Ref. [20] performed the DWBA analysis using a macroscopic transition density, and compared the experimental data with the DWBA calculation as shown in

Fig. 1.16. They deduced the Hoyle state exhausts 7.6% of the EWSR strength.

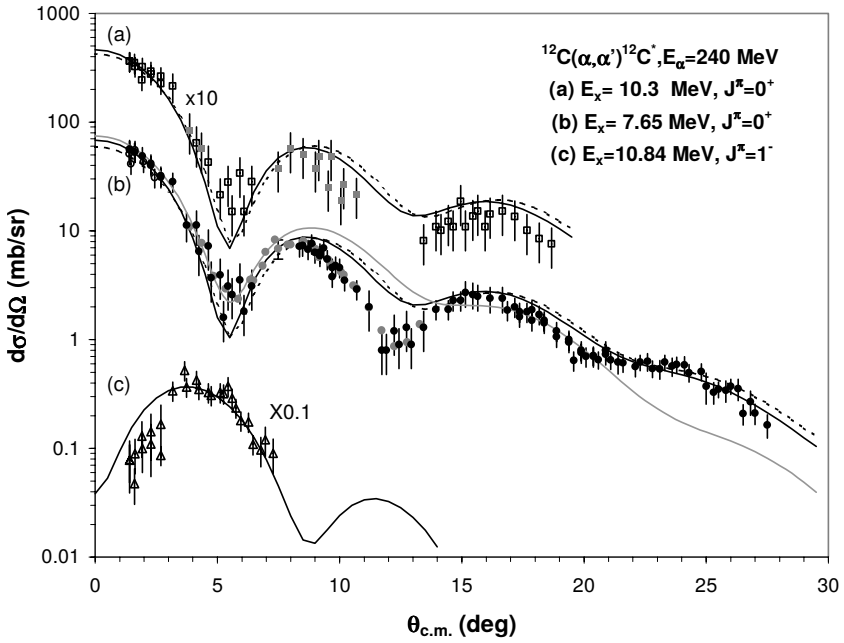

Figure 1.16: The differential cross sections for the $^{12}\mathrm{C}(\alpha, \alpha')$ reaction at $E_\alpha = 240$ MeV compared with the DWBA calculations [20]. Taken from Fig. 8 in Ref. [20]. (b) The solid circles and line represent the experimental data and the DWBA calculation for the Hoyle state at $E_x = 7.65$ MeV, respectively. (a) and (c) for the transition to the 0^+ state at $E_x = 10.3$ MeV and 1^- state at $E_x = 10.84$ MeV, respectively.

In Ref. [58], the authors performed a double folding-model analysis of the inelastic $\alpha + {}^{12}\mathrm{C}$ scattering at $E_\alpha = 104, 139, 172.5$, and 240 MeV using a complex density-dependent interaction (CDJLM interaction, which was constructed on the M3Y-Paris interaction [59]) and the reliable wave functions of the ground and Hoyle states in ^{12}C from 3α resonating group method (RGM) calculation [40]. The monopole excitation strength to the Hoyle state predicted by the 3α RGM calculations is 22.8% of the EWSR strength and close to the strength reported from the inelastic electron scattering [56, 57]. Nevertheless, the calculated cross sections of the inelastic alpha scattering for the Hoyle state using the 3α RGM wave functions were significantly larger than the measured cross section at $E_\alpha = 104$–240 MeV as shown in Figs. 1.17 and 1.18. The authors of Ref. [58] performed both the DWBA and the coupled-channel (CC) calculations at $E_\alpha = 104$, 139, 172.5, and 240 MeV. The dashed and dotted lines in Figs. 1.17 and 1.18 represent the DWBA and CC calculations with 22.8% of the EWSR strength, whereas the solid and

dash-dotted lines represent the DWBA calculation with 6.9% of the EWSR strength and the CC calculation in which the imaginary part of the optical potential was increased to reproduce the experimental data.

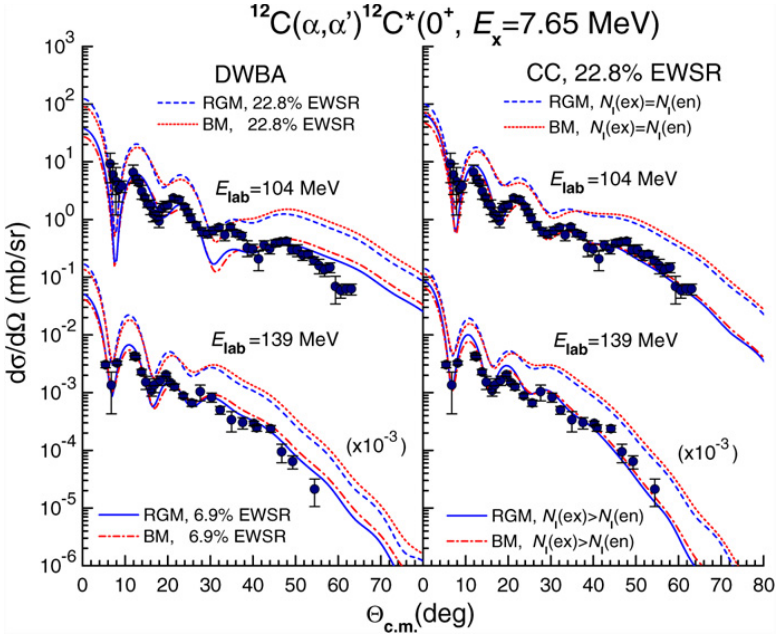

Figure 1.17: The DWBA and CC calculations for the cross section of the $^{12}\mathrm{C}(\alpha,\alpha')$ reaction exciting the Hoyle state at $E_\alpha = 104$ and 139 MeV. The solid circles are the experimental data, whereas the dash, dotted, solid, dash-dotted lines are the theoretical calculations. Taken from Fig. 3 in Ref. [58].

This discrepancy is consistent with the previous results [20] that the excitation strength for the Hoyle state determined by the inelastic alpha scattering is much smaller than that determined by the inelastic electron scattering. In contrast to the Hoyle state, the cross sections to the 2^+_1 state in ^{12}C were well reproduced by the CC calculation at the intermediate energies as shown in Fig. 1.19.

It was claimed in Ref. [58] that this problem is due to the weakly bound structure of the Hoyle state which significantly enhances the absorption in the exit $\alpha+^{12}\mathrm{C}^*(0^+_2)$ channel, and the reaction mechanism of inelastic alpha scattering might strongly couple to the nuclear structure. Therefore, the approximate linear proportional relation between cross sections and relevant transition strengths might not be valid in the analysis of the inelastic alpha scattering. It is a serious problem suggesting that the strength distribution determined by the MDA of the inelastic alpha scattering might not be reliable.

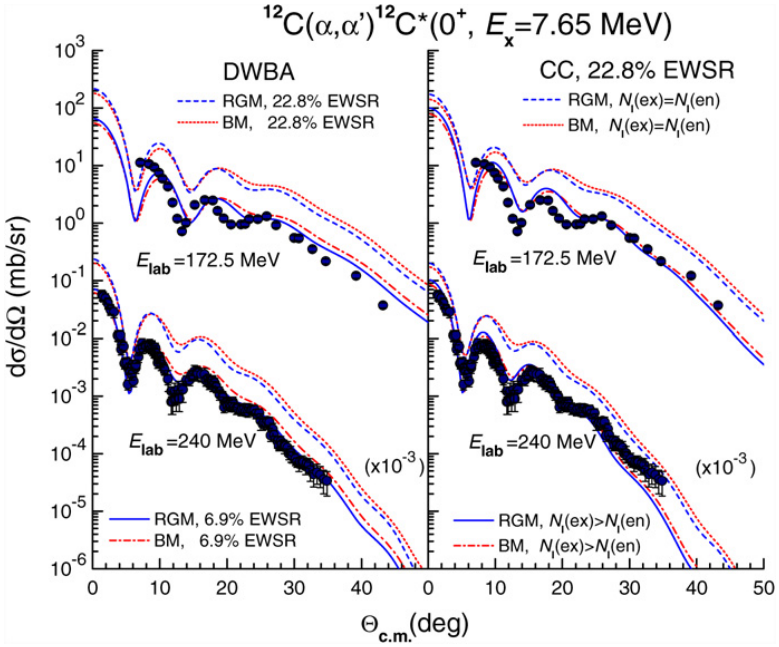

Figure 1.18: Same as Fig. 1.17, but at $E_\alpha = 172.5$ and 240 MeV. Taken from Fig. 4 in Ref. [58].

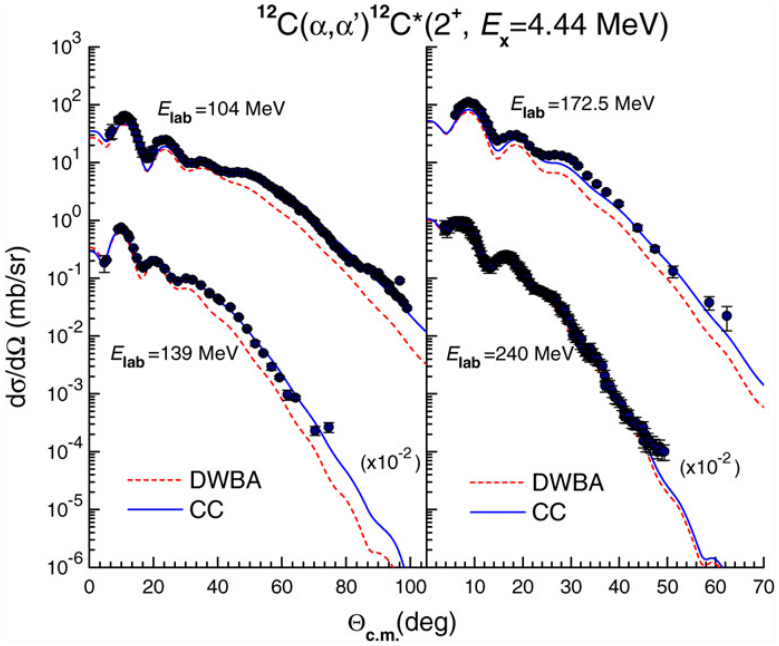

Figure 1.19: The DWBA and CC calculations for the cross section of the $^{12}\mathrm{C}(\alpha,\alpha')$ reaction exciting the 2_1^+ state at $E_\alpha = 104, 139, 172.5$, and 240 MeV. The solid circles are the experimental data, whereas the dotted and solid lines are the theoretical calculations. Taken from Fig. 5 in Ref. [58].

1.4 Systematic measurements of inelastic alpha scattering

The MDA of the inelastic alpha scattering at E_α = 96–386 MeV has been extensively performed to examine the nuclear structure as described in Sec. 1.2, however, the reliability of the MDA was shaken by the puzzle of the missing monopole strength discussed in Sec. 1.3. It is very important to examine and to solve this puzzle of the inelastic alpha scattering, otherwise, it leads us to serious situation where we cannot reliably examine the nuclear structure by means of the inelastic alpha scattering. Nevertheless, the systematic measurement of the inelastic alpha scattering to examine the reliability of the theoretical calculations has never been carried out until now.

In the present work, we measured the cross sections of the inelastic alpha scattering at E_α = 130 and 386 MeV, exciting low-lying discrete states in ^{12}C, ^{16}O, ^{20}Ne, ^{24}Mg, ^{28}Si and ^{40}Ca, and systematically compared the measured cross sections with the DWBA calculation for the first time. These targets were selected because the ambiguity of the nuclear structure in the DWBA calculation becomes small in the self-conjugate even-even nuclei.

Transition-density distributions used in the present DWBA calculations were obtained by the macroscopic models [60, 61], and the amplitudes of the transition-density distributions are determined from the electromagnetic transition strengths. The electromagnetic transition strengths for the discrete states were reliably determined by the electromagnetic probes like the inelastic electron scattering. Since the natural-parity transitions induced by the electromagnetic interaction are the "electric" transitions, their electromagnetic transition strengths are sensitive to protons only. On the other hand, the isoscalar natural-parity transitions induced by the inelastic alpha scattering are sensitive to both of protons and neutrons. Because the proton distribution in self-conjugate nuclei can be assumed to be same with the neutron distribution due to the isospin symmetry, the isoscalar transition strengths in such nuclei can be estimated from the electromagnetic transition strengths. Moreover, the spin and parity of the ground states in even-even nuclei are 0^+, therefore the transferred angular momentum is uniquely identified from the spin and parity of the final state.

A reliable calculation of cross sections is necessary to extract the transition strength from the experimental data in the MDA. We performed the "parameter-free" DWBA calculation in which all of the adjustable parameters are determined by the electromagnetic transition strengths and elastic scattering, and systematically compared with the

measured cross sections to test the applicability of the conventional DWBA calculation to the inelastic alpha scattering, for the first time. We also studied ambiguities of the DWBA calculations from the distorting potentials, phenomenological interaction, transition densities, and coupled-channel effects.

Chapter 2

Experiment

2.1 Overview

We systematically measured the cross sections of the inelastic alpha scattering at forward angles including 0° at E_α = 130 and 386 MeV, exciting low-lying states in ^{12}C, ^{16}O, ^{20}Ne, ^{24}Mg, ^{28}Si, and ^{40}Ca.

A series of the measurements (E253, E308, E369, and E402) was performed at Research Center for Nuclear Physics (RCNP), Osaka University. The incident alpha beam was accelerated by the coupled cyclotrons at RCNP, and transported to the target. Momenta of scattered alpha particles from the target were analyzed with the high-resolution magnetic spectrometer Grand Raiden (GR) [62]. The scattered particles are detected with the focal plane detectors of GR.

2.2 Beam line

A $^4He^{2+}$ beam was accelerated to 130 MeV by the AVF cyclotron. The accelerated beam was transported to the West experimental hall using the bypass beam line. For the measurements with the 386-MeV $^4He^{2+}$ beam, $^4He^{2+}$ beam accelerated up to 87.1 MeV by the AVF cyclotron was next injected into the ring cyclotron and accelerated again to 386 MeV. After the acceleration, the 386-MeV beam were transported to the West experimental hall. The accelerated beam was transported to the target through the WS beam line in the West experimental hall. Figure 2.1 shows the AVF cyclotron, the ring cyclotron, the bypass beam line, the West experimental hall, the WS beam line, and the target position.

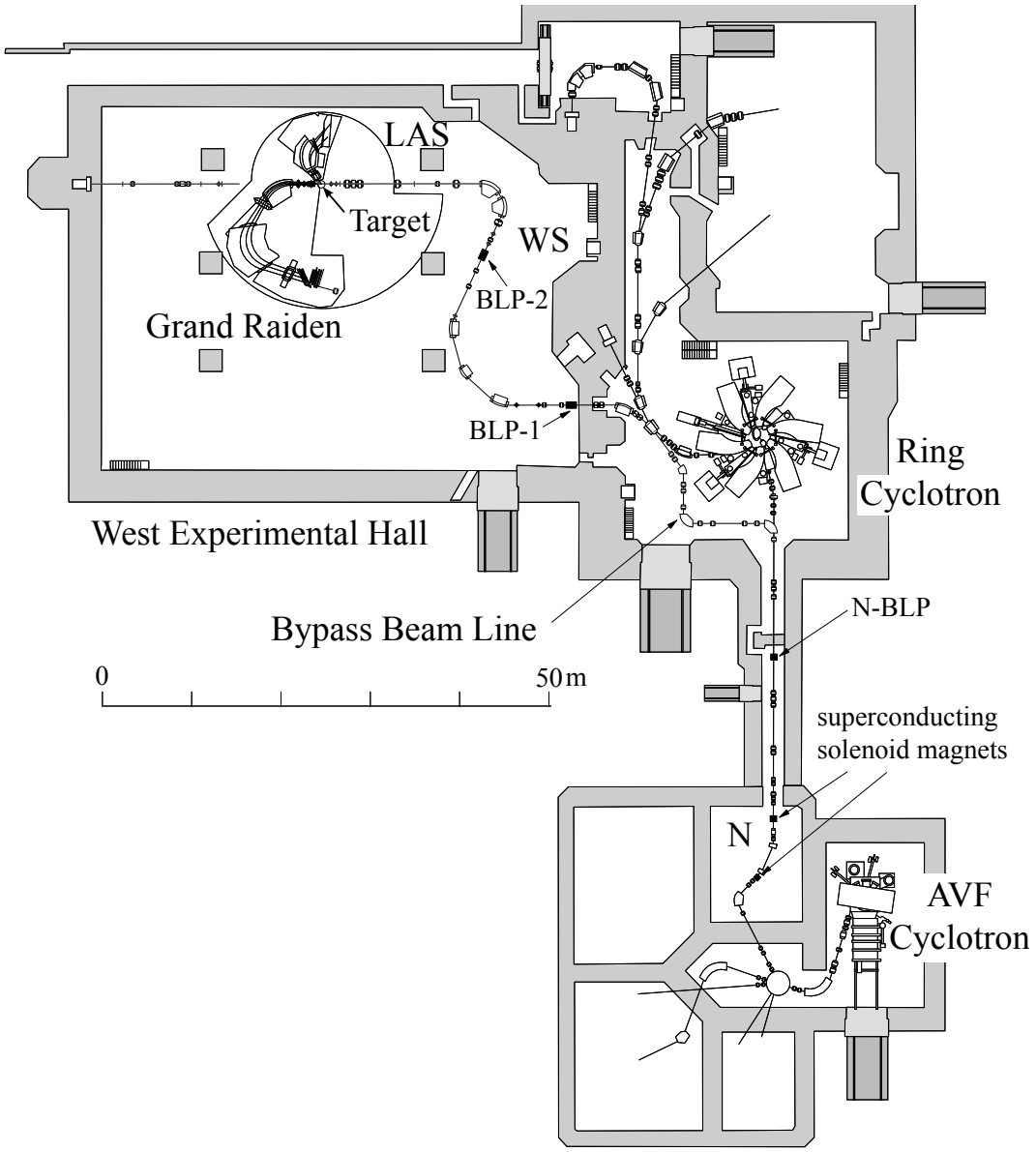

Figure 2.1: Overview of the AVF cyclotron and the ring cyclotron in RCNP. West experimental hall and the WS beam line are also shown. "WS" means the WS beam line.

The 130-MeV $^4He^{2+}$ beam was achromatically transported to the target, whereas the 386-MeV $^4He^{2+}$ beam was dispersively transported to the target in the measurements. The excitation-energy resolution at $E_\alpha = 386$ MeV was improved with the dispersive beam transport [63–65]. However, the dispersive beam transport for the ^{20}Ne gas target could not be done because the energy spread of the $^4He^{2+}$ beam from the ring cyclotron ($\Delta E = 250$ keV) was wider than the usual ($\Delta E = 100$ keV) when the ^{20}Ne gas target was used. This wider energy spread caused by the condition of the accelerators. The dispersive transport of such a beam with a wide energy spread results in unacceptably large beam size on the target.

2.3 Targets

We used self-supporting foil targets for ^{12}C, ^{24}Mg, ^{28}Si, and ^{40}Ca. The SiO_2 foil was used as the ^{16}O target. The contribution from ^{nat}Si was subtracted using a ^{nat}Si target. For the ^{20}Ne target, a cooling gas target system was used [66, 67].

Table 2.1 summarizes the target nuclei, thicknesses, and isotope enrichment.

Table 2.1: Thicknesses and isotope enrichment of the targets used in the present measurements with the $^4He^{2+}$ beams at $E_\alpha = 130$ and 386 MeV. All the foil targets are self-supporting.

Nucleus	State	Thickness	Enrichment	$^4He^{2+}$ energy	
				130	386
		(mg/cm^2)	(%)	(MeV)	
^{12}C	foil	2.2	98.9[a]	✓	✓
SiO_2[b]	foil	2.2	99.8[c]	✓	✓
^{20}Ne	gas[d]	2.4	99.95		✓
^{24}Mg	foil	1.2	99.92	✓	
^{24}Mg	foil	2.5	> 99.9		✓
^{28}Si	foil	1.72	92.2[a]	✓	
^{28}Si	foil	2.16	92.2[a]		✓
^{40}Ca	foil	1.63	> 99.9	✓	✓

[a] Natural abundance.
[b] The SiO_2 foil was used as the ^{16}O target.
[c] Natural abundance of ^{16}O.
[d] See the text for more details

2.3.1 Gas target

The isotopically enriched ^{20}Ne gas with a purity of 99.95% was filled into the gas cell and cooled by liquid N_2 in order to increase the target density. The entrance and exit windows were sealed with aramid films with a thickness of 4 μm. The pressure and temperature of the ^{20}Ne gas were monitored using the diaphragm pressure gauge (KM31, Nagano Keiki Co., Ltd.) and the platinum resistance thermometer (R610-3, Chino Co., Ltd.) during the measurements. The gas pressure and temperature were at 78.0 ± 1.2 kPa and 86.5 ± 0.4 K, respectively. The effective thickness of the ^{20}Ne gas target along the beam axis was calibrated by filling the gas cell with the CO_2 gas at the pressure close to that of the ^{20}Ne gas. We determined the thickness of the ^{20}Ne gas as 11.2 ± 1.7 mm by comparing the measured cross section of the elastic alpha scattering from ^{12}C with the known value. This thickness corresponded to 2.4 ± 0.4 mg/cm^2.

2.4 Magnetic spectrometer Grand Raiden

Scattered alpha particles were analyzed using the magnetic spectrometer Grand Raiden (GR) [62]. Figure 2.3(a) shows an overview of GR and its related instruments for the experimental setup at $\theta_{\rm lab} = 0^\circ$.

The GR has a magnet configuration of QSQD(M)D(+D). Here, the characters Q, S, D, M represents the quadrupole, sextupole, dipole, and multipole magnets, respectively. The QSQD(M)D(+D) are typically denoted as Q1, SX, Q2, D1, MP, D2, and DSR in order. The design specification of GR are listed in Table 2.2. The MP are mainly used to correct ion-optical aberrations, whereas the DSR is an auxiliary magnet for measurements of the spin-rotation parameters. The MP and DSR, which are denoted by the characters enclosed in parentheses, were not used to analyze the momenta of scattered particles in the present measurements. The DSR was used during the measurement at $\theta_{\rm lab} = 0^\circ$ as a steering magnet to guide the incident ^{4}He^{2+} beam to Faraday cups.

2.5 Focal plane detectors

The two multi-wire drift chambers (MWDC1 and 2) and two plastic scintillation counters (PS1 and 2) were installed at the focal plane of GR. The detector system was aligned along the focal plane at 45° with respect to the central ray of the spectrometer. Figs. 2.3(b) and 2.4 show the focal plane detectors, although the focal plane

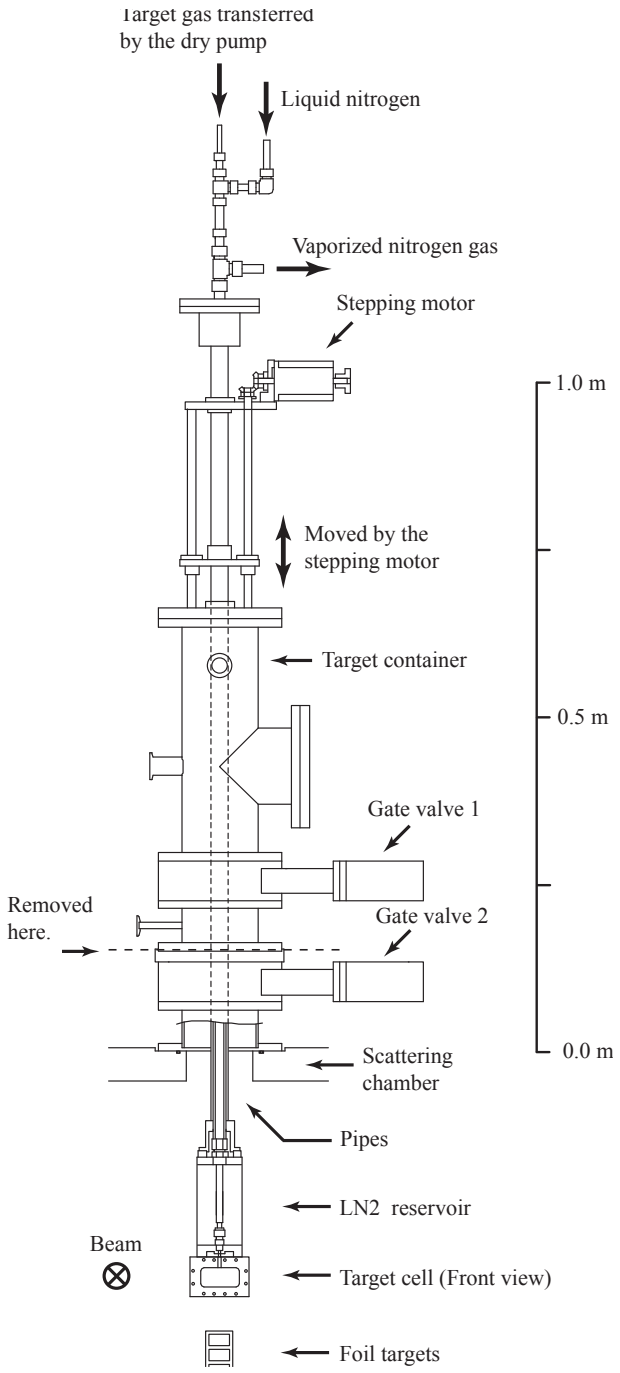

Figure 2.2: Schematic view of the gas target system, which is install on top of the scattering chamber [67]. ^{20}Ne gas was filled in the target gas cell and cooled by the liquid N_2.

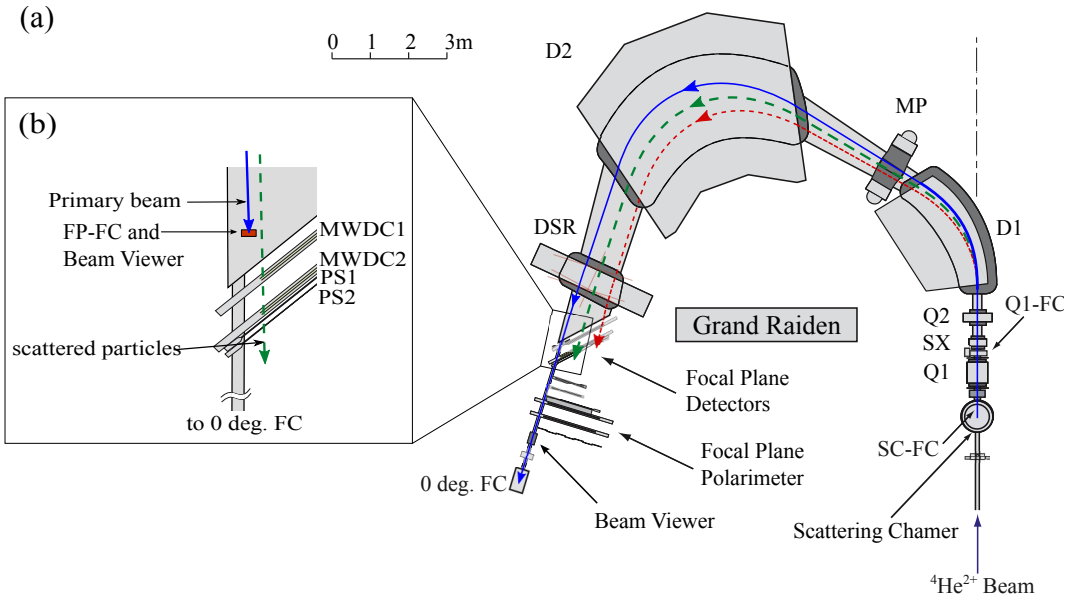

Figure 2.3: (a) Overview of the Grand Raiden spectrometer and its related instruments. The experimental setup at $\theta_{\mathrm{lab}} = 0°$ is shown [68]. The solid lines with arrow heads in the spectrometer show the trajectories of primary beam particles, and dashed and dotted lines show those of scattered particle. The primary beam was guided to the Faraday cup, which was located at the downstream of the spectrometer (0 deg. FC). (b) A schematic view around the focal plane. In case of the spectrum measurements for low-lying excited states, the primary beam was stopped at the focal plane Faraday cup (FP-FC), which was placed at the upstream of the focal plane.

Table 2.2: Design specification of the magnetic spectrometer Grand Raiden

	Grand Raiden
Configuration	QSQD(M)D(+D)
Mean orbit radius	3 m
Total deflection angle	162°
Focal plane length	150 cm
Tilting angle of focal plane	45°
Maximum magnetic field strength	1.8 T
Maximum magnetic rigidity	5.4 T·m
Horizontal magnification $(x\|x)$	-0.417
Vertical magnification $(y\|y)$	5.98
Momentum dispersion	15.451 m
Momentum range	5%
Momentum resolution	37,076
Acceptance of horizontal angle	$\pm$20 mr
Acceptance of vertical angle	$\pm$70 mr
Solid angle	$\sim$ 5.6 msr

polarimeters were not used in the present measurements. The MWDCs have holes at their high-momentum sides of the sensitive area, and the holes enable us to conduct the primary beam particles to the downstream for the 0° measurements.

The MWDCs were used to determine the three-dimensional trajectories of scattered particles at the focal plane, and the PS1 and PS2 which were placed at just the downstream of the MWDCs were used to generate the data-acquisition trigger. The plastic scintillators with a thickness of 10 mm were used as the PS1 and PS2, and the scintillation light was detected by the photo-multiplier tubes (PMTs) on the both sides of the PS1 and PS2.

2.5.1 Multi-wire drift chambers

Design specification of the MWDCs are shown in Table. 2.3. Each MWDC consists of two anode planes, namely horizontal (X) plane and the 48.2°-tiled (U) plane, and the anode wires are placed with the 2 mm spacing in the anode plane. The anode wires consists of the sense wires and the potential wires, and the spacing of sense wires are 6 mm in X-plane and 4 mm in U-plane as shown for X-plane in Fig. 2.5. High voltage of -4.8 kV was applied to the cathode planes of the MWDCs, and of -400 V was applied to the potential wires for the ^{20}Ne measurements. The wire configuration of the

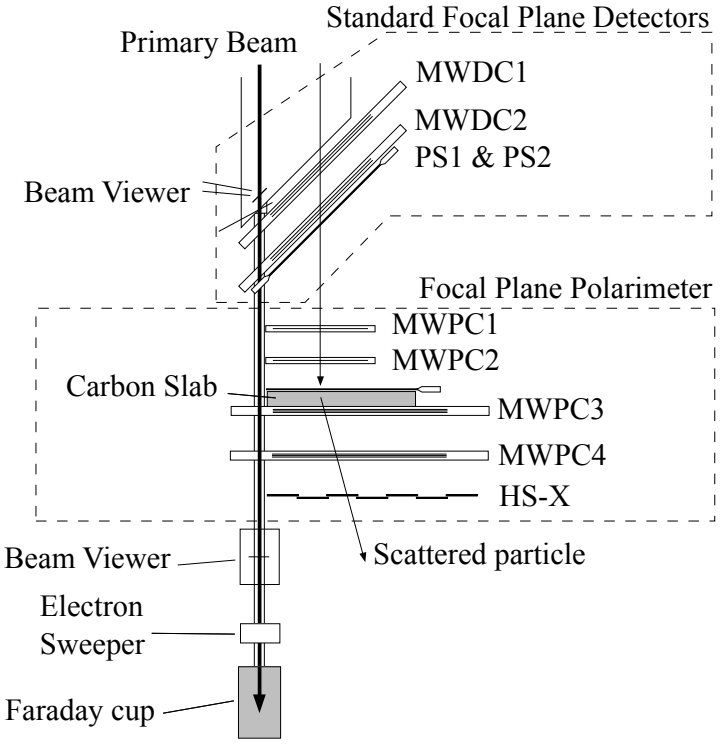

Figure 2.4: Schematic view of the focal plane detectors and downstream instruments of GR for the $\theta_{\rm lab} = 0^\circ$ measurement.

Table 2.3: Design specification of the MWDCs for GR placed at the focal plane. Supplied voltages are for the ^{20}Ne measurements.

	MWDC
Wire configuration	X(0° =vertical), U(−48.2°)
Active area	1150^{W}mm × 120^{H}mm
Number of sense wires	192(X), 208(U)
Cathode-anode gap	10 mm
Anode wire spacing	2 mm
Sense wire spacing	6 mm (X), 4 mm (U)
Sense wire material	20μm ϕ Au-W
Potential wire material	50μm ϕ Au-Cu/Be
Supplied voltage	−4.8 kV (cathode)
	−400 V (potential)
	0 V (sense)
Gas mixture	Argon(71.4%)+Iso-butane(28.6%)+Iso-propyl-alcohol
Gas seal	12.5μm aramid film
Pre-amplifier	LeCroy 2735DC
Digitizer	LeCroy 3377 drift chamber TDC

MWDCs for GR are shown in Fig. 2.6. The MWDCs were filled with a mixed gas which consists of argon, iso-butane, and iso-propyl-alcohol. Iso-propyl-alcohol was mixed at 2 °C vapor pressure into argon gas, and the argon and iso-butane gases were mixed with 71.4% and 28.6%. The MWDCs are placed at 45° with respect to the central ray of the spectrometer as shown in Fig. 2.4, therefore several sense wires typically generate the signal per plane for one trajectory of a scattered charged particle as shown in Fig. 2.5.

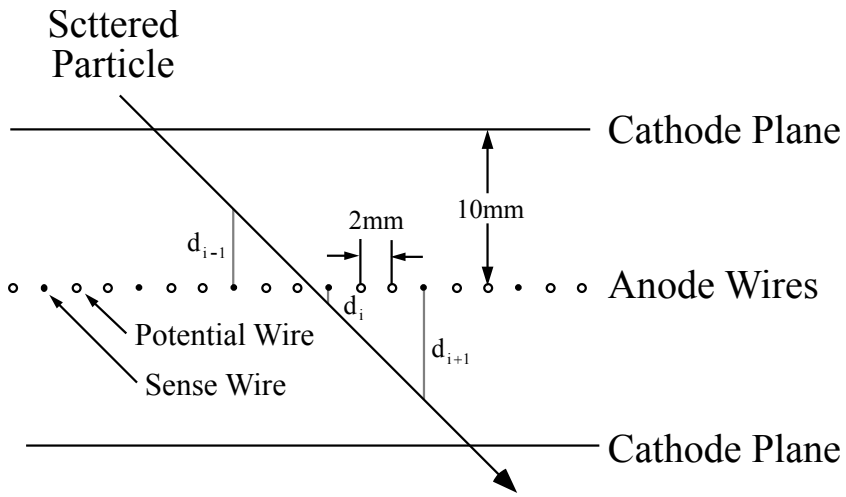

Figure 2.5: Schematic view for an X-plane of the MWDC. Typical trajectory of a scattered particle is also shown by an arrow.

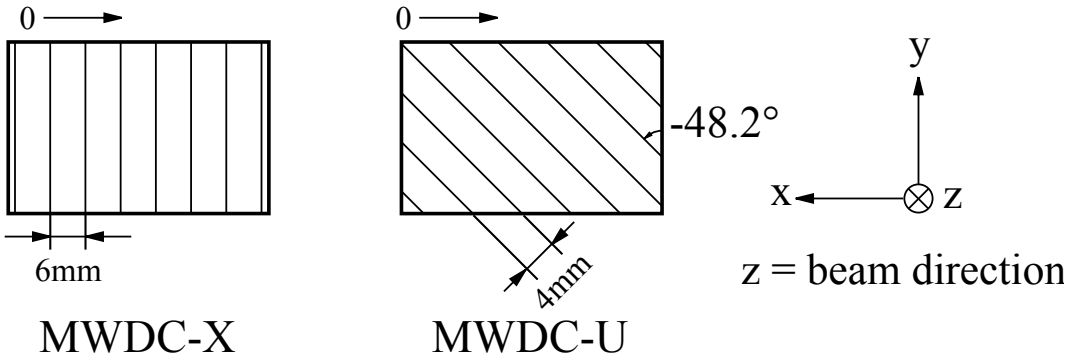

Figure 2.6: Wire configuration for the sense wires of the MWDCs. The wire numbering order are shown by arrows.

2.6 Faraday cups

The incident $^4He^{2+}$ beam was stopped by the four Faraday cups, and beam currents during the measurements were monitored. The zero-degree Faraday cup (0 deg. FC), which was located at the downstream of the focal plane, was used for the measurements at $\theta_{\rm lab} = 0^\circ$, and the primary beam was transported to the 0 deg. FC through GR. When the 0 deg. FC was used, the low-lying excited states at $E_x < 2.5$ MeV for $E_\alpha = 130$ MeV and at $E_x < 7.5$ MeV for $E_\alpha = 386$ MeV could not be measured due to the geometrical limitation of the MWDCs. The lateral distances between trajectories of the primary beam and scattered alpha particles exciting such low-lying states at the focal plane were too short for the MWDCs to detect the scattered alpha particles separately from the primary beam. To measure the (α, α') spectra for such low-lying states at $\theta_{\rm lab} = 0^\circ$, an alternative Faraday cup called as the focal plane Faraday cup (FP-FC) was used. The FP-FC was installed at the front of the MWDCs as shown in Fig. 2.3(b). Since the FP-FC was placed very close to the sensitive area of the MWDCs, the FP-FC enabled us to detect the scattered alpha particles exciting the low-lying states by the MWDCs. However, huge background γ rays from the FP-FC hit both the MWDCs and the trigger plastic scintillators, therefore the beam intensity was limited lower than 1.0 nA when the FP-FC was used.

For the measurements at $\theta_{\rm lab} = 2.5^\circ$–$5.0^\circ$, the primary beam was stopped at the Faraday cup behind the Q1 magnet of GR (Q1-FC) as shown in Fig. 2.3(a). The Faraday cup installed in the scattering chamber (SC-FC) was used in the measurements at the backward angles $\theta_{\rm lab} \geq 6.0^\circ$.

Charge collection efficiencies of the four Faraday cups were calibrated within 3% uncertainties by using a beam monitor (BLP-1) consisting of plastic scintillators located on the beam line.

2.6.1 Beam-line polarimeter

The beam-line polarimeters (BLP-1 and BLP-2) are located at the WS beam line as shown in Fig. 2.1. The BLP-1 was used to calibrate the charge collection efficiencies of the four Faraday cups in the present measurements. Each BLP consists of four sets of plastic scintillation detectors as shown in Fig. 2.7.

The scintillation detectors were placed at the angles of 14.4° and 40.0°. An aramid film with a thickness of 4 μm was used as the analyzer target to calibrate the charge

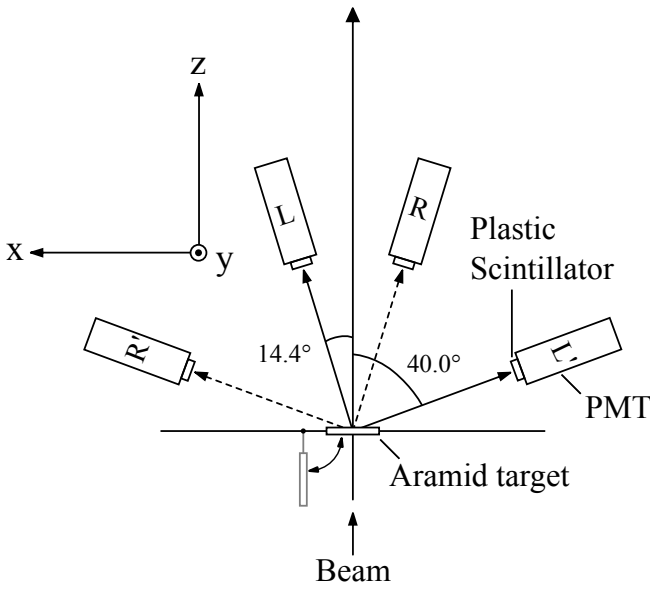

Figure 2.7: Schematic top view of the BLP setup. The plastic scintillation detectors labeled by "L" and "L′" are one set of the detectors. Similar to the horizontal (x-z) plane, there are also two pairs of the detector in the vertical (y-z) plane, but the detectors in the vertical plane were not used in the present measurements.

collection efficiency. An alpha particle flies to the detector at 14.4° when it is elastically scattered by a proton in the analyzer target, and the recoiling proton flies to the detector at 40.0°. $\alpha + p$ elastic scattering was identified by detecting scattered alpha particle and recoiling proton by a set of detectors in coincidence. The charge collection efficiencies of the four Faraday cups are calibrated by comparing the output of the four Faraday cups with the counting rate of the coincidence signals from the BLP detectors.

2.7 Data acquisition system

The data-acquisition triggering system was constructed with LeCroy 2366 universal logic modules (ULM), which were equipped with field programmable gate-array (FPGA) chips [69], and the trigger signals were generated by the coincidence of the PS1 and PS2 signals. A schematic view of the trigger circuit is shown in Fig. 2.8. Since the focal plane scintillators had the PMTs on both left and right edges, the PS1 and PS2 signals were generated with the coincidence of both PMTs signals.

The overview of the data acquisition (DAQ) system was shown in Fig. 2.9. Each

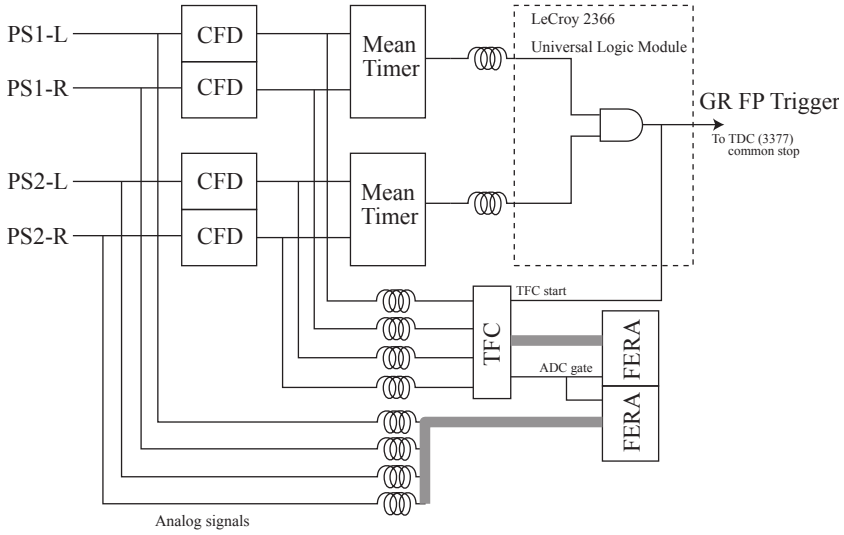

Figure 2.8: Schematic view of the trigger circuit and a part of circuit for analog signals.

event was constructed of the drift-time data from the MWDCs digitized by LeCroy 3377 TDC, the charge and timing signals from the trigger scintillators encoded with FERA and FERET system, and the input register. The Flow Controlling Event Tagger (FCET) [70] attached the event header, event number, and input register words to the data from LeCroy FERA and FERET systems, and the attached data was used to check the consistency of data in the subsequent event reconstruction.

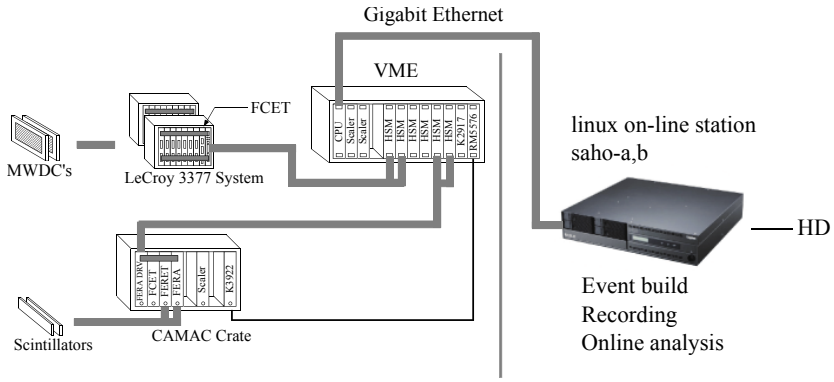

Figure 2.9: Overview of the data acquisition system.

The digitized data were transferred in parallel via ECL bus lines to the High Speed Memory (HSM) modules in the VME crate. The stored data in the HSMs were transferred via gigabit Ethernet to the Linux-based DAQ server (saho-a). The data recording to the storage, event building, online analysis were performed on the DAQ server.

2.8 Summary of the measurements

Table 2.4 summarizes the angular ranges for the cross-section measurements of the elastic alpha scattering at $E_\alpha = 130$ and 386 MeV, respectively. The cross sections at $E_\alpha = 130$ MeV were measured for all the targets except ^{20}Ne. The cross sections at backward angles between $\theta_{\mathrm{c.m.}} = 41.9°$ and $70.3°$ were measured using different experimental setup with the Si and CsI(Tl) detectors. The cross sections at $E_\alpha = 386$ MeV were measured for ^{12}C and ^{20}Ne only, although the cross sections for ^{24}Mg and ^{16}O were taken from Refs. [11] and [12], respectively. Since the cross sections for ^{28}Si and ^{40}Ca at $E_\alpha = 386$ MeV were not measured in the present experiment nor taken from previous works, a special treatment was done in the analysis of ^{28}Si and ^{40}Ca as described in Sec. 5.1.

Similarly, Table 2.5 summarizes the angular ranges for the cross-section measurements of the inelastic alpha scattering at $E_\alpha = 130$ and 386 MeV, respectively. The cross sections at $E_\alpha = 130$ MeV were measured for all the targets except ^{20}Ne.

Table 2.4: Angular ranges for the cross section measurements of the elastic alpha scattering at $E_\alpha = 130$ and 386 MeV.

Nucleus	Elastic scattering	
	$E_\alpha = 130$ MeV	$E_\alpha = 386$ MeV
	$\theta_{\text{c.m.}}$ (deg)	$\theta_{\text{c.m.}}$ (deg)
^{12}C	5.0°–70.3°	2.7°–34.2°
^{16}O	4.7°–58.1°	2.5°–28.5° [a]
^{20}Ne	Not measured	5.1°–27.4°
^{24}Mg	5.4°–70.4°	5.3°–28.8° [b]
^{28}Si	8.0°–48.8°	Not measured
^{40}Ca	4.1°–59.3°	Not measured

[a] Ref. [12].
[b] Ref. [11].

Table 2.5: Angular ranges for the cross section measurements of the inelastic alpha scattering at $E_\alpha = 130$ and 386 MeV.

Nucleus	Inelastic scattering	
	$E_\alpha = 130$ MeV	$E_\alpha = 386$ MeV
	$\theta_{\text{c.m.}}$ (deg)	$\theta_{\text{c.m.}}$ (deg)
^{12}C	0.5°–18.2°	0.4°–29.5°
^{16}O	0.5°–17.0°	2.4°– 7.0°
^{20}Ne	Not measured	0.5°–13.9°
^{24}Mg	0.5°–15.8°	0.8°–12.0°
^{28}Si	0.5°–15.5°	2.2°– 6.4°
^{40}Ca	0.4°–14.8°	2.1°– 6.2°

Chapter 3

Data Analysis

3.1 Particle identification

Particle identification was performed applying two gates on the data. One was the gate for the time difference between the data-acquisition trigger and the signal synchronized to the acceleration by the AVF cyclotron (RF signal), which corresponds to the time of flight from the target to the focal plane. The other was the gate for the energy deposit in the PS1.

Since the flight path of the scattered particle from the target to the focal plane depends on the scattering angle and the momentum of the particle, the correction to the time difference was performed to remove the dependence on the position at the focal plane (x_{fp}) related to the momentum and the scattering angle at the target (θ_{tgt}) as shown in Fig. 3.1. The raw and corrected time difference are shown in the left and right panels in Fig. 3.2, respectively. Since the RF signal was downscaled by a rate divider circuit, two prominent peaks due to the alpha particles were observed as shown in Fig. 3.2.

Particle identification by the energy deposit in the PS1 was performed using the signals from the the PMTs attached to both edges of the PS1. Considering that the emitted light in the scintillators is attenuated exponentially during the transmission to the PMT, the geometric mean of the ADC values of the two PMTs on the left and right edges of the PS1 is approximately independent from the position where the scattered particle hits, and is proportional to the energy deposit. Figures 3.3(a) and (b) show the correlation between the ADC values from the left and right PMT and the horizontal positions, whereas Fig. 3.3(c) is the correlation between the geometrical mean of the ADC values

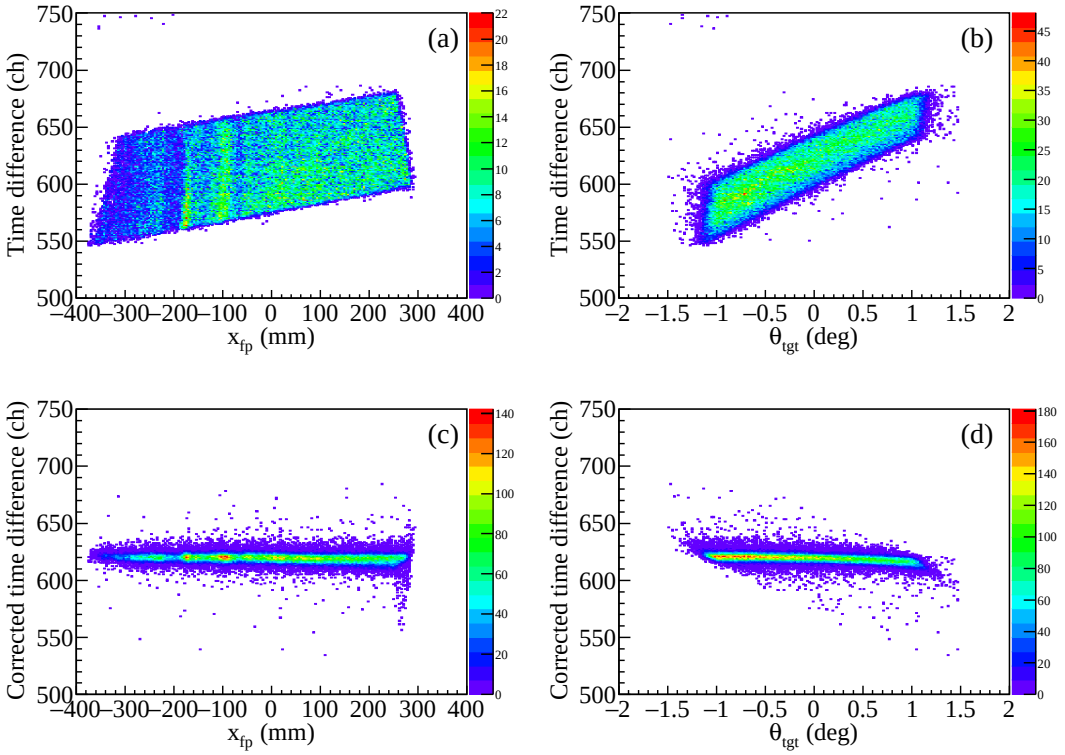

Figure 3.1: Two demensional scatter plot of the time difference between the data-acquisition trigger and the RF signal versus the horizontal position at the focal plane (x_{fp}) and the horizontal scattering angle (θ_{tgt}). The data for the measurement of highly excited region in ^{12}C from the inelastic alpha scattering at $E_\alpha = 386$ MeV are shown. (a) and (b) show the time difference before the correction, whereas (c) and (d) show after the correction.

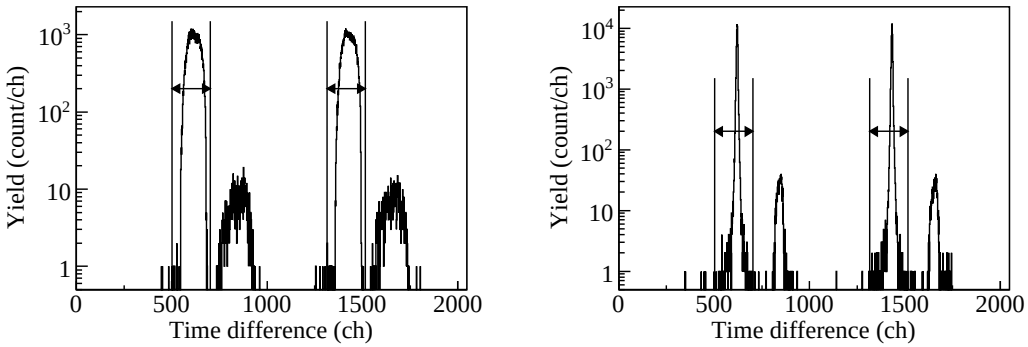

Figure 3.2: Example of the particle identification using the time difference. The regions shown by the arrows correspond to the alpha particles. The left panel shows the time difference before the correction, whereas the right shows that after the correction.

from the left and right PMTs. The geometrical mean is almost independent from the particle position although the signals from the PMTs attenuate with increasing the distance between the particle position and the PMTs.

The loci with the higher ADC values in Fig. 3.3 were attributed to the alpha particles, whereas those with the lower ADC values were due to the low energy-loss particles. These low energy-loss particles were eliminated as seen in Fig. 3.4 by limiting the time difference between the data-acquisition trigger and the RF signal (see Fig. 3.2). Figure 3.5 shows the spectra of the geometric mean of the ADC values from left and right PMTs. The small peak due to the low energy-loss particles in Fig. 3.5(a) disappears in Fig. 3.5(b) in similar to Fig. 3.4. The alpha particles were identified by selecting the region shown by the arrow in Fig. 3.5(b).

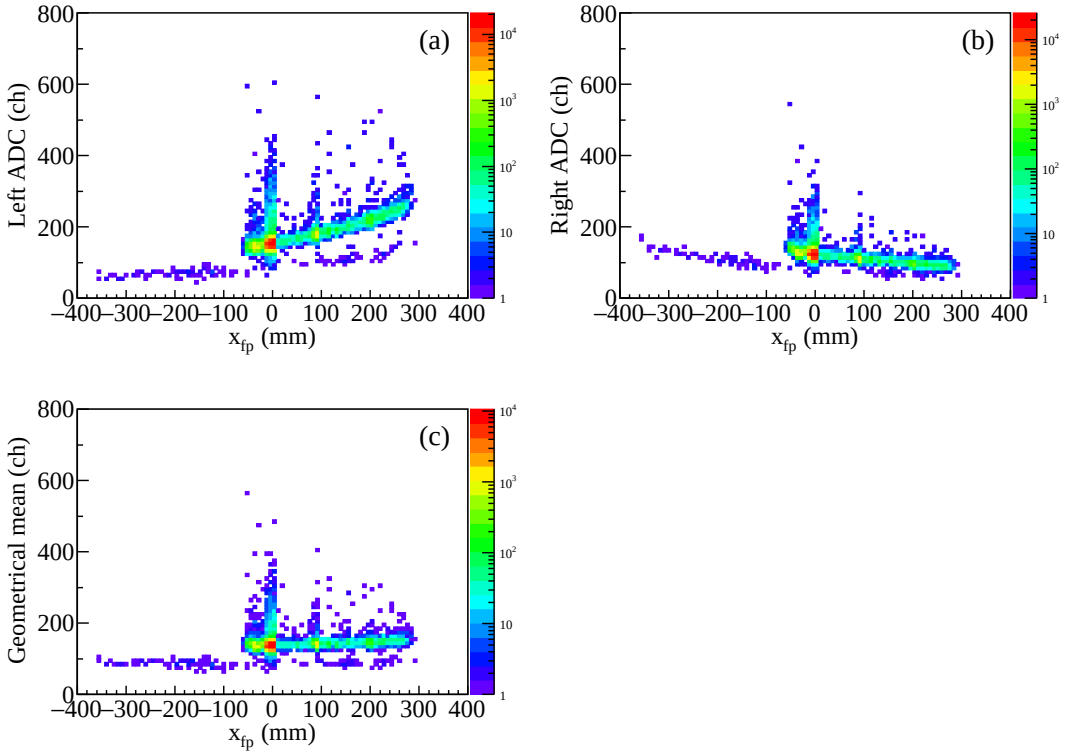

Figure 3.3: Example of the ADCs of the scattered particle at the PS1 for the measurement of the elastic and inelastic scattering from aramid films at E_α = 386 MeV at $\theta_{\rm lab} = 8.0°$. (a) and (b) Two-dimensional scatter plots for the ADC values from the left or right PMT versus the horizontal positions ($x_{\rm fp}$). (c) Two-dimensional scatter plot of the geometrical mean of the ADC values from the left and right PMTs versus the horizontal position.

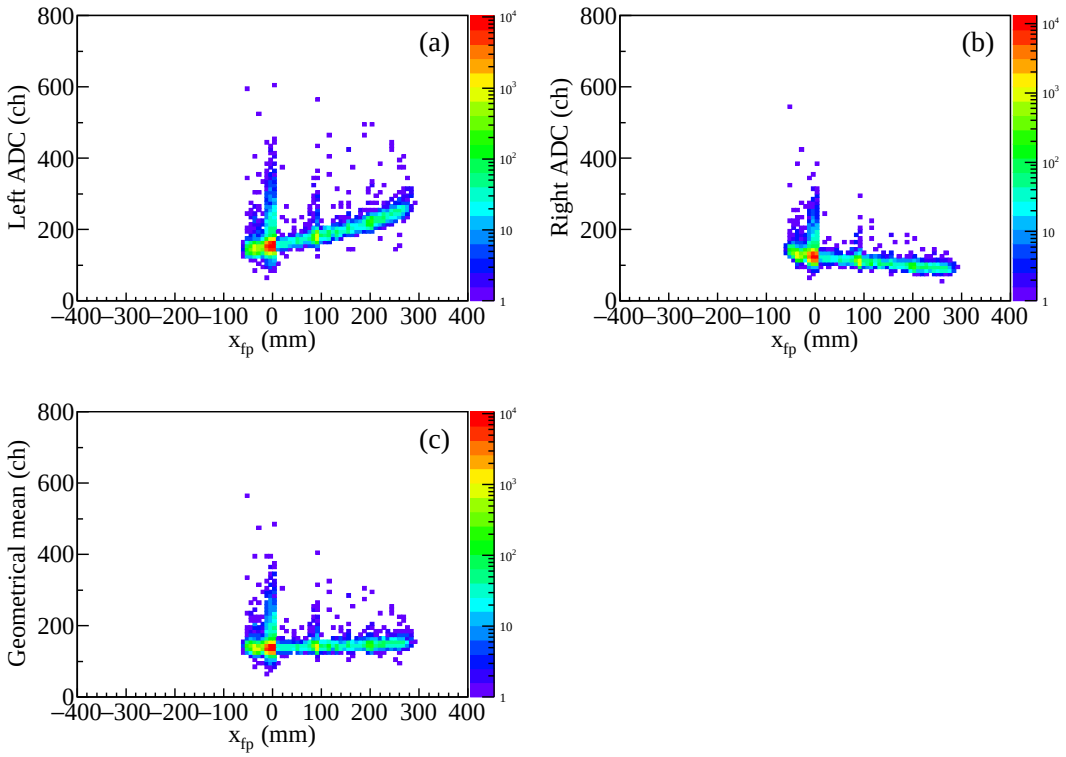

Figure 3.4: Same as Fig. 3.3, but gated by the time difference between the data-acquisition trigger and the RF signals.

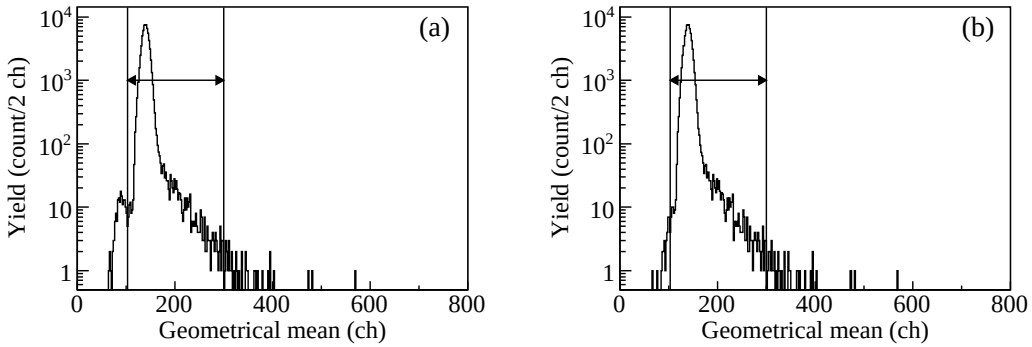

Figure 3.5: Example of the particle identification using the energy deposit in the PS1. The region shown by the arrows correspond to the alpha particles. (a) The geometric mean of ADCs without the gate of the time difference. (b) With the gate of the time difference.

3.2 Track reconstruction

The three-dimensional trajectories of the particles were reconstructed by using the position information from the two sets of the MWDCs at the focal plane of GR. The position parallel to the anode wires in each anode plane was determined from the vertical drift lengths $d_{i-1}, d_i, \cdots$ at hit wires as shown in Fig. 2.5. The positions on the X-plane of the MWDC1 (X1) and the X-plane of the MWDC2 (X2) defined an X-tracking plane, and those on the U-planes (U1 and U2) defined a U-tracking plane, and thus the trajectory of the detected particles was determined as in Fig. 3.6.

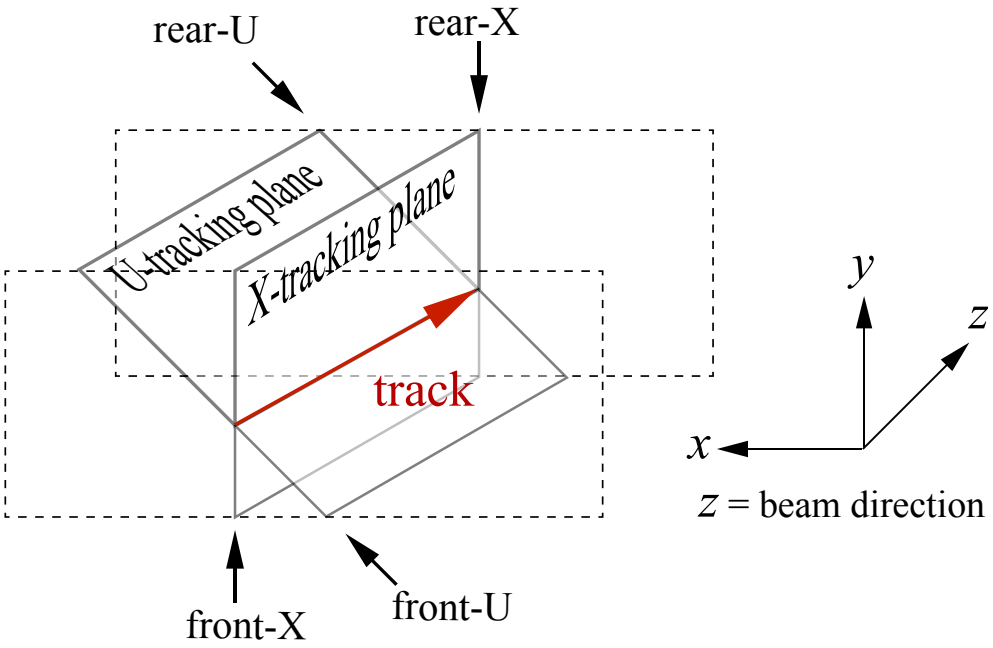

Figure 3.6: Schematic view of the determination of the particle trajectory.

Since only the drift time to each sense wire can be directly measured, the calibration of the drift time to the drift length was performed using the measurement of a continuum spectrum in a highly excited region in ^{12}C. Schematic histograms which represents the conversion from the drift time to the drift length are show in Fig. 3.7.

As already discussed in Sec. 2.5.1, a typical scattered particle induces the signals at two or more sense wires as shown in Fig. 2.5. We define a group of such adjacent sense wires as a "cluster". In the present analysis, all the anode planes were required to have only one cluster which contains not less than two hit wires. The cluster which contains only one wire was ignored because the background events such as X- and γ-rays usually

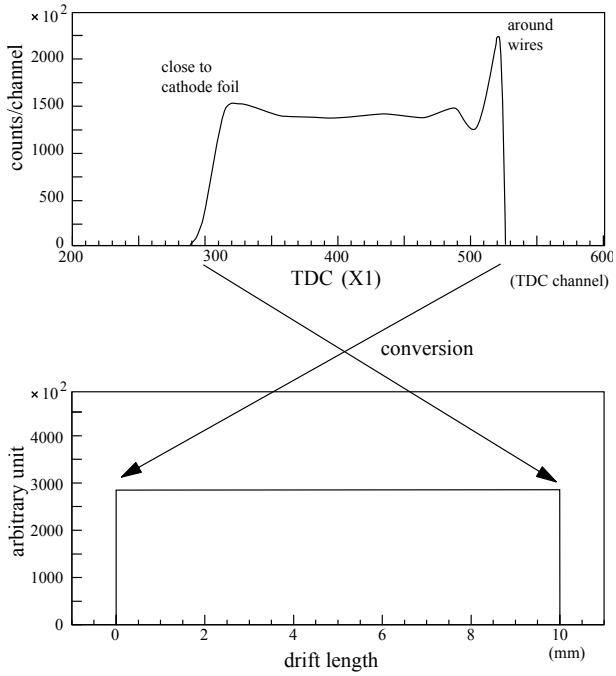

Figure 3.7: Conversion from the drift times to the drift lengths of the MWDCs

cause the single hit wire.

3.2.1 Efficiency

The efficiency of each plane of the MWDCs is estimated as follows,

$$\epsilon_{X1} = \frac{N_{X1\cap U1\cap X2\cap U2}}{N_{U1\cap X2\cap U2}}, \tag{3.1}$$

$$\epsilon_{U1} = \frac{N_{X1\cap U1\cap X2\cap U2}}{N_{X1\cap X2\cap U2}}, \tag{3.2}$$

$$\epsilon_{X2} = \frac{N_{X1\cap U1\cap X2\cap U2}}{N_{X1\cap U1\cap U2}}, \tag{3.3}$$

$$\epsilon_{U2} = \frac{N_{X1\cap U1\cap X2\cap U2}}{N_{X1\cap U1\cap X2}}, \tag{3.4}$$

where $N_{X1\cap U1\cap X2\cap U2}$ denotes the number of events in which the tracks of the particles were reconstructed by all of the four planes of the MWDCs, and $N_{U1\cap X2\cap U2}$, ($N_{X1\cap X2\cap U2}$, $N_{X1\cap U1\cap U2}$, and $N_{X1\cap U1\cap X2}$) in the denominator denotes the number of events in which the tracks were reconstructed by the three planes except the $X1$ ($U1$, $X2$, and $U2$) plane. The overall tracking efficiency ϵ_{MWDC} of the MWDCs was calculated

by $\epsilon_{\mathrm{MWDC}} = \epsilon_{X1} \times \epsilon_{U1} \times \epsilon_{X2} \times \epsilon_{U2}$.

The position dependence of the tracking efficiency was examined. Since the position at the focal plane could be related to the excitation energy in the inelastic alpha scattering, the efficiency of each plane of the MWDCs for α particles inelastically scattered from the ^{12}C target at $E_\alpha = 386$ MeV and $\theta_{\mathrm{lab}} = 8.0°$ was obtained as a function of excitation energy. As shown in Fig. 3.8, the tracking efficiency of the MWDCs was almost constant to the excitation energy.

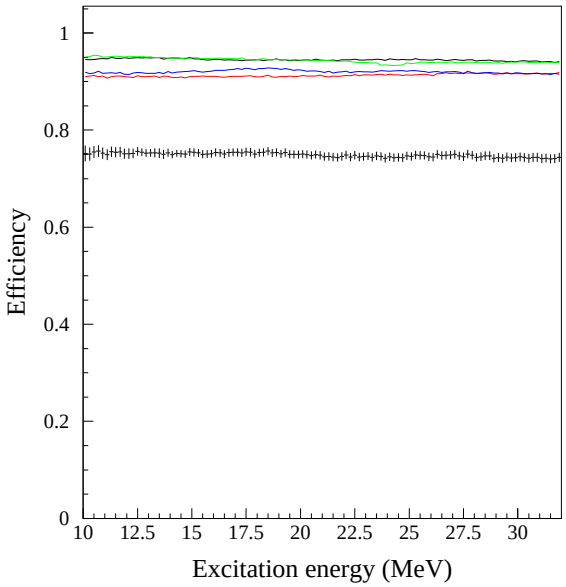

Figure 3.8: Example of the detection efficiency of each plane of the MWDCs for alpha particles inelastically scattered from the target at $E_\alpha = 386$ MeV and $\theta_{\mathrm{lab}} = 8.0°$ as a function of excitation energy. The black, red, green, and blue lines show the efficiencies for X1, U1, X2, and U2 planes, respectively. The histogram with error bars shows the total tracking efficiency.

3.3 Calibration of the excitation energy and the scattering angle

The excitation energy was calculated from the momentum and scattering angle of the detected particle assuming the two-body scattering at the incident energy of $E_\alpha = 386$

or 130 MeV. Since only the momentum deviation from the central ray can be measured with the magnetic spectrometer, the energy scale of the calculated excitation energy was calibrated using the peak position for the known discrete excited states in the measured spectra.

Scattering angles within the angular acceptance of GR were calibrated using the sieve slit as reported in Ref. [68]. Figure 3.9 shows the sieve slit used for the ^{20}Ne measurements. The large hole at the center of the slit is designed to be placed on the incident beam axis. The upstream side of the slit was at the 577.5 mm downstream from the target. The hole spacings in the horizontal and vertical directions corresponded to 0.496° and 1.190° from the target, respectively.

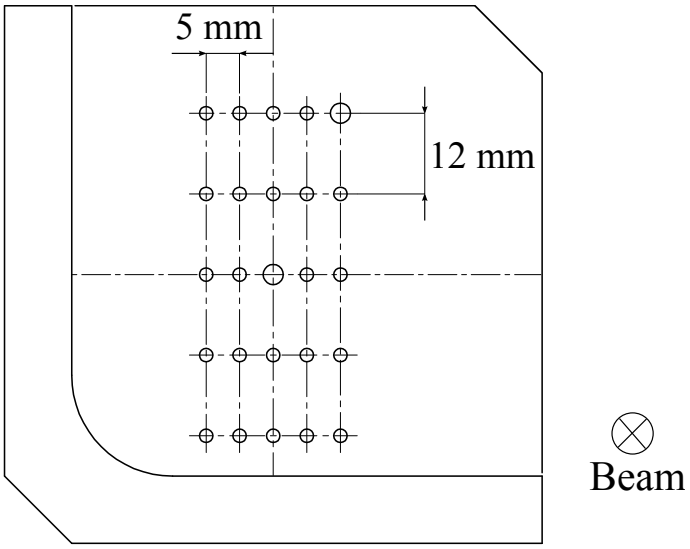

Figure 3.9: Drawing of the sieve slit used for the calibration in the ^{20}Ne measurements. The large hole at the center of slit is designed to be placed on the incident beam axis. The dash-dotted lines are drawn to guide the eyes.

Figures 3.10 and 3.11 show the data from five measurements with different magnetic field strengths using the sieve slit to calibrate the scattering angle for the ^{20}Ne measurements. The field strength of GR was set at five different values with the steo of 0.8%. The particles which were scattered at the target and passed through a hole of the sieve slit were detected at the focal plane. The two dimensional scatter plot of the measured angle at the focal plane ($\theta_{\rm fp)}$ versus the horizontal position ($x_{\rm fp}$) is shown in Fig. 3.10. The particles passed through the holes at the same horizontal angle form one locus as seen in Fig. 3.10. The measured angle ($\theta_{\rm fp}$) and the position ($x_{\rm fp}$) were converted to the

scattering angle at the target ($\theta_{\rm tgt}$) and the momentum difference from the central ray using the optical properties of GR, and calibrated using the geometrical information of the sieve slit. The two dimensional scatter plot of the calibrated scattering angle at the target ($\theta_{\rm lab}$) versus the momentum difference from the central ray is shown in Fig. 3.11. The angular acceptance of GR was limited to $|\theta_{tgt}| \leq 0.8°$ and was divided into four

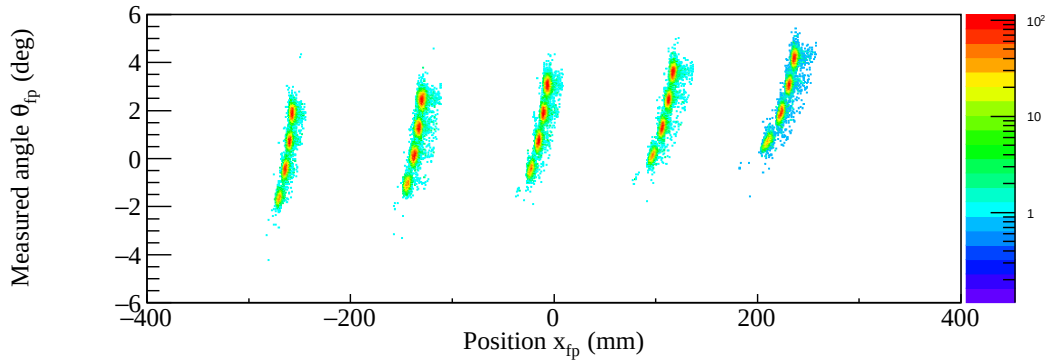

Figure 3.10: Two dimensional scatter plot of the measured horizontal angles at the focal plane of GR ($\theta_{\rm fp}$) versus the position at the focal plane ($x_{\rm fp}$). The data from five measurements with different magnetic field strengths are superimposed.

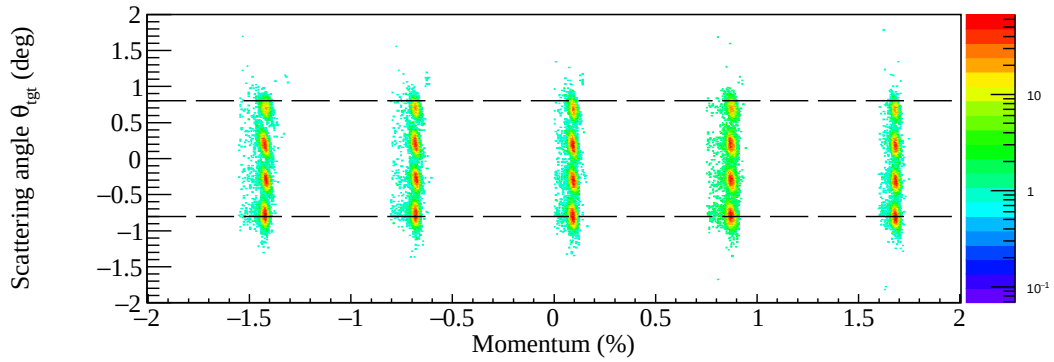

Figure 3.11: Two dimensional scatter plot of the scattering angles at the target ($\theta_{\rm tgt}$) versus the momentum difference from the central ray. The data from five measurements with different magnetic field strength are superimposed. The dashed lines are drawn at $|\theta_{tgt}| = 0.8°$, and the data in the region between the two lines were analyzed to obtain the cross sections.

angular bins with a width of 0.4° to obtain the cross sections.

3.4 Background subtraction

Beam particles passing through the target spread out due to multiple Coulomb scattering and hit beam ducts. These particles caused continuous background in excitation-energy spectra at forward angles. These background events were removed using the vertical position information of scattered particles at the focal plane because alpha particles scattered from the target were vertically focused near the focal plane whereas background particles scattered at different positions were not focused [71].

An (α, α') spectrum measured using the ^{20}Ne gas target is shown in Fig. 3.12(a). Several discrete peaks for the ground and excited states in ^{12}C, ^{14}N, ^{16}O, and ^{35}Cl were

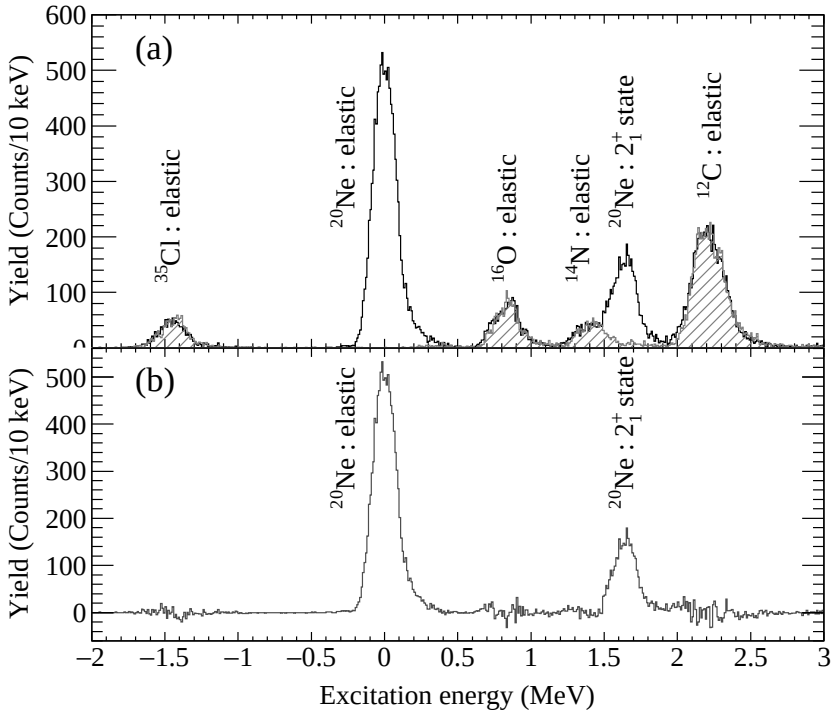

Figure 3.12: Excitation-energy spectra for the ^{20}Ne(α, α') reaction at $E_\alpha = 386$ MeV measured at $\theta_{\rm lab} = 10.8°$. (a) The open histogram represents the excitation-energy spectrum obtained using the gas cell filled with ^{20}Ne. The hatched histogram represents the normalized spectrum obtained using the empty gas cell. (b) A background-free ^{20}Ne(α, α') spectrum obtained by subtracting the background events originated from aramid films.

observed. These nuclei are contained in the aramid films at the entrance and exit windows of the gas cell. In order to subtract the background events due to the aramid

windows, the background measurements with the empty gas cell was carried out. The pressure of the empty gas cell was kept at the order of 10^{-2} Pa. The measured background spectrum is shown by the hatched histogram in Fig. 3.12(a). The background-free spectra were successfully obtained by subtracting background spectra as seen in Fig. 3.12(b). The normalization factor for the background subtraction was calculated by taking into account the beam intensities, target thicknesses, tracking efficiencies, and data-acquisition efficiencies. Similarly, the background-free excitation energy spectra for ^{16}O were obtained by subtracting the excitation energy spectra for ^{nat}Si from those for $^{nat}SiO_2$.

3.5 Cross sections for the (α, α) and (α, α') reactions

The obtained excitation-energy spectra for the (α, α') reactions at $E_\alpha = 130$ MeV at $\theta_{\rm lab} = 0.0°$ are shown in Fig. 3.13. The typical energy resolution of the (α, α') spectra

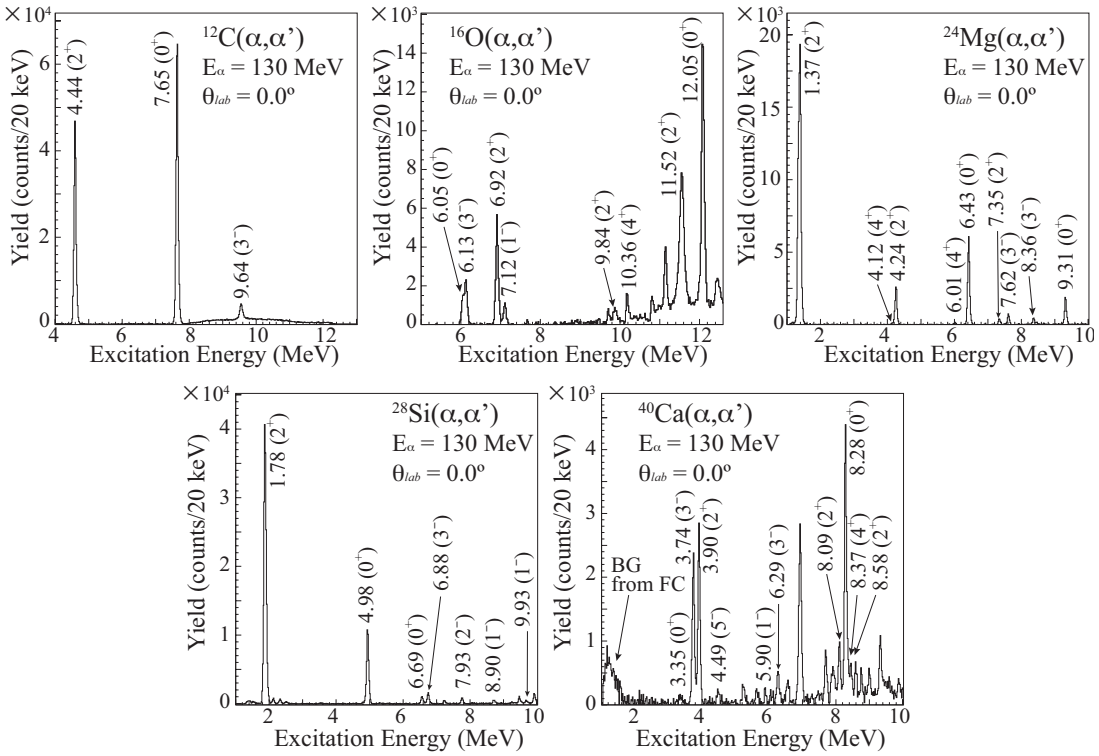

Figure 3.13: Excitation-energy spectra for the (α, α') reactions at $E_\alpha = 130$ MeV measured at $\theta_{\rm lab} = 0.0°$.

at $E_\alpha = 130$ MeV and 386 MeV was about 85 keV and 95 keV at the full width at half maximum (FWHM) for the solid targets except ^{20}Ne, respectively. On the other hand, the energy resolution of the $^{20}\mathrm{Ne}(\alpha, \alpha')$ reaction at $E_\alpha = 386$ MeV was about 250 keV at FWHM. This wider energy spread was caused by the condition of the accelerators.

From these excitation energy spectra, the cross sections of the (α, α) reaction at $E_\alpha =$ 130 and 386 MeV were obtained as follows.

The number of the scattered alpha particles exciting an excited state was counted in the excitation energy spectrum. The cross section at the scattering angle θ_{lab} in the laboratory frame $[d\sigma/d\Omega(\theta)]_{\mathrm{lab}}$ was determined from the number of the detected alpha particles Y, the number of the target nucleus N_{tgt}, the number of the incident alpha particles N_{beam}, the solid angles for the spectrum $\Delta\Omega$, the tracking efficiency $\epsilon_{\mathrm{track}}$, the charge-collection efficiency ϵ_{FC}, and the data-acquisition efficiency ϵ_{DAQ}.

$$\left[\frac{d\sigma}{d\Omega}(\theta_{\mathrm{lab}})\right]_{\mathrm{lab}} = \frac{Y}{N_{\mathrm{tgt}} \cdot N_{\mathrm{beam}} \cdot \Delta\Omega} \cdot \frac{1}{\epsilon_{\mathrm{track}} \cdot \epsilon_{\mathrm{FC}} \cdot \epsilon_{\mathrm{DAQ}}}. \tag{3.5}$$

The cross section in the laboratory frame $[d\sigma/d\Omega(\theta_{\mathrm{lab}})]_{\mathrm{lab}}$ was converted to that in the center-of-mass frame $[d\sigma/d\Omega(\theta_{\mathrm{c.m.}})]_{\mathrm{c.m.}}$ using the relation between the laboratory and center-of-mass frames as follows,

$$\left[\frac{d\sigma}{d\Omega}(\theta_{\mathrm{c.m.}})\right]_{\mathrm{c.m.}} = g(\theta_{\mathrm{lab}}) \left[\frac{d\sigma}{d\Omega}(\theta_{\mathrm{lab}})\right]_{\mathrm{lab}}, \tag{3.6}$$

where $g(\theta_{\mathrm{lab}})$ is the conversion factor. $g(\theta_{\mathrm{lab}})$ and $\theta_{\mathrm{c.m.}}$ are calculated from the relativistic kinematics using the masses of the target nucleus and the alpha particle, the excitation energy of the state, and the scattering angle in the laboratory frame θ_{lab}. The errors were estimated from uncertainties of all the quantities in Eq. (3.6).

The measured cross sections of the elastic (α, α) reactions at $E_\alpha = 386$ and 130 MeV relative to the Rutherford cross sections (Rutherford ratio) are presented in Figs. 3.14 and 3.15, respectively. Similarly, the cross sections of the inelastic (α, α') reactions at $E_\alpha = 386$ and 130 MeV were obtained as presented in the next chapter.

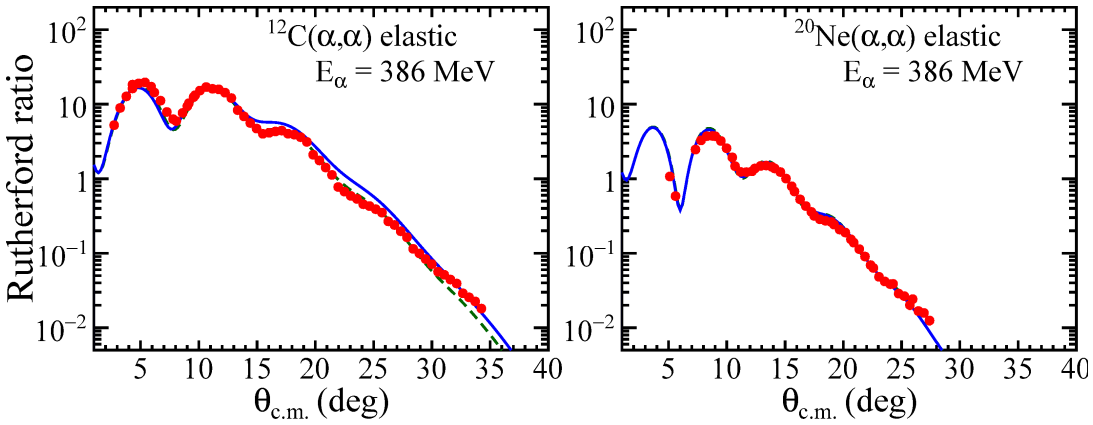

Figure 3.14: Measured cross sections of the elastic alpha scattering off ^{12}C and ^{20}Ne at $E_\alpha = 386$ MeV relative to the Rutherford cross sections (Rutherford ratio) compared with the theoretical calculation. The solid circles with error bars show the measured cross sections. The solid and dashed lines represent the results of calculation with the density-independent (DI) and density-dependent (DD) αN interactions, respectively. For the details about the theoretical calculations, see Chap. 5.

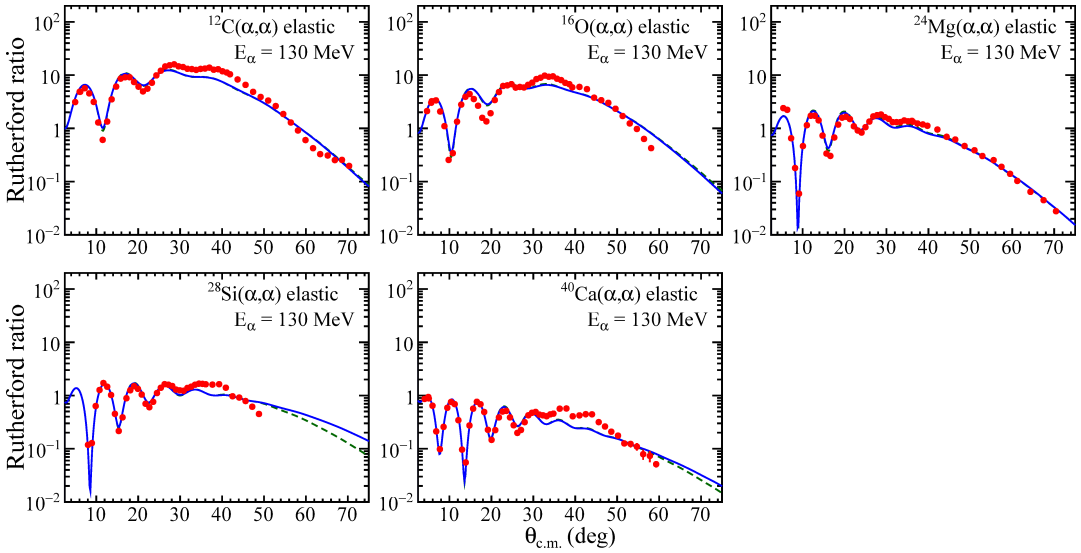

Figure 3.15: Same as Fig. 3.15, but for ^{12}C, ^{16}O, ^{24}Mg, ^{28}Si, and ^{40}Ca at $E_\alpha = 130$ MeV.

Chapter 4

Results

The measured (α, α') cross sections for the $\Delta L = 0$, $\Delta L = 2$, and $\Delta L = 3$ transitions at $E_\alpha = 386$ and 130 MeV are shown in Figs. 4.1 and 4.2, Figs. 4.3 and 4.4, and Figs. 4.5 and 4.6, respectively. The excited states of which the cross sections were measured in the present work are listed in Table 4.1. Figures 4.7 and 4.8 show those for $\Delta L = 4$ and $\Delta L = 1$, respectively. In Figs. 4.2–4.8, the cross sections of the excited states whose electromagnetic excitation strengths from the ground states were reported in the previous studies [47, 72–76] are presented, whereas the measured cross sections of the excited states whose electromagnetic transition strengths are unknown are shown in Fig. 4.9.

Table 4.1: List of the excited states identified in the present work.

Nucleus	J^π	E_x	E_α		Nucleus	J^π	E_x	E_α	
			130	386				130	386
		(MeV)	(MeV)				(MeV)	(MeV)	
^{12}C	0^+_1	0.00	✓	✓	^{24}Mg	2^+_5	9.00	✓	✓[b]
^{12}C	2^+_1	4.44	✓	✓	^{24}Mg	1^-_1	9.15	✓	✓[b]
^{12}C	0^+_2	7.65	✓	✓	^{24}Mg	0^+_3	9.31	✓	✓[b]
^{12}C	3^-_1	9.64	✓	✓	^{24}Mg	2^+_7	10.36	✓	
^{12}C	1^-_1	10.84	✓		^{28}Si	0^+_1	0.00	✓	
^{16}O	0^+_1	0.00	✓	✓[a]	^{28}Si	2^+_1	1.78	✓	✓
^{16}O	0^+_2	6.05	✓		^{28}Si	4^+_1	4.62	✓	
^{16}O	3^-_1	6.13	✓	✓	^{28}Si	0^+_2	4.98	✓	✓
^{16}O	2^+_1	6.92	✓	✓	^{28}Si	0^+_3	6.69	✓	
^{16}O	1^-_1	7.12	✓		^{28}Si	3^-_1	6.88	✓	
^{16}O	2^+_2	9.84	✓		^{28}Si	2^+_2	7.93	✓	
^{16}O	4^+_1	10.36	✓		^{28}Si	2^+_3	8.26	✓	
^{16}O	2^+_3	11.52	✓	✓	^{28}Si	1^-_1	8.90	✓	
^{16}O	0^+_3	12.05	✓	✓	^{28}Si	2^+_4	9.48	✓	
^{20}Ne	0^+_1	0.00		✓	^{28}Si	1^-_2	9.93	✓	
^{20}Ne	2^+_1	1.63		✓	^{28}Si	3^-_2	10.18	✓	
^{20}Ne	4^+_1	4.25		✓	^{28}Si	2^+_5	10.51	✓	
^{20}Ne	3^-_1	5.62		✓	^{40}Ca	0^+_1	0.00	✓	
^{20}Ne	0^+_2	6.73		✓	^{40}Ca	0^+_2	3.35	✓	
^{24}Mg	0^+_1	0.00	✓	✓[b]	^{40}Ca	3^-_1	3.74	✓	✓
^{24}Mg	2^+_1	1.37	✓	✓[b]	^{40}Ca	2^+_1	3.90	✓	✓
^{24}Mg	4^+_1	4.12	✓		^{40}Ca	5^-_1	4.49	✓	
^{24}Mg	2^+_2	4.24	✓		^{40}Ca	1^-_1	5.90	✓	
^{24}Mg	4^+_2	6.01	✓		^{40}Ca	3^-_2	6.29	✓	
^{24}Mg	0^+_2	6.43	✓	✓[b]	^{40}Ca	2^+_2	8.09	✓	
^{24}Mg	2^+_3	7.35	✓	✓[b]	^{40}Ca	0^+_3	8.28	✓	
^{24}Mg	3^-_1	7.62	✓	✓[b]	^{40}Ca	4^+_1	8.37	✓	
^{24}Mg	3^-_2	8.36	✓	✓[b]	^{40}Ca	2^+_3	8.58	✓	

[a] Ref. [12]
[b] Ref. [11]

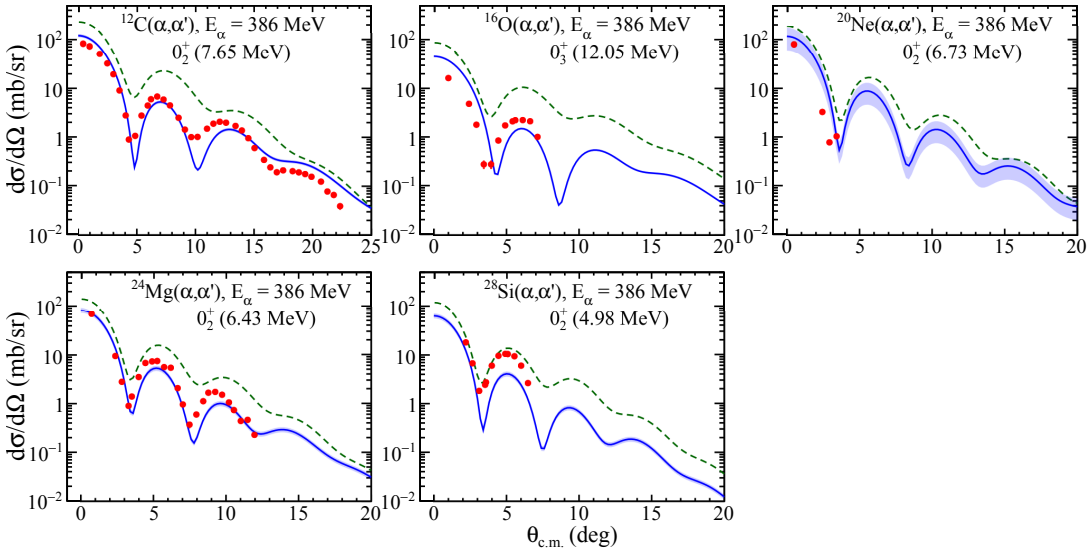

Figure 4.1: Measured cross sections of the (α, α') reaction at $E_\alpha = 386$ MeV for the $\Delta L = 0$ transitions whose electromagnetic transition strengths are known from the previous studies [47, 72–76]. The solid circles with error bars show the measured cross sections. The solid lines with error bands and dashed lines are the theoretical calculations with the density-independent (DI) and density-dependent (DD) αN interactions, respectively. The error bands are shown for the theoretical calculations with DI interactions only. For details about the theoretical calculations, see Chap. 5.

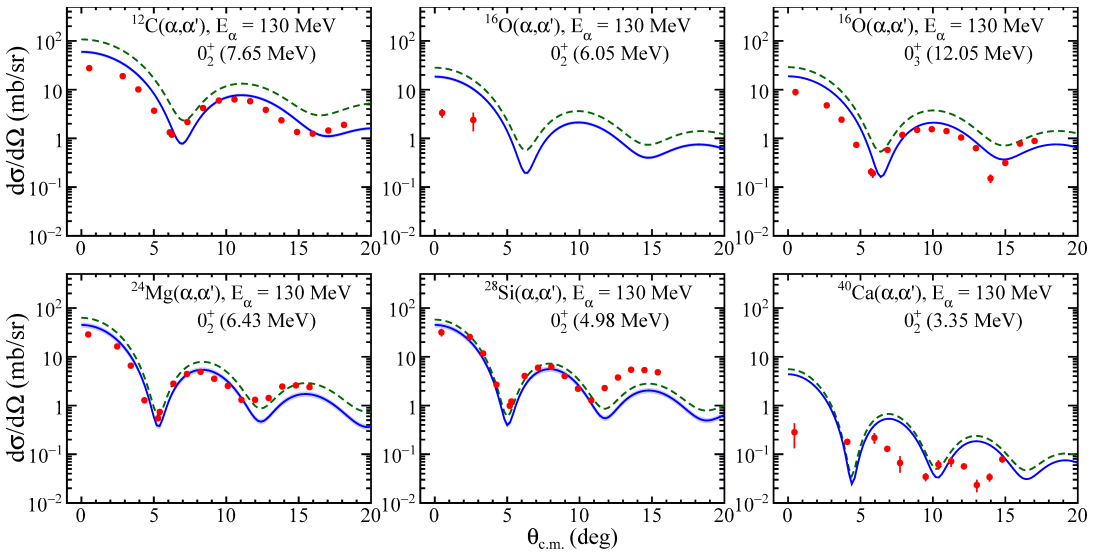

Figure 4.2: Same as Fig. 4.1, but the cross sections for the $\Delta L = 0$ transitions at $E_\alpha = 130$ MeV.

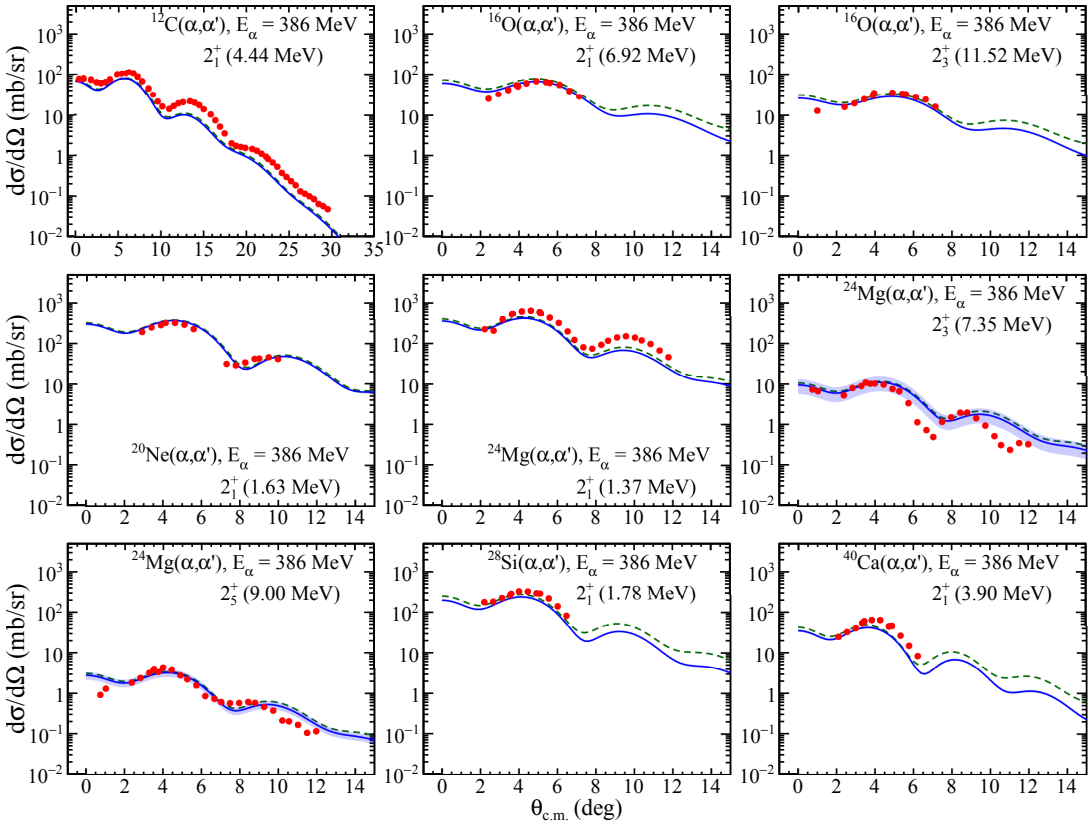

Figure 4.3: Same as Fig. 4.1, but the cross sections for the $\Delta L = 2$ transitions at $E_\alpha =$ 386 MeV.

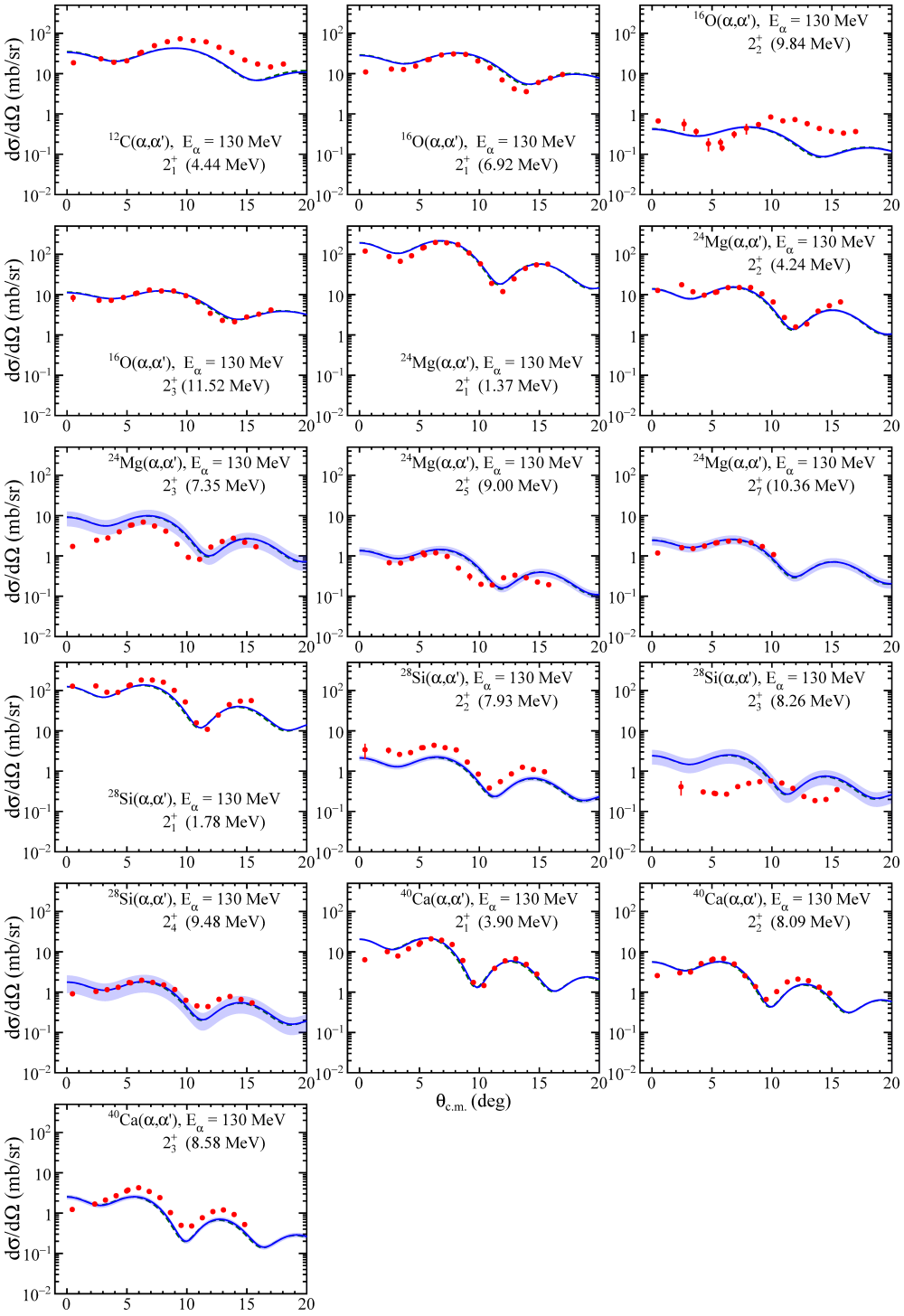

Figure 4.4: Same as Fig. 4.1, but the cross sections for the $\Delta L = 2$ transitions at $E_\alpha =$ 130 MeV.

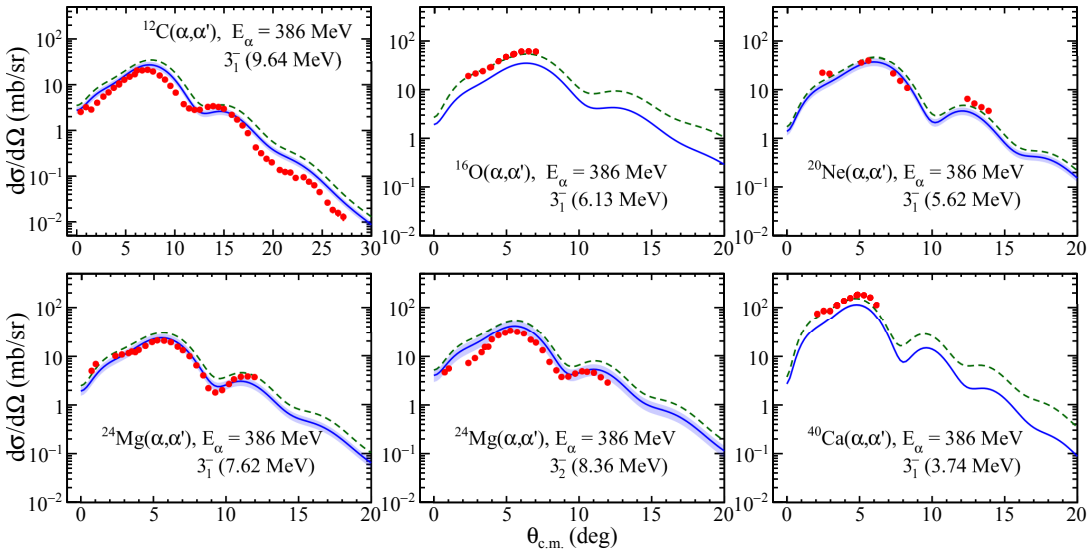

Figure 4.5: Same as Fig. 4.1, but the cross sections for the $\Delta L = 3$ transitions at $E_\alpha =$ 386 MeV.

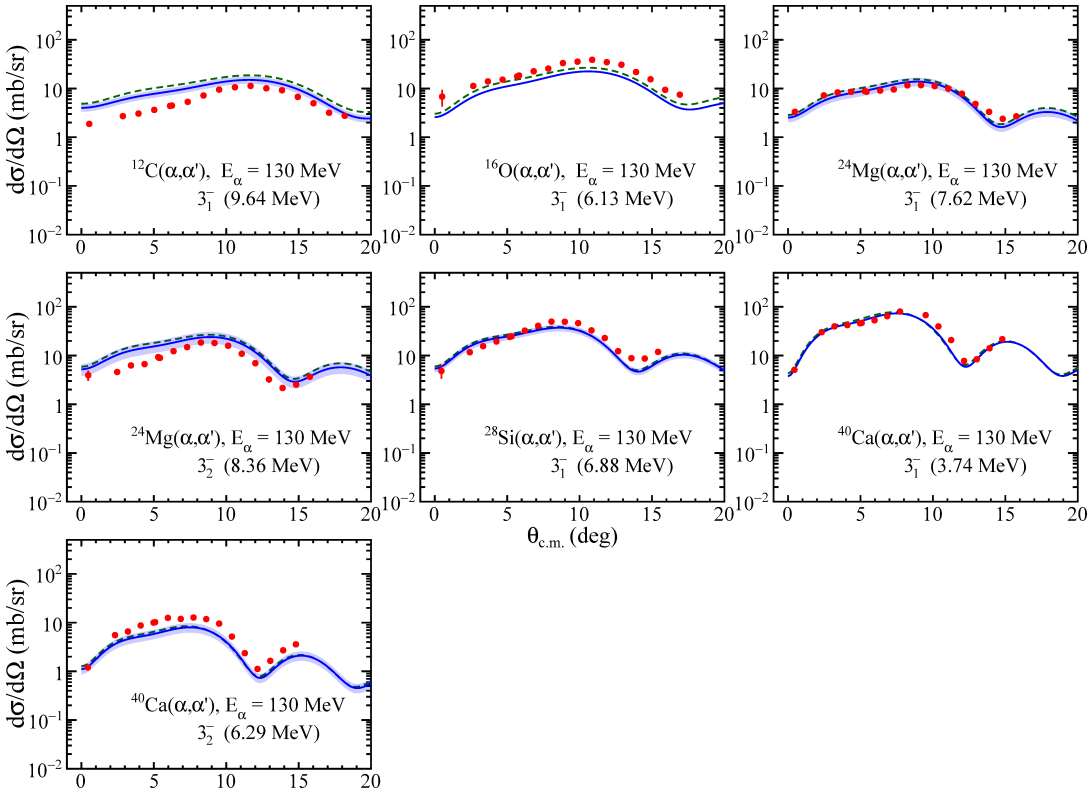

Figure 4.6: Same as Fig. 4.1, but the cross sections for the $\Delta L = 3$ transitions at $E_\alpha =$ 130 MeV.

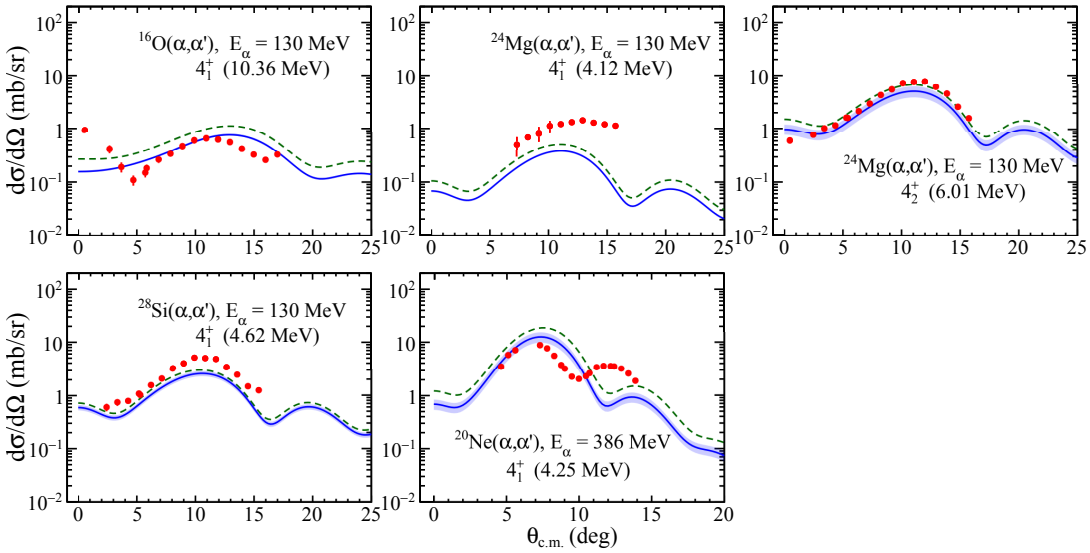

Figure 4.7: Same as Fig. 4.1, but the cross sections for the $\Delta L = 4$ transitions at $E_\alpha =$ 130 and 386 MeV.

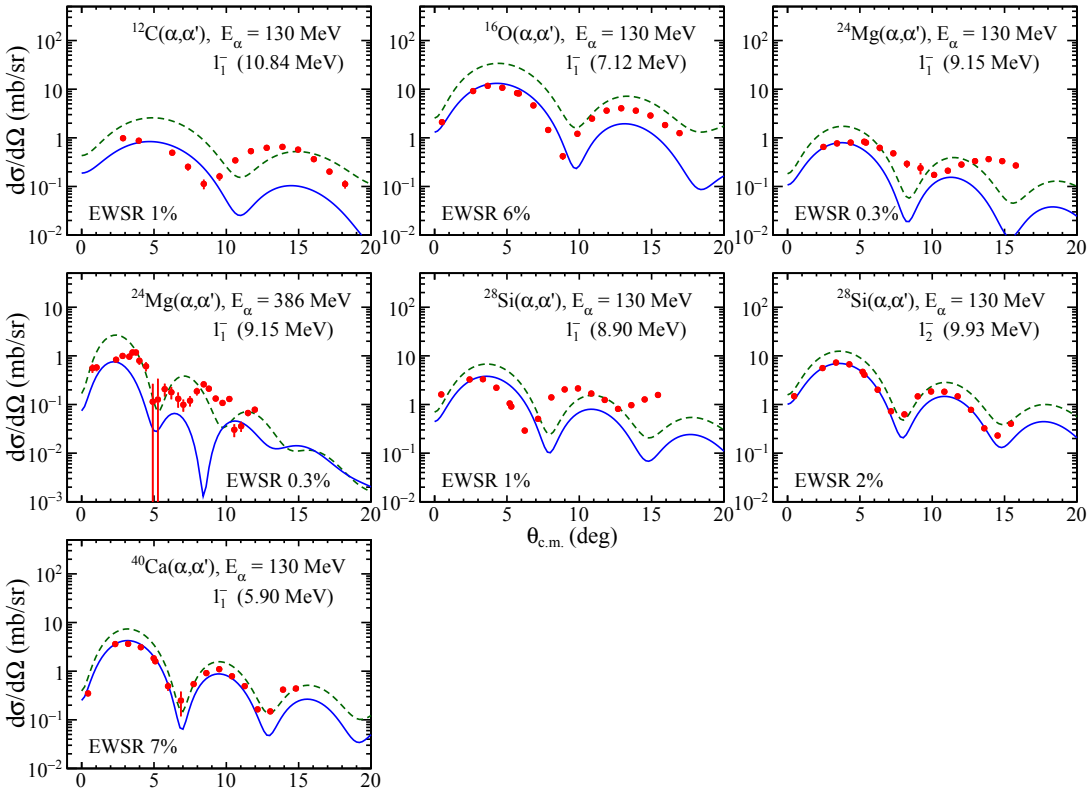

Figure 4.8: Same as Fig. 4.1, but the cross sections for the $\Delta L = 1$ transitions at $E_\alpha = 130$ and 386 MeV. Note that the calculated cross sections are normalized to exhaust 1%, 6%, 0.3%, 1%, 2%, and 7% of the EWSR strengths of the isoscalar dipole transitions in ^{12}C(1^-_1), ^{16}O(1^-_1), ^{24}Mg(1^-_1), ^{28}Si(1^-_1), ^{28}Si(1^-_2), and ^{40}Ca(1^-_1), respectively. For details about the theoretical calculations, see Chap. 5 and Sec. 6.4.

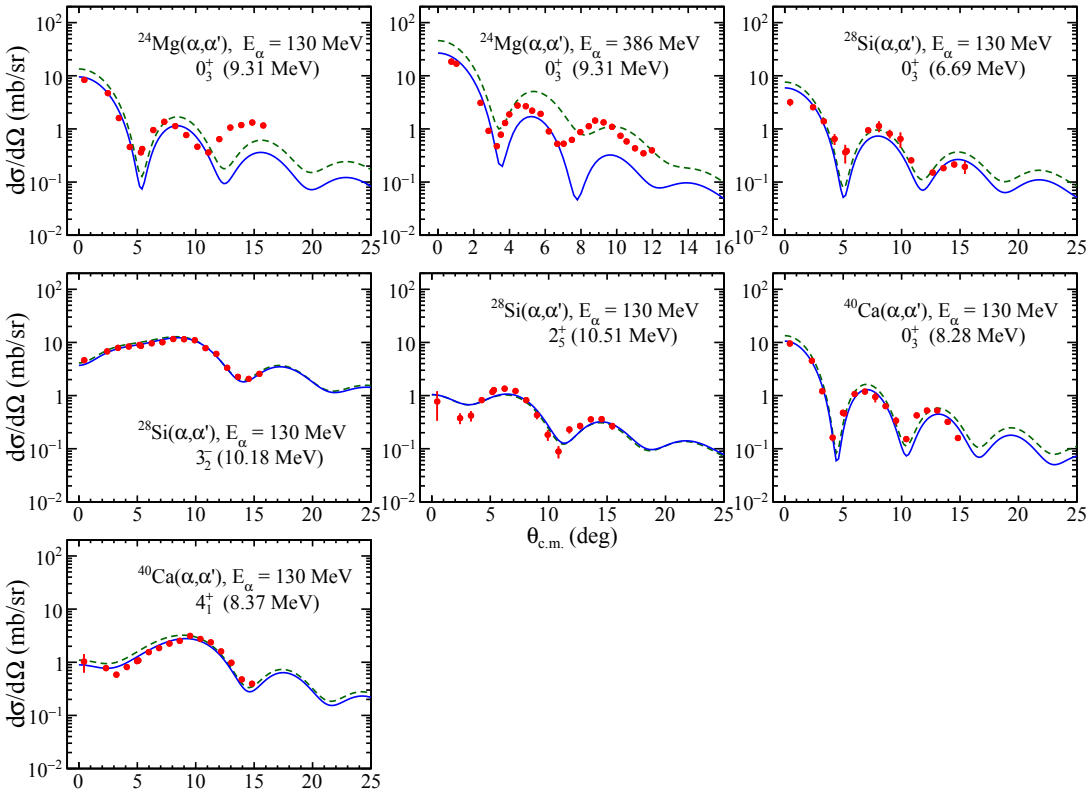

Figure 4.9: Same as Fig. 4.1, but the cross sections for the inelastic alpha scatterings at $E_\alpha = 130$ and 386 MeV where the corresponding electromagnetic transition strengths are not reported in the previous studies [47, 72–76]. Note that the calculated cross sections with the DI interactions (solid lines) are fitted to the experimental data.

Chapter 5

DWBA analysis

The theoretical model calculation is necessary to extract the transition strength from the obtained cross sections, and we performed the DWBA analyses using the computer code ECIS-95 [77]. The measured cross sections were compared with the DWBA calculations using the known values of the electromagnetic transition strengths in order to check the reliability of the theoretical calculation, which are widely used in the previous [3–13, 16, 17]. In this chapter, the formalism of the present calculations are explained.

In the present DWBA calculation, the optical-model potentials for the elastic alpha scattering were used as the distorting potentials. The same distorting potential was used in the entrance and exit channels for each nucleus. The optical-model potentials and the transition potentials between the ground and excited states were calculated by folding the macroscopic densities with the effective αN interaction.

5.1 Optical-model potential and the effective αN interaction

An optical-model potential $U(r)$ for elastic alpha scattering is obtained by folding the ground-state density distribution of the target nucleus with effective αN interaction $u\left[|\boldsymbol{r}-\boldsymbol{r'}|, \rho_0(r')\right]$ as follows,

$$U(r) = \int d\boldsymbol{r'} \rho_0(r')\ u\left[|\boldsymbol{r}-\boldsymbol{r'}|, \rho_0(r')\right], \tag{5.1}$$

where $\boldsymbol{r'}$ and $\boldsymbol{r}$ denote the position of a point-like nucleon in the target and an incident alpha particle, respectively. $\rho_0(r')$ is the ground-state density distribution of a target nucleus. Figure 5.1 shows the definition of the spacial coordinates $\boldsymbol{r}$ and $\boldsymbol{r'}$.

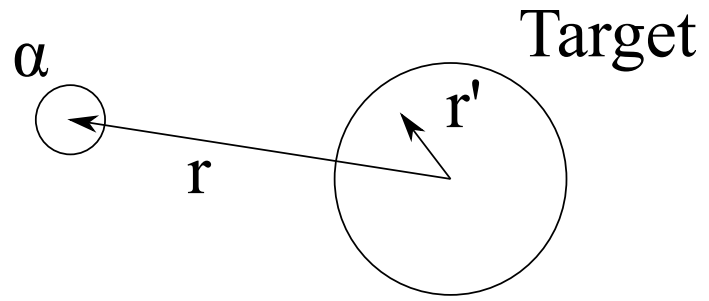

Figure 5.1: Definition of the spacial coordinates in Eq. (5.1).

$u\left[|\boldsymbol{r}-\boldsymbol{r'}|, \rho_0(r')\right]$ is empirically parameterized by five adjustable parameters [78] as

$$\begin{aligned} u\left[|\boldsymbol{r}-\boldsymbol{r'}|, \rho_0(r')\right] = \quad & -v\left[1+\beta\rho_0^{2/3}(r')\right] e^{-|\boldsymbol{r}-\boldsymbol{r'}|^2/\alpha_v^2} \\ & -iw\left[1+\beta\rho_0^{2/3}(r')\right] e^{-|\boldsymbol{r}-\boldsymbol{r'}|^2/\alpha_w^2}, \end{aligned} \tag{5.2}$$

where v and w are the depth parameters, β is the density-dependence parameter, and α_v and α_w are the range parameters for real and imaginary parts of the αN interaction, respectively.

5.1.1 Density distribution of nucleus

The density distributions of the ground states of the target nuclei were calculated from the charge distributions obtained by the electron scattering measurements. The charge distributions of ^{12}C, ^{16}O, ^{24}Mg, ^{28}Si, and ^{40}Ca were parameterized in the form of the sum of Gaussian functions [79], while that of ^{20}Ne was in the form of the two-parameter Fermi model [80]. In the form of the sum of Gaussian function, the charge distribution $\tilde{\rho}_0^c(r)$ is expressed as follows [79],

$$\tilde{\rho}_0^c(r) = \sum_i A_i \left\{ \exp\left[-\frac{r-R_i}{\gamma}^2\right] + \exp\left[-\frac{r+R_i}{\gamma}^2\right] \right\}, \tag{5.3}$$

with

$$A_i = ZeQ_i \left[2\pi^{3/2}\gamma^3\left(1+\frac{2R_i^2}{\gamma^2}\right)\right]^{-1}, \tag{5.4}$$

where R_i and Q_i are the position and the amplitude of the Gaussians and the values of Q_i are normalized such that $\sum_i Q_i = 1$. R_i, Q_i, and γ in Eq. (5.3) were determined to reproduce the cross sections of the elastic electron scattering. In the form of the two-parameter Fermi model, the charge distribution $\tilde{\rho}_0^c(r)$ is expressed as follows [80],

$$\tilde{\rho}_0^c(r) = \frac{\rho_0}{1 + \exp\left[4.4(r-c)/t\right]}, \tag{5.5}$$

where ρ_0 is the saturation density, and c and t are determined to reproduce the cross sections of the elastic electron scattering. The calculated charge distributions are normalized to satisfy

$$4\pi \int \tilde{\rho}_0^c(r') r'^2 dr' = Ze. \tag{5.6}$$

We calculated the point-proton distributions of the target nuclei by unfolding their charge distributions with the proton charge form factor [81–83]. The charge distribution is expressed using the point-proton distribution ρ_p and the charge distribution of proton $\tilde{\rho}_0^{c,\mathrm{proton}}$ as follows,

$$\tilde{\rho}_0^c(r) = \int \rho_{\mathrm{p}}(\boldsymbol{r'}) \tilde{\rho}_0^{c,\mathrm{proton}}(\boldsymbol{r} - \boldsymbol{r'}) d\boldsymbol{r'}. \tag{5.7}$$

The Fourier transform of Eq. (5.7) is given by,

$$F_c(q) = G_c^p(q) \cdot F_p(q), \tag{5.8}$$

where q, $F_c(q)$, $F_p(q)$, and $G_c^p(q)$ are the momentum transfer, the charge form factor of nucleus (Fourier transform of charge distribution), the form factor of point-proton (Fourier transform of point-proton distribution), and the charge form factor of proton (Fourier transform of proton charge distribution), respectively. $G_c^p(q)$ is also called as Sachs electric form factor of proton [84], and parameterized in Ref. [82] as follows,

$$G_c^p(q) = \frac{1 - 0.24\tau}{1 + 10.98\tau + 12.82\tau^2 + 21.97\tau^3}, \tag{5.9}$$

where $\tau = q^2/4m_{\mathrm{nucleon}}^2$ and m_{nucleon} is the mass of the nucleon. The point-proton distributions are obtained by performing the inverse Fourier transformation of $F_c(q) \cdot [G_c^p(q)]^{-1}$. Since Eq. (5.9) has a node at $\tau = 1/0.24$, it is inappropriate to use Eq. (5.9) directly for the calculation. In the present analysis, another parameterization was utilized in the

calculations as follows [85],

$$G_c^p(q) = \frac{0.312}{1+q^2/6.0} + \frac{1.312}{1+q^2/15.02} - \frac{0.709}{1+q^2/44.08} + \frac{0.085}{1+q^2/154.2}. \tag{5.10}$$

Figure 5.2 shows the experimental data compared with Eq. (5.9), whereas Fig. 5.3 shows the comparison of Eqs. (5.9) and (5.10). As seen in Fig. 5.3, Eqs. 5.9 and 5.10 were satisfactory consistent each other. The point-neutron distributions were assumed to be same with the point-proton distributions for the self-conjugate $A = 4n$ nuclei. The calculated density distribution of the nuclei are shown in Fig. 5.4. The density distributions of ^{58}Ni, ^{90}Zr, ^{116}Sn, ^{144}Sm, and ^{208}Pb were calculated by assuming that the point-proton and point-neutron distributions have the same shape and normalizing $\rho_0(r')$ to satisfy $4\pi \int \rho_0(r')r'^2 dr' = A$. A is the mass number of the nucleus. The density distribution heavier than ^{40}Ca were used to determine the interactions for ^{28}Si and ^{40}Ca in Sec. 5.1.2.

5.1.2 Determination of the effective αN interaction

The parameters in Eq. (5.2) were determined so as to reproduce the cross sections of the elastic alpha scattering. We assumed the same range parameters for real and imaginary parts of the interaction ($\alpha_v = \alpha_w$). The density-dependence parameter β was fixed at -1.9 or 0.0. The parameter value of $\beta = -1.9$ was proposed in Ref. [78], and widely used for the analysis of inelastic alpha scattering [4, 6–13, 16–18, 44, 71]. On the other hand, the parameter value of $\beta = 0.0$ means that the interaction is independent of the density of the target nucleus. For comparison between density-dependent and independent interactions, we determined two different sets of the interaction parameters with $\beta = -1.9$ and 0.0 for each nucleus. In this work, the αN interactions with $\beta = 0.0$ are denoted by "DI" (density independent), whereas those with $\beta = -1.9$ are denoted by "DD" (density dependent).

The calculated cross sections with the best-fit parameter values to the elastic alpha scattering data at $E_\alpha = 386$ and 130 MeV are shown in Figs. 3.14 and 3.15, respectively. The cross sections calculated with the DI and DD interactions are almost the same. Tables 5.1 and 5.2 list the best-fit parameters for the DI and DD interactions at $E_\alpha = 130$ and 386 MeV, respectively. The mass dependence of these parameters are shown in Figs. 5.5–5.8.

As described in Sec. 2.8, there are no available data of the elastic alpha scattering off

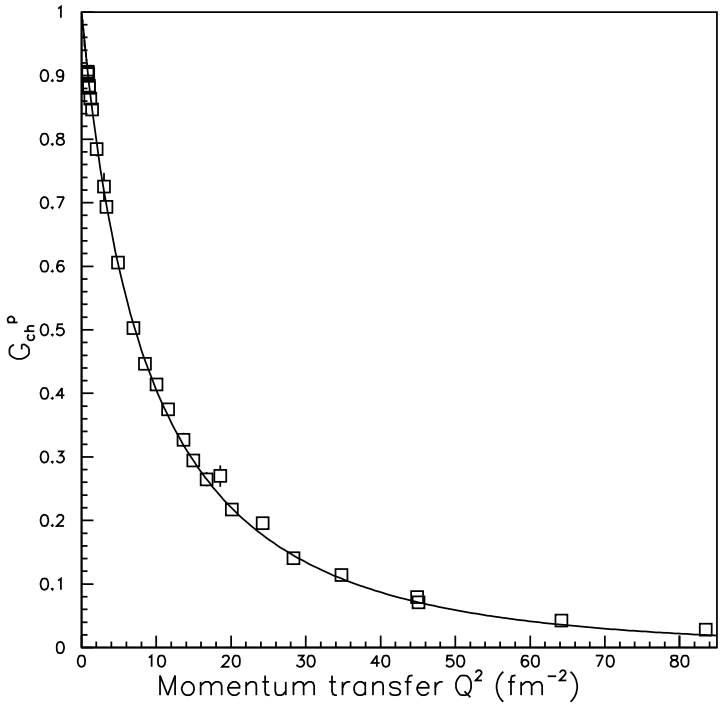

Figure 5.2: Charge form factor of proton (G^p_{ch}) [86–88] compared with Eq. (5.9). Taken from Fig. 4.7 in Ref. [82].

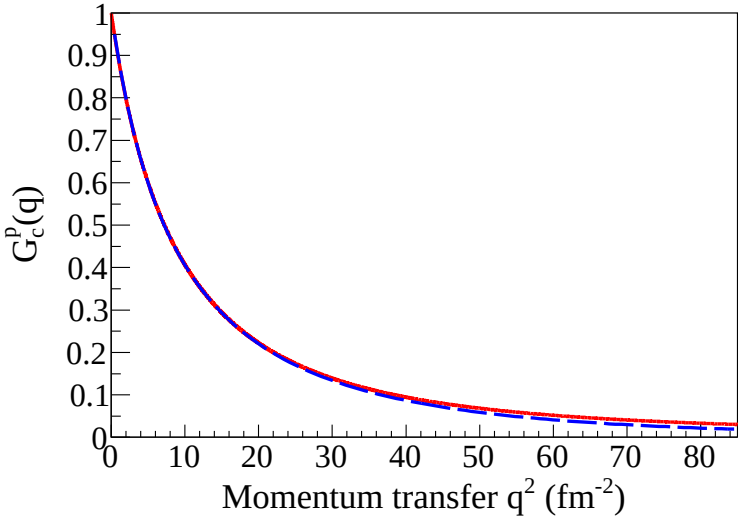

Figure 5.3: Charge form factor of proton (G^p_{ch}) parameterized by Eqs. (5.9) and (5.10). The red solid line and the blue dashed line show Eqs. (5.10) and (5.9), respectively.

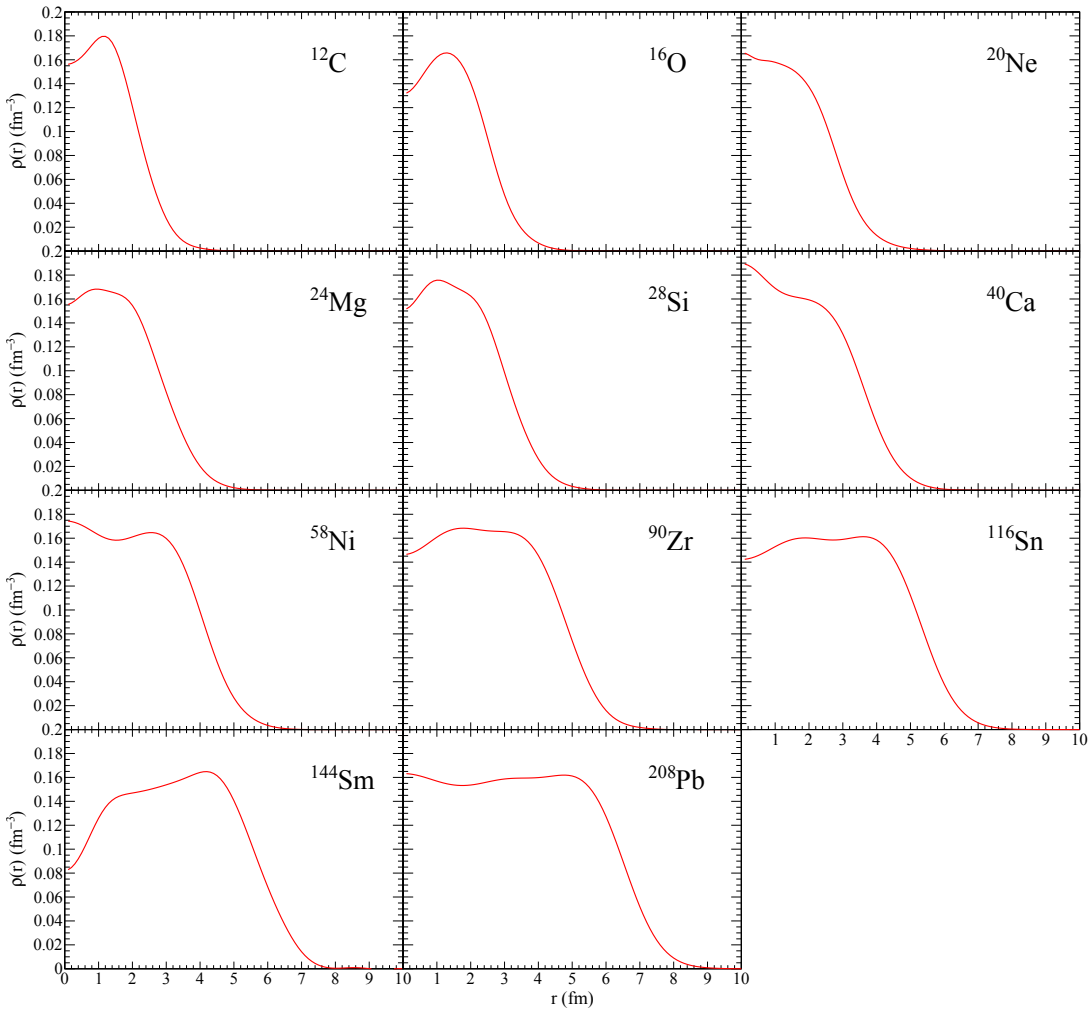

Figure 5.4: Calculated density distributions of the nuclei which are used to analyze the present data.

Table 5.1: Parameterization for the density-independent (DI) and density-dependent (DD) αN interaction at $E_\alpha = 130$ MeV.

Nucleus	Int. type	v (MeV)	w (MeV)	$\alpha_v = \alpha_w$ (fm)	β (fm^2)
^{12}C	DI	22.35	9.90	2.16	0.0
^{16}O	DI	18.48	7.34	2.26	0.0
^{24}Mg	DI	26.61	14.21	2.06	0.0
^{28}Si	DI	39.73	17.82	1.93	0.0
^{40}Ca	DI	36.72	19.25	1.97	0.0
^{12}C	DD	47.65	21.56	1.99	-1.9
^{16}O	DD	48.67	19.56	2.04	-1.9
^{24}Mg	DD	57.85	31.64	1.86	-1.9
^{28}Si	DD	74.36	34.24	1.79	-1.9
^{40}Ca	DD	71.14	37.69	1.81	-1.9

^{28}Si and ^{40}Ca at $E_\alpha = 386$ MeV. Therefore, we could not determine the parameters of the interactions for these nuclei by fitting the cross sections of elastic alpha scattering. We fitted the elastic alpha scattering data of ^{58}Ni, ^{90}Zr, ^{116}Sn, ^{144}Sm, and ^{208}Pb at $E_\alpha = 386$ MeV taken from Refs. [6, 18, 19] and determined the parameters for these nuclei as shown in Figs. 5.5 and 5.6. Although the parameters scattered for the lighter nuclei than ^{24}Mg, we could see the approximate linear relation between the parameters and $A^{1/3}$ for the heavier nuclei. We interpolated the parameters for the heavier nuclei as drawn by the solid lines in Figs. 5.5 and 5.6, and estimated the parameters for ^{28}Si and ^{40}Ca at $E_\alpha = 386$ MeV.

Table 5.2: Parameterization for the density-independent (DI) and density-dependent (DD) αN interaction at $E_\alpha = 386$ MeV.

Nucleus	Int. type	v (MeV)	w (MeV)	$\alpha_v = \alpha_w$ (fm)	β (fm^2)
^{12}C	DI	18.89	13.39	2.01	0.0
^{16}O	DI	20.54	11.07	1.99	0.0
^{20}Ne	DI	20.96	19.69	1.89	0.0
^{24}Mg	DI	14.37	9.05	2.15	0.0
^{28}Si[a]	DI	12.63	8.94	2.11	0.0
^{40}Ca[a]	DI	11.99	8.63	2.13	0.0
^{58}Ni	DI	13.99	8.51	2.11	0.0
^{90}Zr	DI	13.22	7.74	2.17	0.0
^{116}Sn	DI	12.24	7.33	2.21	0.0
^{144}Sm	DI	11.78	6.84	2.23	0.0
^{208}Pb	DI	11.62	6.97	2.29	0.0
^{12}C	DD	41.29	28.24	1.81	−1.9
^{16}O	DD	45.84	24.21	1.78	−1.9
^{20}Ne	DD	46.19	43.00	1.65	−1.9
^{24}Mg	DD	32.41	20.53	1.91	−1.9
^{28}Si[a]	DD	33.99	21.15	1.87	−1.9
^{40}Ca[a]	DD	33.24	20.54	1.89	−1.9
^{58}Ni	DD	34.53	21.05	1.85	−1.9
^{90}Zr	DD	32.93	19.51	1.91	−1.9
^{116}Sn	DD	30.09	18.20	1.96	−1.9
^{144}Sm	DD	28.32	16.49	1.99	−1.9
^{208}Pb	DD	28.00	16.75	2.08	−1.9

[a] The interaction parameters were determined from the global trend. See text for details.

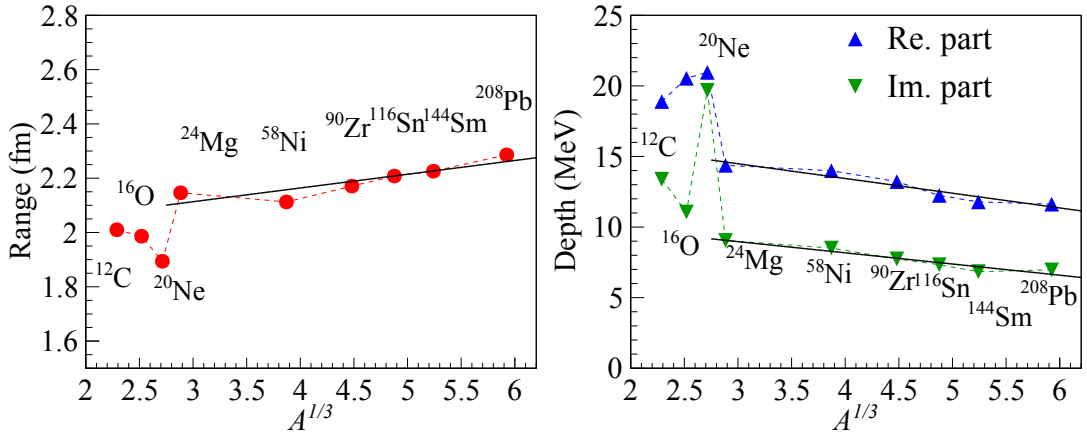

Figure 5.5: Depth and range parameters of the phenomenological density-independent (DI) αN interaction at $E_\alpha = 386$ MeV as a function of $A^{1/3}$. The solid circles show the range parameters $\alpha_v = \alpha_w$, whereas the upward and downward triangles show the real and imaginary depth parameters v and w, respectively. The solid lines are the results of the linear fitting to the parameters at $A =$ 24–208. The dotted lines connect each parameter points to guide the eyes.

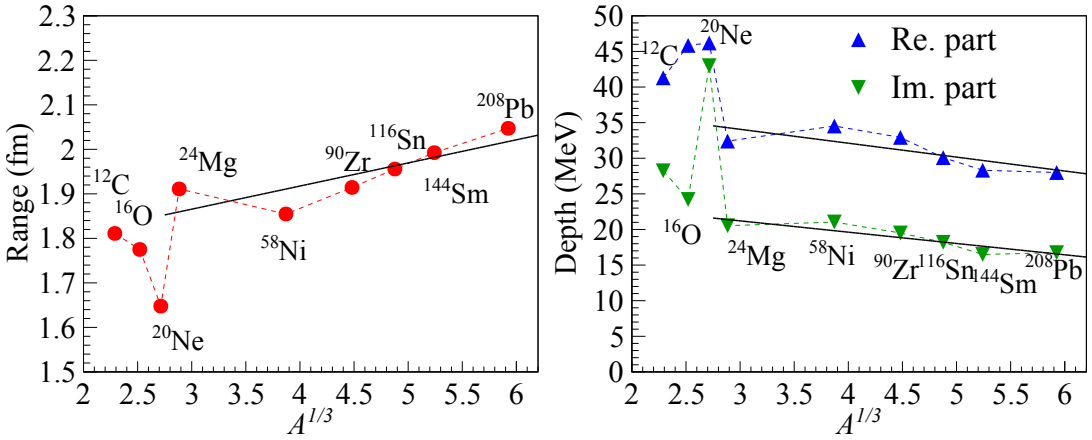

Figure 5.6: Same as Fig. 5.5, but for the DD interaction at $E_\alpha = 386$ MeV.

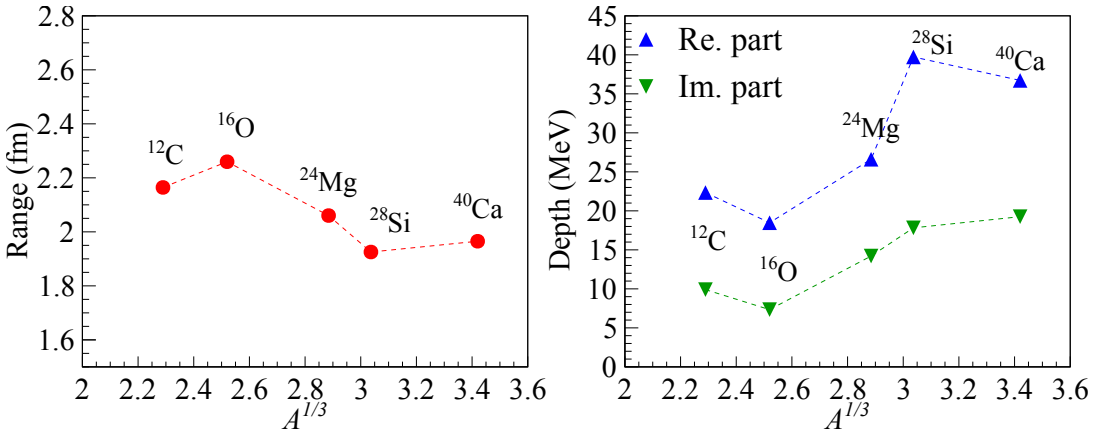

Figure 5.7: Same as Fig. 5.5, but for the DI interaction at $E_\alpha = 130$ MeV.

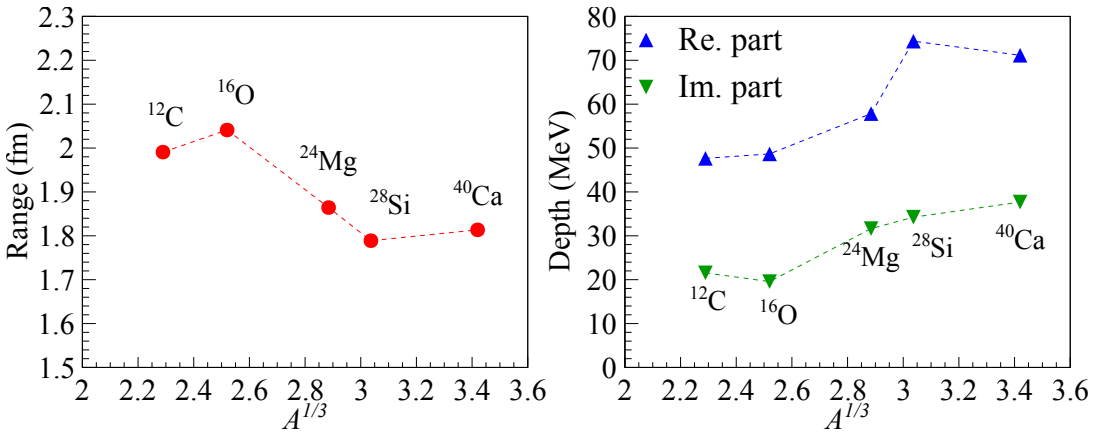

Figure 5.8: Same as Fig. 5.5, but for the DD interaction at $E_\alpha = 130$ MeV.

5.2 Macroscopic transition densities and potentials

5.2.1 Transition densities

We used the macroscopic charge transition densities for isoscalar transitions calculated from the standard macroscopic models [60, 61]. The charge transition density $\tilde{\rho}^{(\lambda)}_{J_f,J_i}(r')$ for a transferred angular momentum λ with the initial-state spin J_i and the final-state spin J_f is given as follows,

$$\tilde{\rho}^{(0)}_{J_f,J_i}(r') = -\alpha_0 \left(3 + r' \frac{d}{dr'}\right) \tilde{\rho}_0(r'), \qquad (\lambda = 0) \tag{5.11}$$

$$\tilde{\rho}^{(1)}_{J_f,J_i}(r') = -\frac{\beta_1}{\sqrt{3}R} \left[3r'^2 \frac{d}{dr'} + 10r - \frac{5}{3}\langle r'^2 \rangle \frac{d}{dr'} + \epsilon \left(r \frac{d^2}{dr'^2} + 4\frac{d}{dr'}\right)\right] \tilde{\rho}_0(r'), \qquad (\lambda = 1) \tag{5.12}$$

$$\tilde{\rho}^{(\lambda)}_{J_f,J_i}(r') = -\delta_\lambda \frac{d}{dr'} \tilde{\rho}_0(r'), \qquad (\lambda \geq 2) \tag{5.13}$$

where α_0 is the dimensionless deformation parameter and δ_λ is the deformation length. $\tilde{\rho}_0(r')$ is the ground-state charge density distribution. β_1, R, and $\langle r'^2 \rangle$ are the collective coupling parameter for the isoscalar dipole resonance, the half-density radius of the Fermi charge distribution, and the root-mean-square radius of the ground-state charge distribution, respectively.

If one excited state at the excitation energy E_x with the transferred angular momentum λ exhausts 100% of the EWSR strength, α_0, β_1, and δ_λ are calculated from the sum rule limit in Ref. [60], Ref. [61], and Refs. [89–91] as follows,

$$\alpha_0^2 = \frac{2\pi\hbar^2}{AmE_x \langle r'^2 \rangle}, \tag{5.14}$$

$$\beta_1^2 = \frac{6\pi\hbar^2}{mAE_x} \frac{R^2}{11\langle r'^4 \rangle - 25/3 \langle r'^2 \rangle^2 - 10\epsilon \langle r'^2 \rangle}, \tag{5.15}$$

$$\delta_\lambda^2 = \frac{\lambda(2\lambda+1)^2}{(\lambda+2)} \frac{2\pi\hbar^2}{AmE_x} \frac{\langle r'^{2\lambda-2} \rangle}{\langle r'^{\lambda-1} \rangle^2}, \tag{5.16}$$

where A and m are the mass number of the target and the nucleon mass, respectively, and $\epsilon = (4/E_2 + 5/E_0)\hbar^2/3mA$. E_2 and E_0 are the excitation energies of the giant quadrupole and monopole resonances, respectively.

The values of α_0 and δ_λ were determined so as to reproduce the known electromagnetic transition strengths [47, 72–76]. We need to pay attention to the fact that the electromagnetic probes are sensitive to protons only in electric transitions, therefore the electric transition strength carried by protons $[B(E\lambda)]$ is generally different from the isoscalar strength $[B(E\lambda; IS)]$ carried by both protons and neutrons [44]. $B(E\lambda)$ and $B(E\lambda; IS)$ with a multipolarity of λ are described as,

$$B(E\lambda) = e^2 \frac{2J_f + 1}{2J_i + 1} |M_p(E\lambda)|^2, \tag{5.17}$$

$$B(E\lambda; IS) = \frac{2J_f + 1}{2J_i + 1} |M_p(E\lambda) + M_n(E\lambda)|^2, \tag{5.18}$$

where M_p and M_n are the proton and neutron transition matrix elements, respectively. We assumed $M_n(E\lambda) = M_p(E\lambda) = M(E\lambda)$ considering the approximately conserved charge symmetry in the light self-conjugate nuclei in the present work, and it leads to be,

$$B(E\lambda; IS) = \frac{4B(E\lambda)}{e^2}. \tag{5.19}$$

$M(E\lambda)$ is calculated from the charge transition density $\tilde{\rho}^{(\lambda)}_{J_f,J_i}(r')$ as follows,

$$M(E0) = \sqrt{4\pi} \int \tilde{\rho}^{(0)}_{J_f,J_i}(r') r'^4 dr', \tag{5.20}$$

$$M(E1) = \int \tilde{\rho}^{(\lambda)}_{J_f,J_i}(r') r'^5 dr', \tag{5.21}$$

$$M(E\lambda) = \int \tilde{\rho}^{(\lambda)}_{J_f,J_i}(r') r'^{\lambda+2} dr' \quad (\lambda \geq 2). \tag{5.22}$$

Therefore, we can determine the amplitudes α_0, β_1, and δ_λ in Eqs. (5.14)–(5.16) from the known electromagnetic transition strengths $B(E\lambda)$ and monopole transition matrix elements. Tables 5.3–5.6 show the excited states measured in the present work whose electromagnetic transition strengths are reported in Refs.[47, 72–76] and the amplitudes in Eqs. (5.14) and (5.16) which were determined to reproduce the $B(E\lambda)$ values.

5.2.2 Transition potentials

Considering the density dependence of the interaction $u\left[|\boldsymbol{r} - \boldsymbol{r}'|, \rho_0(r')\right]$ to the lowest order, the transition potential $\delta U_\lambda(r)$ was obtained by folding the transition density

Table 5.3: Electromagnetic transition strengths $B(E0)$ [47, 72–76] and the deformation parameters α_0 for the $\lambda = 0$ transitions. α_0 is determined to reproduce $B(E0)$ for each transition.

Nucleus	E_x (MeV)	J^π	$B(E0)$ (e^2fm^4)	α_0
^{12}C	7.65	0_2^+	30.3 ± 2.2	0.27 ± 0.01
^{16}O	6.05	0_2^+	11.4 ± 0.8	0.102 ± 0.004
^{16}O	12.05	0_3^+	16.2 ± 0.7	0.121 ± 0.003
^{20}Ne	6.73	0_2^+	55 ± 30	0.15 ± 0.04
^{24}Mg	6.43	0_2^+	44.9 ± 5.4	0.108 ± 0.006
^{28}Si	4.98	0_2^+	46.2 ± 5.4	0.089 ± 0.005
^{40}Ca	3.35	0_2^+	7.3 ± 0.2	0.0199 ± 0.003

Table 5.4: Electromagnetic transition strengths $B(E2)$ [47, 72–76] and the deformation lengths δ_2 for the $\lambda = 2$ transitions. δ_2 is determined to reproduce $B(E2)$ for each transition.

Nucleus	E_x (MeV)	J^π	$B(E2)$ (e^2fm^4)	δ_2 (fm)
^{12}C	4.44	2_1^+	38 ± 2	1.42 ± 0.04
^{16}O	6.92	2_1^+	37 ± 1	1.02 ± 0.01
^{16}O	9.84	2_2^+	0.67 ± 0.06	0.127 ± 0.006
^{16}O	11.52	2_3^+	18.2 ± 0.8	0.67 ± 0.01
^{20}Ne	1.63	2_1^+	330 ± 16	2.04 ± 0.05
^{24}Mg	1.37	2_1^+	426 ± 9	1.93 ± 0.02
^{24}Mg	4.24	2_2^+	33 ± 2	0.53 ± 0.02
^{24}Mg	7.35	2_3^+	11.6 ± 4.6	0.31 ± 0.06
^{24}Mg	9.00	2_5^+	3.2 ± 0.7	0.17 ± 0.02
^{24}Mg	10.36	2_7^+	6.5 ± 1.6	0.24 ± 0.03
^{28}Si	1.78	2_1^+	327 ± 6	1.38 ± 0.01
^{28}Si	7.93	2_2^+	7.6 ± 1.1	0.19 ± 0.01
^{28}Si	8.26	2_3^+	6.9 ± 2.7	0.20 ± 0.04
^{28}Si	9.48	2_4^+	3.4 ± 1.6	0.178 ± 0.04
^{40}Ca	3.90	2_1^+	90 ± 6	0.46 ± 0.02
^{40}Ca	8.09	2_2^+	26.2 ± 1.8	0.250 ± 0.009
^{40}Ca	8.58	2_3^+	12.3 ± 1.6	0.17 ± 0.01

Table 5.5: Electromagnetic transition strengths $B(E3)$ [47, 72–76] and the deformation lengths δ_3 for the $\lambda = 3$ transitions. δ_3 is determined to reproduce $B(E3)$ for each transition.

Nucleus	E_x (MeV)	J^π	$B(E3)$ ($e^2\text{fm}^6$)	δ_3 (fm)
^{12}C	9.64	3^-_1	$(7.2 \pm 0.4) \times 10^2$	1.84 ± 0.05
^{16}O	6.13	3^-_1	$(1.38 \pm 0.04) \times 10^3$	1.59 ± 0.02
^{20}Ne	5.62	3^-_1	$(1.8 \pm 0.3) \times 10^3$	1.2 ± 0.1
^{24}Mg	7.62	3^-_1	$(1.5 \pm 0.3) \times 10^3$	0.90 ± 0.097
^{24}Mg	8.36	3^-_2	$(2.6 \pm 0.7) \times 10^3$	1.19 ± 0.16
^{28}Si	6.88	3^-_1	$(4.4 \pm 0.7) \times 10^3$	1.25 ± 0.10
^{40}Ca	3.74	3^-_1	$(1.72 \pm 0.08) \times 10^3$	1.35 ± 0.03
^{40}Ca	6.29	3^-_2	$(2.0 \pm 0.4) \times 10^3$	0.46 ± 0.05

Table 5.6: Electromagnetic transition strengths $B(E4)$ [47, 72–76] and the deformation lengths δ_4 for the $\lambda = 4$ transitions. δ_4 is determined to reproduce $B(E4)$ for each transition.

Nucleus	E_x (MeV)	J^π	$B(E4)$ ($e^2\text{fm}^8$)	δ_4 (fm)
^{16}O	10.36	4^+_1	$(3.4 \pm 1.2) \times 10^3$	0.64 ± 0.11
^{20}Ne	4.25	4^+_1	$(3.8 \pm 0.8) \times 10^4$	1.28 ± 0.13
^{24}Mg	4.12	4^+_1	$(2.6 \pm 0.4) \times 10^3$	0.28 ± 0.02
^{24}Mg	6.01	4^+_2	$(3.5 \pm 0.8) \times 10^4$	1.01 ± 0.12
^{28}Si	4.62	4^+_1	$(1.8 \pm 0.2) \times 10^4$	0.56 ± 0.03

$\rho^{(\lambda)}_{J_f,J_i}(r')$ with $u\left[|\boldsymbol{r}-\boldsymbol{r}'|,\rho_0(r')\right]$ as follows,

$$\begin{aligned}\delta U_\lambda(r) &= \int dr' \rho^{(\lambda)}_{J_f,j_i}(r') \\ &\times \left[u\left[|\boldsymbol{r}-\boldsymbol{r}'|,\rho_0(r')\right] + \rho_0(r')\frac{\partial u\left[|\boldsymbol{r}-\boldsymbol{r}'|,\rho_0(r')\right]}{\partial \rho_0(r')}\right]. \end{aligned} \tag{5.23}$$

The transition density $\rho^{(\lambda)}_{J_f,J_i}(r')$ is given by unfolding the charge transition density $\tilde{\rho}^{(\lambda)}_{J_f,J_i}(r')$ with the proton-charge form factor.

5.3 The DWBA calculation

From the formalism described in Secs. 5.1 and 5.2, we calculated the optical-model potential for the entrance channel $U(r)$ and the transition potential $\delta U_\lambda(r)$. The optical-model potential for the exit channel were assumed to be same as that of the entrance channel in the present calculation. Thus, we performed the DWBA calculations for the transitions whose strengths are known using the computer code ECIS-95 [77], and the calculated cross sections are shown by the solid and dashed lines in Figs. 4.1–4.8. The solid and dashed lines in the figures show the calculated cross sections using the DI and DD interactions, respectively. The errors of the cross sections arose from the uncertainties of the electromagnetic transition strengths are drawn for the DI interaction only for simplicity.

It should be noted that there is no adjustable parameter in the present DWBA calculation because the αN interaction and transition densities are already adjusted by the elastic alpha scattering data and the known $B(E\lambda)$ values.

Chapter 6

Discussion

6.1 Comparison between experimental data and DWBA calculations

The measured cross sections of the inelastic alpha scattering are compared with the calculation using the DI and DD interactions in Fig. 4.1–4.7. Since the experimental cross sections were obtained for the angular bins with a width of 0.4°, the calculated cross sections at each angle are averaged over the angular range of ±0.2°.

As shown for the $\Delta L = 0$ transitions in Figs. 4.1 and 4.2, the calculated cross sections with the DD interactions are systematically larger than the measured cross sections. This discrepancy is consistent with the previous results in Refs. [20, 58]. However, it should be noted that the DWBA calculations using the DD interaction overestimate the cross sections for not only the Hoyle state but also most of the 0^+ states in ^{16}O, ^{20}Ne, ^{24}Mg, ^{28}Si, and ^{40}Ca. This result suggests that the "missing monopole strength" is not specific to the Hoyle state but universal for the $\Delta L = 0$ transitions. On the other hand, the calculated cross sections with the DI interactions are systematically smaller than those with the DD interactions, and are close to the measured cross sections. Especially, the calculation at $E_\alpha = 386$ MeV reasonably well reproduces the experimental data, and does not exhibit the puzzling situation about the missing monopole strength for the Hoyle state.

The measured cross sections of the 0^+_2 states in ^{16}O and ^{40}Ca are much smaller than the calculations as seen in Fig. 4.2. The angular distributions of the measured cross sections for the 0^+_2 states are quite different from the calculations. The reason of the

discrepancy is still unclear. Note that both of these states are the first excited states in the double closed nuclei.

For the $\Delta L = 2$ transitions shown in Figs. 4.3 and 4.4, the DWBA calculations using the DI and DD interactions give almost the same results, and reasonably reproduce the angular distributions of the cross sections except for the several states. For the 2^+_2 state in ^{16}O and the 2^+_3 state in ^{28}Si, the calculated angular distributions of the cross sections are considerably different from the experimental data. The measured cross sections for these 2^+ states are smaller than 1 mb/sr. Since the direct couplings between the ground states and these states are weak, the multi-step processes would be important to reproduce the cross sections for these states.

For the 2^+_3 and 2^+_5 states in ^{24}Mg, the angular distributions of the measured cross sections slightly shift to forward angles compared with the DWBA calculations. This shift would be understandable if we assume that the radii of these states are larger than those of the usual states. In Refs. [92, 93], it was theoretically shown that the angular distribution of inelastic cross sections for the $\Delta L = 0$ transition is not sensitive to the radial expansion of the excited states. However, the recent theoretical study suggests that the situation in the $\Delta L = 2$ transition is different from the $\Delta L = 0$ transition [94]. The shift of the angular distribution due to the radial expansion of the excited states is more visible in the $\Delta L = 2$ transition than in the $\Delta L = 0$ transition, and is more visible at lower reaction energies than at higher reaction energies. This is consistent with the present results that the shift in the angular distribution is more visible at $E_\alpha = 130$ MeV than at $E_\alpha = 386$ MeV.

For the $\Delta L = 3$ and 4 transitions shown in Figs. 4.5–4.7, the differences between the calculations with the DI and DD interactions are small, although the DI interaction gives slightly smaller cross sections.

6.1.1 Normalization factor for the calculated cross sections to fit the experimental data

The calculated cross sections for the (α, α') reactions at $E_\alpha = 386$ MeV are fitted to the experimental data by applying the normalization factor R. If the present DWBA calculation is correct, R should be unity. The normalization factor R is shown in Fig. 6.1 for the $\Delta L = 0$, 2, and 3 transitions. The R values for the DI interaction are systematically closer to the unity than those for the DD interaction, although the R values for the 0^+_3

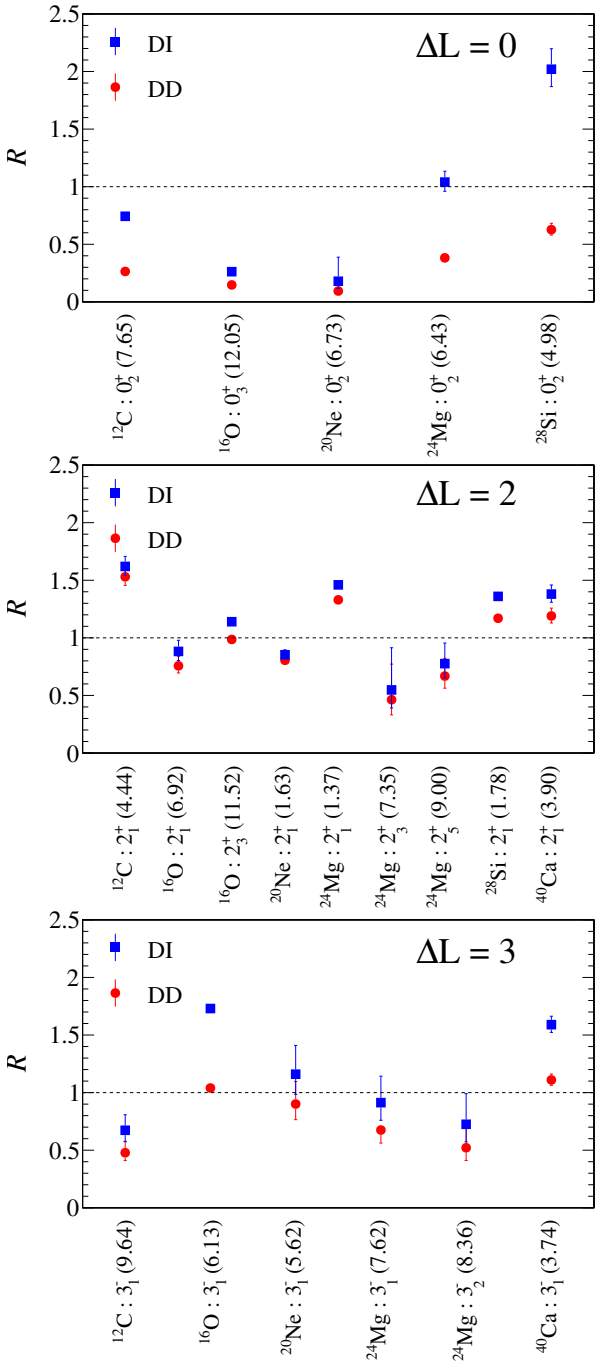

Figure 6.1: Normalization factors for the calculated cross sections for the (α, α') reactions at $E_\alpha = 386$ MeV to fit the experimental data. The solid squares and circles are the normalization factors for the calculations with the DI and DD interactions. The errors arise from the known electromagnetic transition transitions [47, 57, 72–76]

state in ^{16}O and, the 0_2^+ states in ^{20}Ne and in ^{28}Si significantly deviate from the unity.

The cross section for the 0_2^+ states in ^{20}Ne calculated with the DI interaction is consistent with the experimental data at 0° within the error due to the uncertainty from the electromagnetic transition strength. However, the disagreement between the calculation and the experiment around the diffraction minimum causes the deviation of R from the unity.

The cross section of the 0_2^+ state in ^{28}Si was not measured at 0°. Since the cross sections near 0° are crucial for the reliable determination of the isoscalar monopole transition strength, further measurements for these states should be done.

As discussed above, the DWBA calculation with the DI interaction gives a better description for inelastic alpha scattering than those with the DD interaction. Furthermore, the DI interaction at $E_\alpha = 386$ MeV is more applicable to fit the experimental data than that at $E_\alpha = 130$ MeV. This situations is naturally understood from the well-known fact that direct processes are dominant and the reaction mechanism becomes simple above $E \sim 100$ MeV/u.

6.2 Characteristics of the macroscopic transition densities and potentials

The transition densities and potentials in the present folding-model analyses should be examined in order to clarify the reason why the DI and DD interactions give the different results for the $\Delta L = 0$ transitions (see Figs. 4.1 and 4.2). Figure 6.2 shows the transition densities and potentials calculated based on the macroscopic model for the transitions between the ground and excited states in ^{12}C at $E_\alpha = 386$ MeV.

The DI and DD interactions give similar potentials for the 2_1^+ state, whereas these two interactions give significantly different transition potentials for the 0_2^+ state. The transition density for the $\Delta L = 0$ transition has sizable values around the center of a nucleus ($r = 0$). Since the DD interaction is much weaker than the DI interaction around the origin due to the density effect, the DD transition potential for the $\Delta L = 0$ transition is much shallower than the DI transition potential in the inner region. On the other hand, the transition density for the $\Delta L = 2$ transition is almost zero at the origin. Therefore, the DI and DD transition potentials are almost same for the $\Delta L = 2$ transition.

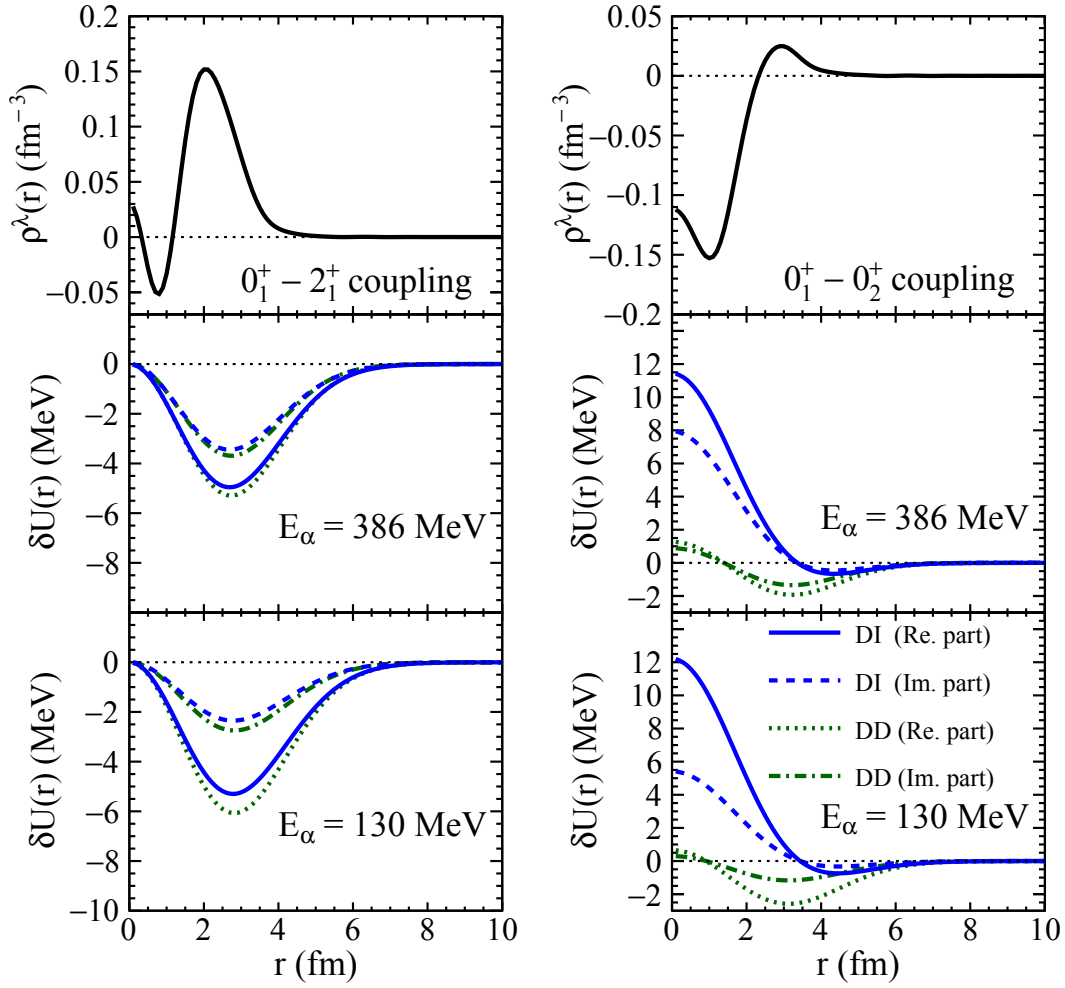

Figure 6.2: Transition densities given by Eqs. (5.11) and (5.13), and the transition potentials with the phenomenological αN interaction. The top panels show the transition densities, and the middle and bottom show the transition potentials for the $0_1^+ - 2_1^+$ and $0_1^+ - 0_2^+$ transitions in ^{12}C at $E_\alpha = 386$ MeV and $E_\alpha = 130$ MeV, respectively. The solid and dashed lines show the real and imaginary parts of the transition potentials with the DI interaction. The dotted and dot-dashed lines show the real and imaginary parts of the potentials with the DD interaction.

Historically, the density dependence of the phenomenological αN interaction was introduced to obtain better description of elastic alpha scattering at backward angles [78]. Although the depth and range parameters used for the DI and DD interactions are determined to fit elastic alpha scattering, cross sections of elastic alpha scattering are sensitive to the nuclear wave functions at the surface only because of the strong absorption [95]. Since the interaction parameters are basically tuned at the surface where the nuclear density is relatively low, in the present work, the DD interaction gives a good description for the $\Delta L = 2$ transition whose transition density enhances near the surface, but does not for the $\Delta L = 0$ transition in which the interior transition density gives a sizable contribution to the transition potential. The weak absorption by the DD transition potential for the $\Delta L = 0$ transitions causes the systematic overestimation of the cross sections and "missing monopole strengths". However, the R values for the $\Delta L = 0$ transitions in Fig. 6.1 shows that the DWBA calculation with the DI interaction is still unsatisfactory, and this fact suggests that the treatment of the density dependence in the present effective αN interaction given in Eq. (5.2) is not suitable to describe the inelastic alpha scattering.

It is noteworthy that the transition potential for the 0^+_1–0^+_2 transition from the recent full microscopic calculation using the realistic NN interaction [96] is similar to the DI transition potential for the $\Delta L = 0$ transition as shown in Fig. 6.3. Note that the sign of the potential in Fig. 6.3 is different from that in the present calculation in Fig. 6.2 due to the different definition of the sign. This fact suggests that a sophisticated effective αN interaction could be constructed from the realistic NN interaction, and such an interaction might give better description than the present empirical effective αN interaction.

6.2.1 Dependence on the nuclear size

We found that the DI interaction at $E_\alpha = 386$ MeV is better than the DD interaction to reproduce the experimental cross sections, but the DD interaction was widely used to analyze the alpha scattering data, especially for the study of the ISGMRs [3–9, 17]. The difference between the DI and DD interactions should be checked by calculating the cross sections to the 0^+_2 and 2^+_1 states in ^{40}Ca, ^{90}Zr, ^{116}Sn, and ^{208}Pb. All the procedures to calculate the cross sections are same as in Sect. 5.3, but the transition strengths are set at 100% of the EWSR strength. The calculated cross sections and transition potentials

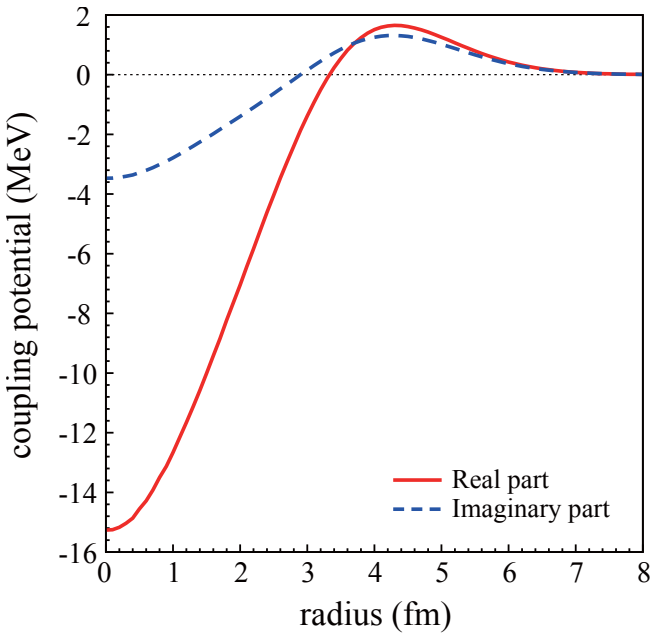

Figure 6.3: The transition potential for the 0_1^+–0_2^+ transition in the ^{12}C(α, α') reaction at $E_\alpha = 172.5$ MeV in Ref. [96]. Taken from Fig. 4 in Ref. [96].

are shown in Fig. 6.4 for the 0_2^+ states and in Fig. 6.5 for the 2_1^+ states. We can find that the difference between the cross sections calculated with the DI and DD interactions is smaller for heavier nuclei as shown by the values denoted as "ratio" in Fig. 6.4 which are the ratios of the calculated cross sections at 0° with the DD interaction to those with the DI interaction. We can understand this result from the fact that the inelastic alpha scattering comes to less sensitive to the inner region with increasing nuclear radii because the alpha particles are absorbed before they reach the inner region.

Eventually, the difference between the DI and DD interactions decreases with increasing nuclear size, however, it is not negligible for the determination of the nuclear incompressibility. Although the shapes of the angular distribution of the cross section calculated with the DD interaction is quite similar to those with the DI interaction, the absolute values of the cross sections with the DD interaction are larger than those with the DI interaction. Thus, the shape of the strength distribution of the isoscalar monopole transition estimated by the MDA with the DD interaction are similar to those with the DI interaction, but the isoscalar monopole transition strengths estimated with the DD interaction are much smaller than those with the DI interaction. For the determination of the nuclear incompressibility, we need to reliably determine the averaged energy over

the isoscalar monopole transitions exhausting most of the EWSR strengths as discussed in Sec. 1.2.1. If the observed EWSR fraction is much smaller than the EWSR limit due to the puzzle of the missing monopole strengths, the estimated K_A values must be reconsidered. Therefore, the density dependence of the phenomenological αN interaction should be treated carefully even for the heavy nuclei such as ^{208}Pb.

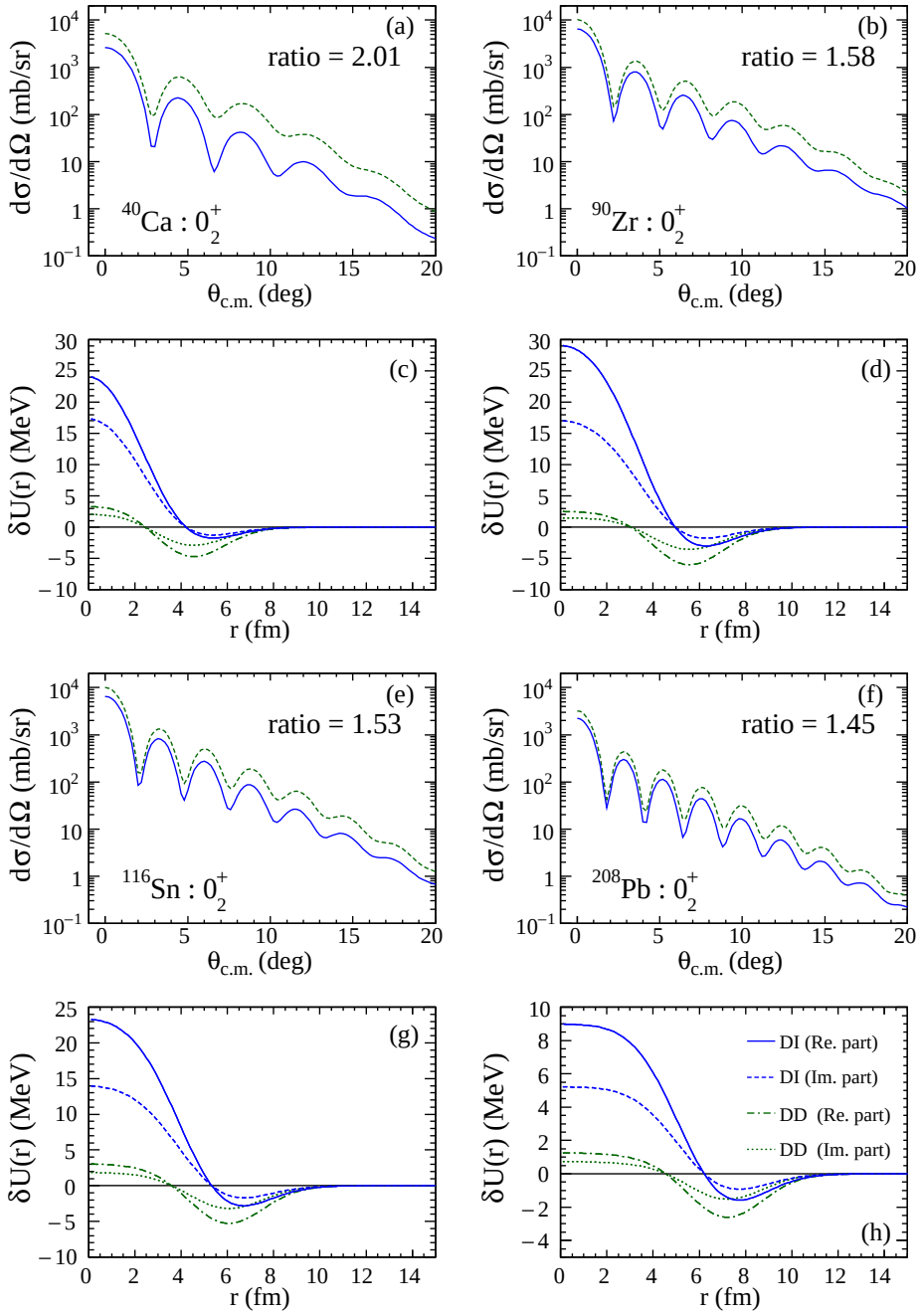

Figure 6.4: (a),(b),(e), and (f); Calculated cross sections of the inelastic alpha reaction to the 0^+_2 states in ^{40}Ca, ^{90}Zr, ^{116}Sn, and ^{208}Pb at $E_\alpha = 386$ MeV. The solid and dashed lines are the results with the DI and DD interactions, respectively. Each transition strength is set at 100% of the EWSR strength.
(c),(d),(g), and (h); The transition potentials for the reactions of (a),(b),(e), and (f), respectively.

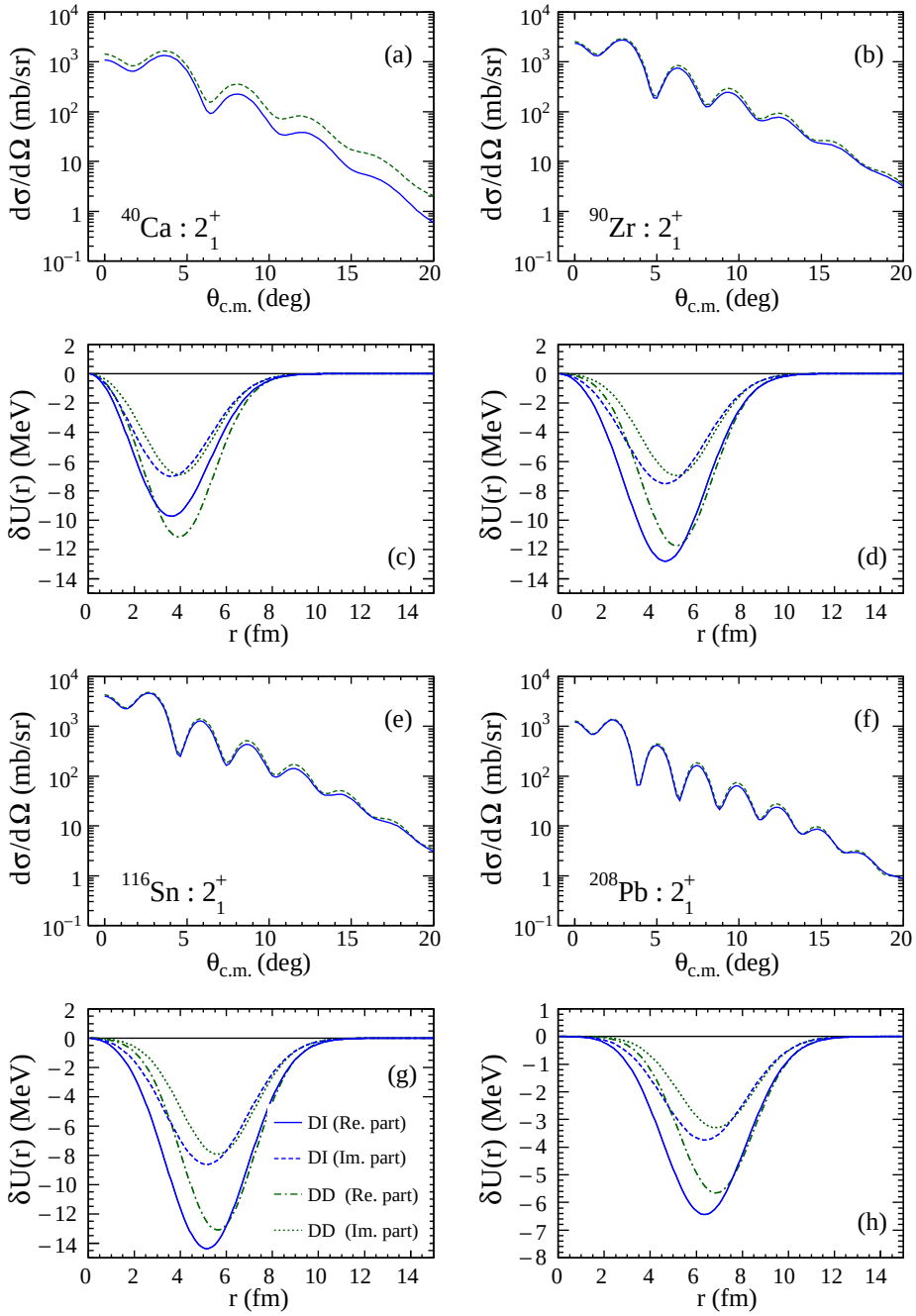

Figure 6.5: Same as Fig. 6.4, but for the 2^+_1 states.

6.3 Ambiguity in the DWBA calculations

Several approximations are introduced to the present DWBA analyses. (i) The macroscopic transition densities are used instead of the realistic microscopic transition densities. (ii) The distorting potentials for the exit channels are assumed to be the same with the entrance channels. (iii) The interactions are approximated by the Gaussian-type phenomenological αN interaction. (iv) The coupled-channel effects are ignored.

These approximations might cause errors in the present analyses. Ambiguities from these approximations are discussed in the following by comparing the present DWBA calculations with the reliable microscopic calculations. However, such reliable macroscopic calculations are available only for several nuclei such as ^{12}C and ^{16}O, therefore, the ambiguities in ^{12}C are discussed in this section.

Only the calculations with the DI interaction at $E_\alpha = 386$ MeV are shown because the situation does not essentially change even for other cases; for example, the DD interaction or at $E_\alpha = 130$ MeV.

6.3.1 Transition densities

The macroscopic transition densities for the 2^+_1, 0^+_2, and 3^-_1 states given by Eqs. (5.11) and (5.13) are shown by the solid lines in the bottom panels of Fig. 6.6. In addition, the dashed lines represent the microscopic transition densities for the 0^+_1–2^+_1 and 0^+_1–0^+_2 transitions from the α-particle condensate wave functions (so-called THSR wave functions) [97, 98] and the transition density for the 0^+_1–3^-_1 transition from 3α RGM calculations [40]. The amplitudes of the microscopic transition densities are normalized to reproduce the known electromagnetic transition strengths [47, 57, 72–76]. The microscopic transition densities are considerable different from the macroscopic transitions densities.

The cross sections for the 2^+_1, 0^+_2, and 3^-_1 states at $E_\alpha = 386$ MeV obtained from the DWBA calculations using the microscopic and macroscopic transition densities are compared in the top panels of Fig. 6.6. The solid lines are the same calculations as described in Sect. 5.3 using the DI interaction and the macroscopic transition densities. The dashed lines are the calculations using the DI interaction and the microscopic transition densities. The differences between the solid and dashed lines are very small for all of the 2^+_1, 0^+_2 and 3^-_1 states in spite of the differences in the transition densities. although the macroscopic transition densities shown by the solid lines in the bottom

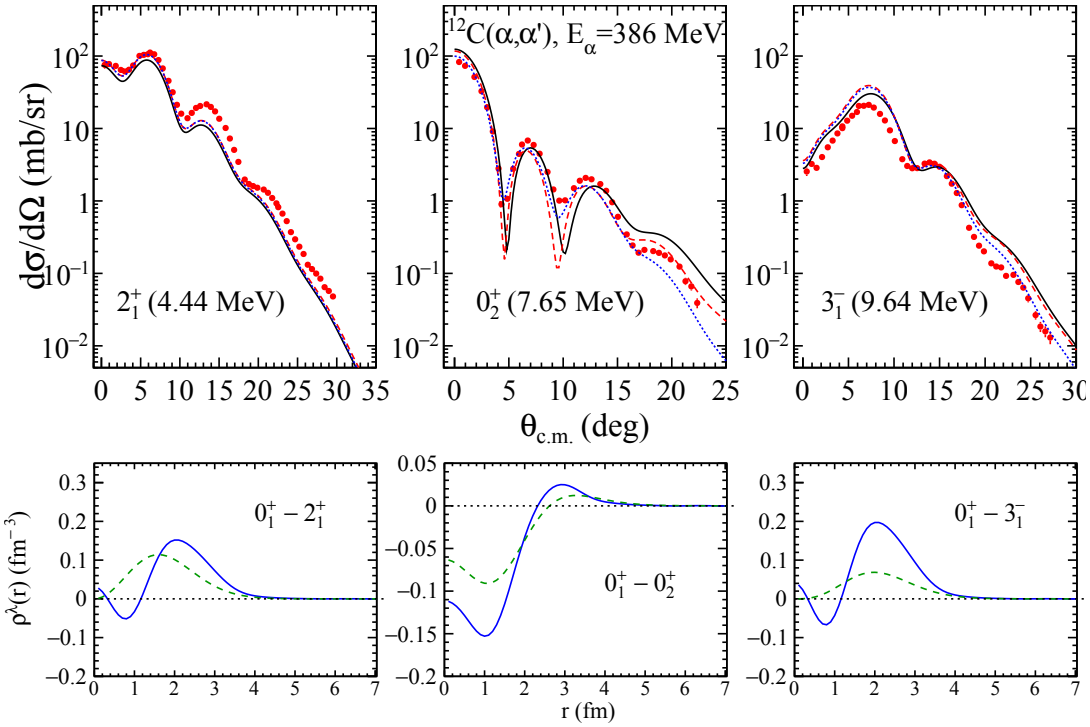

Figure 6.6: Calculated cross sections and transition densities for the 2^+_1, 0^+_2, and 3^-_1 states in ^{12}C at $E_\alpha = 386$ MeV. The solid circles with error bars are the experimental data. The solid lines show the DWBA calculations using the DI interaction and macroscopic transition densities which are same with the solid lines in Figs. 4.1, 4.3, and 4.5. The dashed lines show the DWBA calculations using the DI interaction and the microscopic transition densities from Ref. [40, 97, 98]. The dotted lines are the same DWBA calculations shown by the dashed lines except that the distorting potentials for the exit channels are calculated by folding the density distributions of the excited states with the DI interaction. The dashed and dotted lines are almost the same for the 2^+_1 and 3^-_1 states. In the bottom panels, the solid lines show the macroscopic transition densities given by unfolding the macroscopic charge transition densities [Eqs. (5.11) and (5.13)] with the proton charge form factor, whereas the dashed lines are the microscopic transition densities (See text).

panels are considerably different from the microscopic transition densities. These results show that the ambiguities due to differences in transition densities are negligibly small in the present DWBA calculation.

6.3.2 Distorting potentials

In order to examine ambiguities from the distorting potentials, we replace the distorting potentials for the exit channels with the diagonal potentials for the excited states. The diagonal optical-model potentials are calculated by folding the density distributions of the excited states from Refs. [40, 97, 98] with the DI interaction. The calculated cross sections are represented by the dotted lines in the top panels of Fig. 6.6. The cross sections for the 2_1^+ and 3_1^- states do not change even if the distorting potentials are replaced. For the 0_2^+ state, on the other hand, the cross sections slightly change when the distorting potentials are replaced. This result is explained from the fact that the radius of the 0_2^+ state is much larger than that of the ground state [40, 97, 98] and thus, the distorting potential for the exit channel is very different from that for the entrance channel. However, the variation of the cross sections due to the distorting potential is acceptably small.

6.3.3 Phenomenological αN interaction

The present DWBA calculation using the single-folding potentials assumes the α particle is point particle, and the phenomenological αN interaction is empirically determined to reproduce elastic alpha scattering. This interaction is really phenomenological, and hence it does not established on the realistic NN interaction. The present DWBA calculation should be compared with the calculation using the realistic NN interaction. In the following calculations, we used the diagonal potentials for the excited states as the distorting potential for the exit channels as performed in Sec. 6.3.2.

For comparison, we carried out the DWBA calculation using the NN G-matrix interaction by the Melbourne group [99]. The transition potentials were calculated by doubly folding the projectile density distribution and the target transition-density distribution with the NN G-matrix interaction. The density distributions used with the NN G-matrix interaction are taken from the 3α RGM calculation [40] as the same prescription with Ref. [96]. The calculated cross sections for the 2_1^+, 0_2^+, and 3_1^- states in ^{12}C with the Melbourne and DI interactions are shown by the solid and dashed lines in Fig. 6.7,

respectively. The dashed lines calculated with the DI interaction are same with the dotted lines in the top panels of Fig. 6.6. Both the calculations reasonably reproduce the diffraction pattern of the measured cross sections. The cross sections with the DI interaction are systematically smaller than those with the Melbourne interaction, and are close to the experiment.

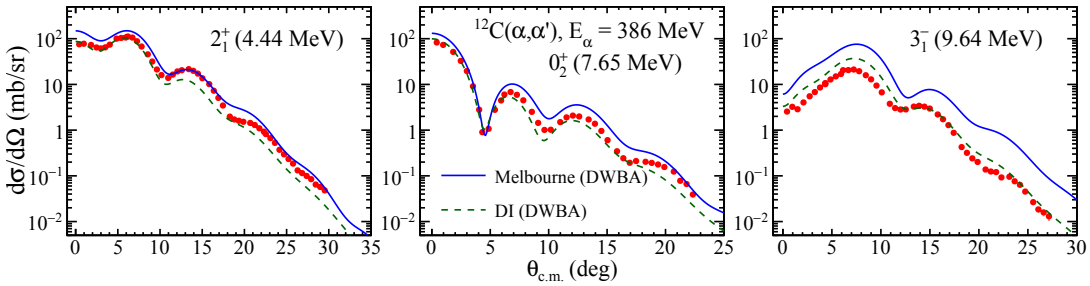

Figure 6.7: Calculated cross sections of the inelastic alpha scattering at $E_\alpha = 386$ MeV exciting the 2_1^+, 0_2^+, and 3_1^- states in ^{12}C. The solid and dashed lines show the DWBA calculations with the Melbourne [99] and DI interactions, respectively. The solid circles with error bars are the experimental data.

6.3.4 Coupled-channel effect

The coupled-channel (CC) effect is ignored in the present DWBA calculation, but it might not be negligible. Especially, it is pointed out that the coupling between the 0_2^+ and 2_2^+ states in ^{12}C is very strong [40, 100]. The CC calculation for the inelastic alpha scattering exciting the 2_1^+, 0_2^+, and 3_1^- states in ^{12}C using the DI interaction at $E_\alpha = 386$ MeV was compared with the DWBA calculation in the top panels of Fig. 6.8. The distorting and transition potentials are calculated by using the wave functions from the 3α RGM calculation for the 3_1^- state [40] and the THSR wave functions for the 0_1^+, 2_1^+, 0_2^+, 2_2^+, and 4_1^+ states [97, 98].

The dotted lines show the CC calculation taking into account the coupled-channel effects between the 6 states (0_1^+, 2_1^+, 0_2^+, 3_1^-, 2_2^+, and 4_1^+), while the dashed lines show the CC calculation taking into account the coupled-channel effects between the 5 states except the 2_2^+ state. The solid lines show the DWBA calculation, which is the same with the dashed lines in Fig. 6.7. The CC effects for the 2_1^+ and 3_1^- states are negligibly small, and the DWBA and CC calculations give similar results except for the 0_2^+ state. The DWBA and 5-state CC calculations give similar results even for the 0_2^+ state, but the 6-state CC calculation gives smaller cross section at forward angles than the other

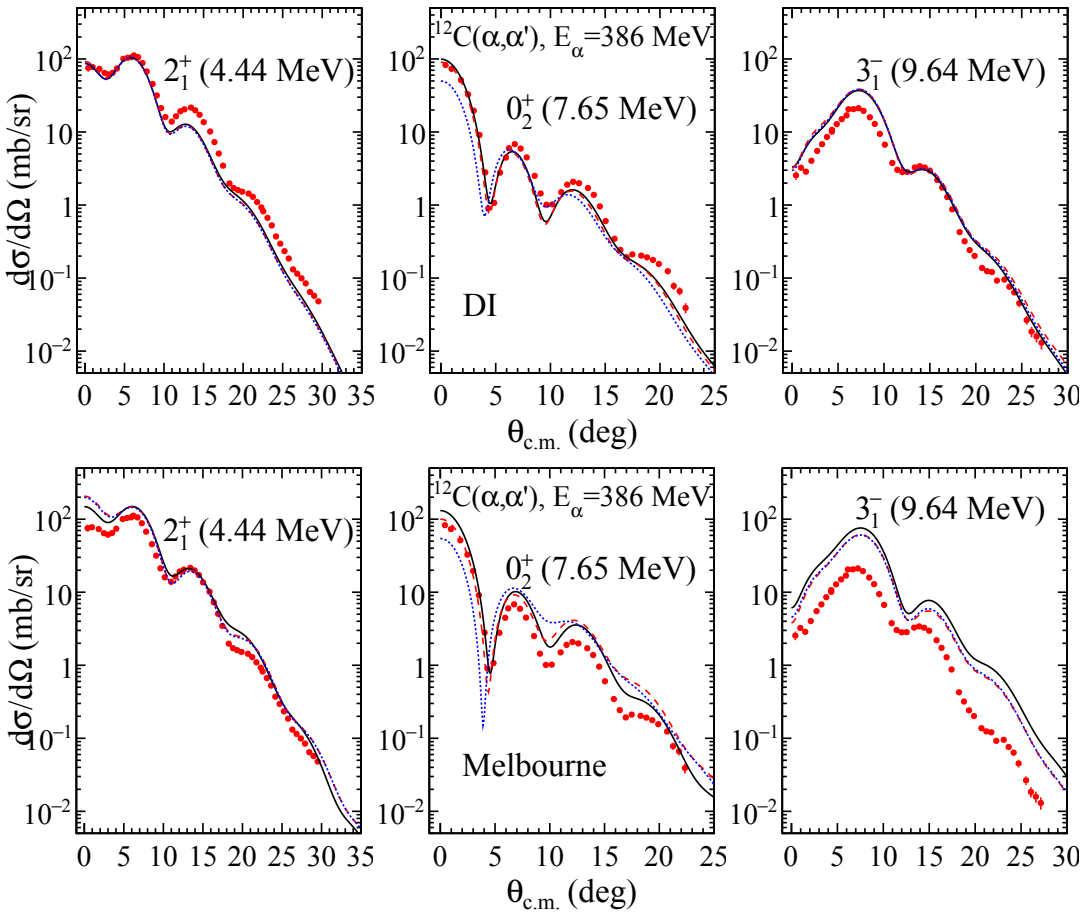

Figure 6.8: Calculated cross sections of inelastic alpha scattering at $E_\alpha = 386$ MeV exciting the 2_1^+, 0_2^+, and 3_1^- states in ^{12}C. The top panels are the DWBA and CC calculations with the DI interaction, and the bottom panels are the calculations with the Melbourne interaction [96]. The solid lines show the DWBA calculation. The dotted and dashed lines respectively show the 6-state and 5-state CC calculations (see text). The dotted and dashed lines are almost the same for the 2_1^+ and 3_1^- states. The solid circles with error bars are the experimental data.

calculations. In addition, the diffraction pattern of the angular distribution in the 6-state CC calculation slightly shifts to forward angles. This result reflects the fact that the coupling between the 0_2^+ and 2_2^+ states is strong.

The reduction of the cross section for the 0_2^+ state is essentially the same phenomenon with the enhanced absorption in the $\alpha+^{12}\mathrm{C}(0_2^+)$ channel proposed in Ref. [58]. It should be noted that the DWBA calculations are better to reproduce the experimental data than the 6-state CC calculation. One possible explanation is that the coupling between the 0_2^+ and 2_2^+ states in the present CC calculation is too strong. The transition strength between the 0_2^+ and 2_2^+ states has never been measured, therefore the experimental study is strongly desired.

Recently, a full microscopic calculation of the inelastic alpha scattering from ^{12}C using the Melbourne NN G-matrix interaction was performed [96]. The CC calculations reported in Ref. [96] are shown in the bottom panels of Fig. 6.8. The dotted and dashed lines show the 6-state and 5-state CC calculations, respectively. On the other hand, the solid lines show the DWBA calculations same with the solid lines in Fig. 6.7. The situation is quite similar to the calculation with the DI interactions. The coupling to the 2_2^+ state is negligibly small for the 2_1^+ and 3_1^- states but not for the 0_2^+ state. The 6-state CC calculation gives smaller cross sections of the 0_2^+ state than the 5-state CC calculations at forward angles, and the diffraction pattern of the angular distribution in the 6-state CC calculation slightly shifts to forward angles. The full microscopic CC calculation slightly underestimates the experimental cross sections for the 0_2^+ state at forward angles and overestimates at backward angles. The three-nucleon force possibly decreases the cross section at backward angles and improves the calculation as discussed in Ref. [96].

As discussed above, the CC effects are negligibly small in most cases of the inelastic alpha scattering although the CC effects sometimes give sizable modification to cross sections. The DWBA calculation using the DI interaction at $E_\alpha = 386$ MeV reasonably reproduces the experimental results even for the 0_2^+ state in ^{12}C.

6.4 Determination of the transition strengths

Among the excited states observed in the present work listed in Table 4.1, there are the excited states whose electromagnetic transition strengths are not reported in the previous studies. As discussed in Sect. 6.1 that the DWBA calculation with the DI

interaction gives a better description for the inelastic alpha scattering than that with the DD interaction for the excited states whose transition strengths are known. Thus, we should determine the transition strengths for those states from the present data with the DI interaction assuming the linear proportionality between the (α, α') cross section and the relevant transition strength.

The DWBA calculations using the DI interaction were performed and fitted to the measured cross sections by changing the amplitudes of the transition densities (α_0 and δ_λ) in Eqs. (5.14) and (5.16). The fitted results are shown by the solid lines in Fig. 4.9, whereas the calculated cross section using the DD interactions with the same amplitudes with the DI interaction are shown by the dashed lines.

The obtained transition strengths are summarized in Table. 6.1. The errors for the strengths originate from the uncertainty of the fitting. The multipolarity λ in Table 6.1 is equal to the spin of the excited state because the spin of the ground state in the self-conjugate $A = 4n$ nuclei is zero.

Table 6.1: Measured transition strengths between the ground and excited states in ^{24}Mg, ^{28}Si, and ^{40}Ca.

Nucleus	E_α (MeV)	E_x (MeV)	J^π	$B(E\lambda; IS)$ (fm$^{2\lambda}$)[a]	EWSR fraction (%)
^{24}Mg	130	9.31	0_3^+	46 ± 31	2.3 ± 1.6
^{24}Mg	386	9.31	0_3^+	64 ± 48	3.2 ± 2.4
^{28}Si	130	6.69	0_3^+	27 ± 13	0.77 ± 0.36
^{28}Si	130	10.18	3_2^-	$(6.0 \pm 0.5) \times 10^3$	6.8 ± 0.5
^{28}Si	130	10.51	2_5^+	12 ± 3	0.60 ± 0.17
^{40}Ca	130	8.28	0_3^+	91 ± 28	1.8 ± 0.6
^{40}Ca	130	8.37	4_1^+	$(2.0 \pm 0.4) \times 10^5$	1.2 ± 0.2

[a] The unit is fm^4 for $\lambda = 0$.

The calculated cross sections fitted to the experiment reproduce the experimental data reasonably well over all measured angles except for the 0_3^+ state in ^{24}Mg at both $E_\alpha = 130$ and 386 MeV. The third diffraction maxima of the calculated cross sections for this state are about four times smaller than those of the measured cross sections, and this is one reason why the errors in the deduced $B(E\lambda; IS)$ are quite large. However, the calculated cross sections for the 0_3^+ state in ^{24}Mg reproduce the experiment at forward angles including 0°.

In contrast to the cases of $\lambda = 0$ and $\lambda \geq 2$ transitions, the situation for the $\lambda = 1$

transitions is not simple. Since the $E1$ transition between isoscalar states is forbidden to the first order, the observed $E1$ transitions between the isoscalar states are competitive processes between isovector transitions allowed by the isospin symmetry breaking and higher-order isoscalar transitions as squeezing oscillation. We can not directly compare the absolute values of the calculated cross sections with the experimental data. because these two types of $E1$ transitions have different transition densities and the known electromagnetic transition strengths $B(E1)$ can not be related to the collective coupling parameter of the transition density in Eq. (5.12).

Therefore, we determined the collective coupling parameter β_1 in Eq. (5.12) to fit the first diffraction maxima of the cross sections assuming that these $E1$ transitions are purely higher-order isoscalar transitions. As discussed in Sec. 6.1, the diffraction pattern of the cross sections are reproduced well by the DWBA calculations using both the DI and DD interactions, and the DI interactions gives systematically smaller cross sections than the DD interactions as in the other multipole transitions.

The deduced coupling parameter β_1 is compared with $\beta_1^{\rm EWSR}$ given by Eq. (5.15) which corresponds to 100% of the EWSR strengths in Table 6.2. The EWSR fractions for β_1 are also shown.

Table 6.2: Deduced collective coupling parameters β_1 and that for the transition with 100% of the EWSR strength ($\beta_1^{\rm EWSR}$). The experimental data and calculated cross sections are shown in Fig. 4.8.

Nucleus	E_α (MeV)	E_x (MeV)	J^π	β_1	EWSR fraction (%)	$\beta_1^{\rm EWSR}$
^{12}C	130	10.84	1_1^-	1.45×10^{-2}	1	1.45×10^{-1}
^{16}O	130	7.12	1_1^-	3.02×10^{-2}	6	1.27×10^{-1}
^{24}Mg	130	9.15	1_1^-	4.11×10^{-2}	0.3	7.51×10^{-1}
^{28}Si	130	8.90	1_1^-	6.47×10^{-3}	1	6.55×10^{-2}
^{28}Si	130	9.93	1_2^-	9.03×10^{-3}	2	6.20×10^{-2}
^{40}Ca	130	5.90	1_1^-	4.11×10^{-3}	7	1.56×10^{-2}

Chapter 7

Summary

Strength distributions in excitation-energy spectra of atomic nuclei provide insights into the nuclear structure because they directly reflect nuclear wave functions. Excitation strength is fundamentally the overlap between wave functions of ground and excited states, and energy is an eigenvalue of a nuclear Hamiltonian associated with the wave function. The excitation strength and energy are experimental observables, and can be directly compared with theoretical calculations of the nuclear structures. Therefore, the determination of the strength distribution is important to study the nuclear structure, for example, the cluster structures in nuclei.

The inelastic alpha scattering has selectivity to isoscalar natural-parity transitions where transferred spin and isospin are $\Delta S = 0$ and $\Delta T = 0$ since both spin and isospin of the alpha particle are zero. Therefore, the inelastic alpha scattering is useful to determine the strength distribution in excitation-energy region where several states overlap each other. In addition, the MDA works well to separate the strength distributions of the different transferred angular momenta ΔL, and it enables us to obtain the strength distribution of the isoscalar natural-parity excitations even from continuous excitation-energy spectra where many states with large widths overlap each other.

The MDA is established on the assumption that the cross sections of the inelastic alpha scattering are reasonably well described by the DWBA calculation and are approximately proportional to the relevant transition strength. However, a result contradictory to this linear proportional relation was reported in the monopole excitation to the Hoyle state from the ground state in ^{12}C. It was claimed in Ref. [58] that this problem was due to the reaction mechanism of the inelastic alpha scattering, and the inelastic alpha scattering

might strongly couple to the nuclear structure.

Therefore, it had been very urgent to confirm whether this puzzle of the inelastic alpha scattering really exists or not. If it exists, the puzzle should be solved, otherwise the strength distribution determined by the MDA of the inelastic alpha scattering might not be reliable. Nevertheless, the systematic measurement of the inelastic alpha scattering had not been performed nor examined to check the reliability of the theoretical calculation used in the MDA until now. In the present work, we systematically measured the cross sections of the inelastic alpha scattering at $E_\alpha = 130$ and 386 MeV exciting low-lying discrete states in ^{12}C, ^{16}O, ^{20}Ne, ^{24}Mg, ^{28}Si and ^{40}Ca for the first time. In addition, the comparison of the measured cross sections with the "parameter-free" DWBA calculation was carried out. All of the adjustable parameters in the DWBA calculation were determined by the electromagnetic transition strengths and the elastic alpha scattering, therefore there is no room for so-called "the puzzle of missing monopole strength" if the consistency between the measured cross sections and the present DWBA calculations is confirmed.

It was found that the DWBA calculation with the DI interaction at $E_\alpha = 386$ MeV was better than with the DD interaction and the calculation with the DI interaction at $E_\alpha = 386$ MeV was better than that at $E_\alpha = 130$ MeV, and thus the inadequate density dependence in the effective αN interaction caused the "puzzle of missing monopole strength" by overestimating the cross sections for the $\Delta L = 0$ transitions. This puzzle was not specific to the Hoyle state in ^{12}C but universally observed in all of the $\Delta L = 0$ transitions.

We also studied ambiguities of the DWBA calculation from the distorting potentials, phenomenological interaction, transition densities, and coupled-channel effects. The ambiguities originating from these factors in the present calculations were negligibly small in most cases of the inelastic scattering, although the CC effects sometimes gave sizable modification to cross sections.

It was also shown that there were still some uncertainties even for the DWBA calculations with the DI interaction to determine the strength distribution. Therefore, a new effective αN interaction with a more sophisticated formula is necessary. The present results should provide the unique and important information for theoretical studies to develop a new reliable αN interaction.

ACKNOWLEDGMENTS

I would like to express a great gratitude, first and foremost, to Prof. T. Kawabata, who is my supervisor during almost all periods of my Ph.D. course at Kyoto University. He introduced me the research field of clustering in nuclei, and the present research theme is motivated to study the clustering in nuclei. He has been giving me continuous support and encouragement for the experiment, the analysis, and the writing and also taking care of my condition during these several years. Therefore, I owe what I am to him.

Both Prof. K. Imai and Prof. T. Nagae have been supporting and instructing me from the start of my research career as a master course student. I spent a special and precious period under them when the new experimental facility J-PARC was just launched and the first physics program was about to get the experimental results.

Core members of the experiment RCNP-E402 at the same laboratory with me when the measurement was performed, Mr. T. Baba, Mr. T. Furuno, Mr. Y. Ishii, Prof. Y. Matsuda, Mr. M. Murata, and Ms. M. Tsumura, mainly supported the ^{20}Ne measurements. They helped me to prepare the experiment again and again without complaining, and the measurements would not be carried out without their continuous and intense cooperation. The other collaborators of E402 also helped me a lot during and also after the experiment. Especially, Prof. H. Matsubara explained and taught me how to use the gas target at RCNP, and supported me to start the research at RCNP. Mr. K. Inaba kindly provided me the data of the ^{12}C measurements. The cross sections given from him, and his support were very important in the present work. The early works by Mr. N. Yokota and Mr. T. Kadoya are the start point of the present work, and many cross-section data were taken under the experiment RCNP-E308 and E369 with them and analyzed by them. I would like to express my thankfulness and appreciation to them. The elastic scatterings at $E_\alpha = 130$ MeV at backward angles were measured under the graduation research program by undergraduate students at Kyoto University (KADAIKENKYU P4), and these data are important to determine the αN interaction precisely. I appreciate the members of P4, the teaching assistants, and also Prof.

Kawabata and Prof. Kanada-En'yo.

Prof. Minomo and Prof. Funaki provided the theoretical calculations which are necessary and important for the discussion in the present work. I asked Prof. Minomo to calculate the cross sections under many different conditions again and again, however, he supported me with tender care even though he must have been busy with his own research. In addition, I had the meetings about the inelastic alpha scattering and the puzzle of the missing monopole strength in these few years, and the discussions during the meetings were very valuable and indispensable for this work and the paper. I would like to thank Prof. Y. Funaki, Prof. M. Ito, Prof. M. Kimura, Prof. Y. Kanada-En'yo Prof. K. Minomo, and Prof. M. Takashina for giving me such a special opportunity.

All of the data for the present work are taken at RCNP. I would like to thank the RCNP cyclotron staffs for providing a high-quality beam for background-free measurements at forward angles including 0°. Many staffs supported the research and my life at RCNP. Particularly, Prof. N. Aoi and Prof. A. Tamii have been kindly supporting me and providing a good environment for the research. I would not be able to study continuously without their help.

Finally, I would like to express my great appreciations to my parents and brother Hiroshi, Sanae, and Akira. They understand my situation well and always support me with patience. I have been able to keep carrying out the present work for these year thanks to their help.

Appendix A

Data tables of cross sections

A.1 Elastic scattering

A.1.1 $E_\alpha = 130$ MeV

Table A.1: $^{12}C(\alpha,\alpha)$ elastic, $E_\alpha = 130$ MeV

$\theta_{c.m.}$ (deg)	$d\sigma/d\Omega$ (mb/sr)	error (mb/sr)
5.0	9.74×10^{3}	5.3×10^{2}
6.0	6.97×10^{3}	3.9×10^{2}
6.2	6.40×10^{3}	3.4×10^{2}
7.3	3.92×10^{3}	2.1×10^{2}
8.3	1.81×10^{3}	9.9×10^{1}
9.4	7.72×10^{2}	4.4×10^{1}
10.5	2.06×10^{2}	1.1×10^{1}
11.5	6.59×10^{1}	3.9
12.6	1.02×10^{2}	5.9
13.7	1.93×10^{2}	1.1×10^{1}
14.7	2.48×10^{2}	1.3×10^{1}
15.8	2.65×10^{2}	1.3×10^{1}
16.9	2.17×10^{2}	1.2×10^{1}
18.0	1.70×10^{2}	9.1
19.0	1.10×10^{2}	5.9
20.1	7.24×10^{1}	3.9
21.1	4.82×10^{1}	2.7
22.2	4.46×10^{1}	2.5
23.3	4.79×10^{1}	2.6

Table A.1: (Continued)

$\theta_{c.m.}$ (deg)	$d\sigma/d\Omega$ (mb/sr)	error (mb/sr)
24.3	5.53×10^{1}	3.0
25.4	5.73×10^{1}	3.1
26.5	5.87×10^{1}	3.2
27.5	5.29×10^{1}	3.1
28.6	4.75×10^{1}	2.8
29.6	3.78×10^{1}	2.2
30.7	3.20×10^{1}	1.9
31.7	2.60×10^{1}	1.5
32.8	2.26×10^{1}	1.3
33.8	1.93×10^{1}	1.1
34.9	1.79×10^{1}	1.1
35.9	1.62×10^{1}	9.5×10^{-1}
37.0	1.51×10^{1}	8.9×10^{-1}
38.0	1.24×10^{1}	7.2×10^{-1}
39.1	1.14×10^{1}	6.7×10^{-1}
40.1	9.43	5.5×10^{-1}
41.1	8.11	4.8×10^{-1}
41.9	7.00	5.1×10^{-1}
43.7	4.77	3.5×10^{-1}

Table A.2: $^{16}O(\alpha,\alpha)$ elastic, $E_\alpha = 130$ MeV

$\theta_{c.m.}$ (deg)	$d\sigma/d\Omega$ (mb/sr)	error (mb/sr)
4.7	1.53×10^{4}	8.4×10^{2}
5.7	1.00×10^{4}	5.6×10^{2}
5.8	9.82×10^{3}	5.2×10^{2}
6.8	5.35×10^{3}	2.9×10^{2}
7.8	1.91×10^{3}	1.0×10^{2}
8.8	6.23×10^{2}	3.5×10^{1}
9.8	9.41×10^{1}	5.5
10.8	8.55×10^{1}	5.0
11.8	2.34×10^{2}	1.4×10^{1}
12.8	3.54×10^{2}	2.0×10^{1}
13.8	3.68×10^{2}	1.9×10^{1}
14.8	3.14×10^{2}	1.7×10^{1}
15.8	1.95×10^{2}	1.1×10^{1}
16.8	1.14×10^{2}	6.6
17.8	5.38×10^{1}	3.1
18.8	3.72×10^{1}	2.2
19.8	4.31×10^{1}	2.5
20.8	6.27×10^{1}	3.6
21.8	7.37×10^{1}	4.2
22.8	8.04×10^{1}	4.5
23.8	6.97×10^{1}	3.8
24.8	6.25×10^{1}	3.4
25.8	4.61×10^{1}	2.7
26.8	4.09×10^{1}	2.4
27.8	3.47×10^{1}	2.0
28.8	3.39×10^{1}	2.0
29.8	3.26×10^{1}	1.9

Table A.2: (Continued)

$\theta_{c.m.}$ (deg)	$d\sigma/d\Omega$ (mb/sr)	error (mb/sr)
30.7	3.35×10^{1}	2.0
31.7	3.14×10^{1}	1.9
32.7	3.05×10^{1}	1.8
33.7	2.59×10^{1}	1.5
34.7	2.36×10^{1}	1.4
35.7	1.91×10^{1}	1.1
36.6	1.62×10^{1}	9.7×10^{-1}
37.6	1.30×10^{1}	7.8×10^{-1}
38.6	1.11×10^{1}	6.7×10^{-1}
39.3	9.05	6.8×10^{-1}
41.0	7.83	4.9×10^{-1}

Table A.3: ^{24}Mg(α,α) elastic, $E_\alpha = 130$ MeV

$\theta_{c.m.}$ (deg)	$d\sigma/d\Omega$ (mb/sr)	error (mb/sr)
5.4	2.17×10^{4}	1.2×10^{3}
6.3	1.06×10^{4}	5.8×10^{2}
7.3	1.79×10^{3}	9.5×10^{1}
8.2	3.04×10^{2}	1.8×10^{1}
9.1	6.50×10^{1}	3.9
10.1	3.46×10^{2}	1.9×10^{1}
11.0	5.97×10^{2}	3.5×10^{1}
11.9	6.50×10^{2}	3.8×10^{1}
12.9	4.82×10^{2}	2.7×10^{1}
13.8	2.99×10^{2}	1.8×10^{1}
14.8	1.19×10^{2}	6.6
15.7	4.29×10^{1}	2.5
16.6	3.07×10^{1}	1.8
17.6	5.49×10^{1}	3.1
18.5	7.82×10^{1}	4.6
19.4	8.67×10^{1}	5.0
20.3	7.49×10^{1}	4.3
21.3	5.68×10^{1}	3.4
22.2	3.51×10^{1}	2.0
23.1	2.49×10^{1}	1.5
24.1	1.95×10^{1}	1.2
25.0	2.12×10^{1}	1.3
25.9	2.34×10^{1}	1.4
26.9	2.55×10^{1}	1.5
27.8	2.36×10^{1}	1.4
28.7	2.13×10^{1}	1.3
29.6	1.68×10^{1}	1.0
30.6	1.38×10^{1}	8.5×10^{-1}
31.5	1.07×10^{1}	6.8×10^{-1}
32.4	9.56	6.1×10^{-1}
33.3	8.57	5.6×10^{-1}
34.2	8.29	5.4×10^{-1}
35.2	7.22	4.8×10^{-1}
36.1	6.65	4.5×10^{-1}

Table A.3: (Continued)

$\theta_{c.m.}$ (deg)	$d\sigma/d\Omega$ (mb/sr)	error (mb/sr)
36.3	6.26	4.4×10^{-1}
37.4	5.17	3.6×10^{-1}
38.7	4.36	3.1×10^{-1}
39.8	3.69	2.6×10^{-1}
42.1	2.51	1.8×10^{-1}
44.4	1.51	1.1×10^{-1}
46.4	1.13	7.9×10^{-2}
48.6	7.17×10^{-1}	5.0×10^{-2}
51.0	4.99×10^{-1}	3.5×10^{-2}
52.9	3.40×10^{-1}	2.4×10^{-2}
55.6	2.37×10^{-1}	1.7×10^{-2}
57.4	1.57×10^{-1}	1.1×10^{-2}
59.5	1.02×10^{-1}	7.1×10^{-3}
61.2	6.77×10^{-2}	4.7×10^{-3}
64.3	3.53×10^{-2}	2.5×10^{-3}
67.5	2.08×10^{-2}	1.5×10^{-3}
70.4	1.11×10^{-2}	7.8×10^{-4}

Table A.4: ^{28}Si(α,α) elastic, $E_\alpha = 130$ MeV

$\theta_{c.m.}$ (deg)	$d\sigma/d\Omega$ (mb/sr)	error (mb/sr)
8.0	2.96×10^{2}	1.7×10^{1}
9.0	2.07×10^{2}	1.2×10^{1}
9.9	6.99×10^{2}	3.8×10^{1}
10.8	9.78×10^{2}	5.5×10^{1}
11.7	9.55×10^{2}	5.4×10^{1}
12.6	6.04×10^{2}	3.2×10^{1}
13.5	3.19×10^{2}	1.7×10^{1}
14.4	1.09×10^{2}	6.0
15.4	4.06×10^{1}	2.4
16.3	5.82×10^{1}	3.4
17.2	1.07×10^{2}	6.0
18.1	1.23×10^{2}	6.9
19.0	1.21×10^{2}	6.8
19.9	8.94×10^{1}	5.1
20.8	5.85×10^{1}	3.4
21.8	3.32×10^{1}	2.0
22.7	2.43×10^{1}	1.5
23.6	2.63×10^{1}	1.6
24.5	3.31×10^{1}	1.9
25.4	3.60×10^{1}	2.1
26.3	3.66×10^{1}	2.2
27.2	3.13×10^{1}	1.8
28.1	2.60×10^{1}	1.5
29.0	1.97×10^{1}	1.2
29.9	1.69×10^{1}	1.0
30.8	1.48×10^{1}	9.0×10^{-1}
31.7	1.49×10^{1}	9.0×10^{-1}
32.6	1.41×10^{1}	8.4×10^{-1}
33.6	1.38×10^{1}	8.3×10^{-1}
34.5	1.30×10^{1}	8.0×10^{-1}
35.4	1.17×10^{1}	7.3×10^{-1}
34.5	1.30×10^{1}	7.9×10^{-1}
36.1	1.06×10^{1}	6.7×10^{-1}
37.7	8.84	5.6×10^{-1}
39.3	7.66	4.9×10^{-1}
40.9	5.65	3.5×10^{-1}
42.5	3.37	2.4×10^{-1}
44.1	2.77	2.1×10^{-1}
45.6	2.10	1.7×10^{-1}
47.2	1.44	1.3×10^{-1}
48.8	9.29×10^{-1}	9.2×10^{-2}

Table A.5: ^{40}Ca(α,α) elastic, $E_\alpha = 130$ MeV

$\theta_{c.m.}$ (deg)	$d\sigma/d\Omega$ (mb/sr)	error (mb/sr)
4.1	6.59×10^{4}	3.5×10^{3}
5.0	3.28×10^{4}	1.8×10^{3}
5.1	2.83×10^{4}	1.5×10^{3}
6.0	1.08×10^{4}	5.9×10^{2}
6.8	2.05×10^{3}	1.1×10^{2}
7.7	5.86×10^{2}	3.3×10^{1}
8.6	1.00×10^{3}	5.6×10^{1}
9.5	1.54×10^{3}	8.4×10^{1}
10.4	1.39×10^{3}	7.9×10^{1}
11.3	9.16×10^{2}	5.3×10^{1}
12.1	3.38×10^{2}	1.8×10^{1}
13.0	7.17×10^{1}	4.2
13.9	3.17×10^{1}	1.9
14.8	1.23×10^{2}	6.8
15.7	2.02×10^{2}	1.2×10^{1}
16.5	2.19×10^{2}	1.3×10^{1}
17.4	1.60×10^{2}	8.9
18.3	9.42×10^{1}	5.4
19.2	3.62×10^{1}	2.1
20.1	1.96×10^{1}	1.2
20.9	2.52×10^{1}	1.5
21.8	3.72×10^{1}	2.2
22.7	4.10×10^{1}	2.4
23.6	3.63×10^{1}	2.2
24.4	2.37×10^{1}	1.4
25.3	1.47×10^{1}	9.3×10^{-1}
26.2	9.24	6.2×10^{-1}
27.1	9.22	6.2×10^{-1}
27.9	1.14×10^{1}	7.4×10^{-1}
28.8	1.36×10^{1}	8.7×10^{-1}
29.7	1.35×10^{1}	8.6×10^{-1}
30.6	1.25×10^{1}	8.1×10^{-1}
31.4	9.99	6.6×10^{-1}
32.3	8.69	5.9×10^{-1}
33.2	7.53	5.2×10^{-1}
34.1	7.39	5.1×10^{-1}
34.8	7.00	6.6×10^{-1}
36.3	7.37	4.7×10^{-1}
37.9	6.29	4.2×10^{-1}
39.4	3.87	4.3×10^{-1}
41.0	3.45	3.2×10^{-1}
42.5	3.17	4.0×10^{-1}
44.0	2.76	2.7×10^{-1}
45.6	1.72	1.4×10^{-1}
47.1	1.26	1.1×10^{-1}
48.6	8.94×10^{-1}	6.5×10^{-2}
50.2	6.69×10^{-1}	6.0×10^{-2}
51.7	4.27×10^{-1}	5.4×10^{-2}
53.2	3.76×10^{-1}	5.4×10^{-2}
54.7	3.02×10^{-1}	4.8×10^{-2}
56.2	1.97×10^{-1}	4.3×10^{-2}
57.8	1.65×10^{-1}	3.9×10^{-2}
59.3	1.05×10^{-1}	1.4×10^{-2}

Table A.5: (Continued)

A.1.2 $E_\alpha = 386$ MeV

Table A.6: ^{12}C(α,α) elastic, $E_\alpha = 386$ MeV

$\theta_{c.m.}$ (deg)	$d\sigma/d\Omega$ (mb/sr)	error (mb/sr)
2.7	2.03×10^{4}	1.0×10^{3}
3.3	1.73×10^{4}	8.7×10^{2}
3.8	1.35×10^{4}	6.8×10^{2}
4.3	1.02×10^{4}	5.1×10^{2}
4.3	1.15×10^{4}	5.8×10^{2}
4.8	7.52×10^{3}	3.8×10^{2}
5.4	5.06×10^{3}	2.6×10^{2}
5.9	3.05×10^{3}	1.5×10^{2}
6.2	2.13×10^{3}	1.1×10^{2}
6.7	1.19×10^{3}	6.0×10^{1}
7.3	6.15×10^{2}	3.1×10^{1}
7.8	3.69×10^{2}	1.9×10^{1}
8.1	3.04×10^{2}	9.2
8.6	3.02×10^{2}	9.1
9.2	3.20×10^{2}	9.6
9.7	3.26×10^{2}	9.8
9.0	3.09×10^{2}	9.4
9.6	3.25×10^{2}	9.8
10.1	3.19×10^{2}	9.6
10.6	2.89×10^{2}	8.8
11.2	2.25×10^{2}	6.8
11.7	1.83×10^{2}	5.5
12.3	1.38×10^{2}	4.2
12.8	9.83×10^{1}	3.0
13.3	5.74×10^{1}	1.7
13.9	4.04×10^{1}	1.2
14.4	2.83×10^{1}	8.7×10^{-1}
15.0	2.06×10^{1}	6.4×10^{-1}
15.5	1.52×10^{1}	4.7×10^{-1}
16.0	1.37×10^{1}	4.2×10^{-1}
16.6	1.25×10^{1}	3.9×10^{-1}
17.1	1.13×10^{1}	3.5×10^{-1}
17.7	9.08	2.8×10^{-1}
18.2	7.83	2.4×10^{-1}

Table A.6: (Continued)

$\theta_{c.m.}$ (deg)	$d\sigma/d\Omega$ (mb/sr)	error (mb/sr)
18.7	6.45	2.0×10^{-1}
19.3	4.98	1.5×10^{-1}
19.8	3.00	9.1×10^{-2}
20.4	2.26	6.8×10^{-2}
20.9	1.64	5.0×10^{-2}
21.4	1.18	3.6×10^{-2}
22.0	7.36×10^{-1}	2.3×10^{-2}
22.5	5.80×10^{-1}	1.8×10^{-2}
23.0	4.63×10^{-1}	1.4×10^{-2}
23.6	3.85×10^{-1}	1.2×10^{-2}
24.1	2.99×10^{-1}	9.2×10^{-3}
24.7	2.59×10^{-1}	8.0×10^{-3}
25.2	2.16×10^{-1}	6.7×10^{-3}
25.7	1.79×10^{-1}	5.6×10^{-3}
26.3	1.26×10^{-1}	3.9×10^{-3}
26.8	1.04×10^{-1}	3.2×10^{-3}
27.3	7.93×10^{-2}	2.5×10^{-3}
27.9	6.10×10^{-2}	1.9×10^{-3}
28.4	3.96×10^{-2}	1.3×10^{-3}
28.9	3.20×10^{-2}	1.0×10^{-3}
29.5	2.50×10^{-2}	8.2×10^{-4}
30.0	1.99×10^{-2}	6.7×10^{-4}
30.5	1.47×10^{-2}	5.2×10^{-4}
31.1	1.25×10^{-2}	4.6×10^{-4}
31.6	1.01×10^{-2}	3.8×10^{-4}
32.1	8.38×10^{-3}	3.3×10^{-4}
32.7	5.81×10^{-3}	2.2×10^{-4}
33.2	4.82×10^{-3}	1.9×10^{-4}
33.7	3.99×10^{-3}	1.7×10^{-4}
34.3	3.01×10^{-3}	1.3×10^{-4}

Table A.7: ^{20}Ne(α,α) elastic, $E_\alpha = 386$ MeV

$\theta_{c.m.}$ (deg)	$d\sigma/d\Omega$ (mb/sr)	error (mb/sr)
5.1	9.44×10^{2}	5.6×10^{1}
5.6	3.57×10^{2}	2.7×10^{1}
7.3	5.19×10^{2}	2.5×10^{1}
7.8	5.35×10^{2}	2.6×10^{1}
8.3	4.77×10^{2}	2.3×10^{1}
8.8	3.84×10^{2}	1.9×10^{1}
9.0	3.40×10^{2}	1.6×10^{1}
9.5	2.39×10^{2}	1.1×10^{1}
10.0	1.56×10^{2}	7.7
10.5	9.72×10^{1}	5.0
10.7	6.75×10^{1}	3.4
11.2	4.73×10^{1}	2.4
11.7	3.98×10^{1}	2.1
12.2	3.47×10^{1}	1.8
12.4	3.50×10^{1}	1.7
12.9	3.24×10^{1}	1.6
13.4	2.84×10^{1}	1.4
13.9	2.36×10^{1}	1.2
14.1	2.10×10^{1}	1.1
14.6	1.64×10^{1}	8.5×10^{-1}
15.1	1.18×10^{1}	6.3×10^{-1}
15.6	8.18	4.6×10^{-1}
15.8	6.55	3.8×10^{-1}
16.3	4.56	2.8×10^{-1}
16.8	3.30	2.1×10^{-1}
17.3	2.46	1.7×10^{-1}
17.5	2.06	1.2×10^{-1}
18.0	1.66	1.0×10^{-1}
18.5	1.43	9.0×10^{-2}
19.0	1.24	8.0×10^{-2}
19.2	1.09	6.5×10^{-2}
19.7	8.48×10^{-1}	5.2×10^{-2}
20.2	7.01×10^{-1}	4.5×10^{-2}
20.7	5.18×10^{-1}	3.5×10^{-2}
21.0	4.47×10^{-1}	3.0×10^{-2}
21.4	3.34×10^{-1}	2.4×10^{-2}
21.9	2.43×10^{-1}	1.9×10^{-2}
22.3	1.71×10^{-1}	1.4×10^{-2}

Table A.7: (Continued)

$\theta_{c.m.}$ (deg)	$d\sigma/d\Omega$ (mb/sr)	error (mb/sr)
22.6	1.50×10^{-1}	1.3×10^{-2}
23.1	1.05×10^{-1}	9.8×10^{-3}
23.6	8.39×10^{-2}	8.3×10^{-3}
24.0	7.11×10^{-2}	7.4×10^{-3}
24.3	6.90×10^{-2}	7.3×10^{-3}
24.8	4.73×10^{-2}	5.6×10^{-3}
25.2	4.06×10^{-2}	5.1×10^{-3}
25.7	2.86×10^{-2}	4.0×10^{-3}
26.0	3.31×10^{-2}	3.4×10^{-3}
26.4	2.13×10^{-2}	2.5×10^{-3}
26.9	1.87×10^{-2}	2.3×10^{-3}
27.4	1.38×10^{-2}	1.9×10^{-3}

Table A.8: ^{24}Mg(α,α) elastic, $E_\alpha = 386$ MeV

$\theta_{c.m.}$ (deg)	$d\sigma/d\Omega$ (mb/sr)	error (mb/sr)
5.3	8.78×10^{2}	5.3×10^{1}
5.7	5.00×10^{2}	3.9×10^{1}
6.2	6.96×10^{2}	4.6×10^{1}
6.7	9.11×10^{2}	5.4×10^{1}
7.0	1.09×10^{3}	4.5×10^{1}
7.5	1.10×10^{3}	4.4×10^{1}
8.0	9.65×10^{2}	4.1×10^{1}
8.4	7.40×10^{2}	3.7×10^{1}
9.4	3.28×10^{2}	1.4×10^{1}
9.8	1.91×10^{2}	1.1×10^{1}
10.3	1.22×10^{2}	8.4
10.8	8.48×10^{1}	7.2
11.7	7.60×10^{1}	8.5
12.2	7.69×10^{1}	8.4
12.7	7.10×10^{1}	8.1
13.1	5.74×10^{1}	7.4
14.1	3.11×10^{1}	1.4
14.5	2.18×10^{1}	1.1
15.0	1.44×10^{1}	9.3×10^{-1}
15.5	9.56	7.6×10^{-1}
16.4	5.58	6.6×10^{-1}
16.9	4.80	6.1×10^{-1}
17.4	4.05	5.7×10^{-1}
17.8	3.56	5.2×10^{-1}
18.8	2.20	2.8×10^{-1}
19.2	1.67	2.4×10^{-1}
19.7	1.14	2.0×10^{-1}
20.2	8.5×10^{-1}	1.7×10^{-1}
21.1	4.49×10^{-1}	9.8×10^{-2}
21.6	3.67×10^{-1}	8.4×10^{-2}
22.1	2.37×10^{-1}	6.9×10^{-2}
22.5	1.96×10^{-1}	6.3×10^{-2}
23.5	1.28×10^{-1}	3.1×10^{-2}
23.9	1.04×10^{-1}	2.8×10^{-2}
24.4	7.85×10^{-2}	2.4×10^{-2}
24.9	6.18×10^{-2}	2.2×10^{-2}
25.8	2.84×10^{-2}	1.3×10^{-2}
26.3	2.52×10^{-2}	1.2×10^{-2}
26.7	1.68×10^{-2}	8.9×10^{-3}
27.2	1.17×10^{-2}	7.7×10^{-3}
28.8	2.7×10^{-3}	1.3×10^{-3}

A.2 Inelastic scattering

A.2.1 $E_\alpha = 130$ MeV

Table A.9: ^{12}C(α, α') inelastic, $E_x = 4.44$ MeV (2_1^+), $E_\alpha = 130$ MeV

$\theta_{c.m.}$ (deg)	$d\sigma/d\Omega$ (mb/sr)	error (mb/sr)
0.5	1.86×10^{1}	9.7×10^{-1}
2.8	2.33×10^{1}	1.4
3.9	1.91×10^{1}	1.1
5.0	2.08×10^{1}	1.2
6.1	3.20×10^{1}	1.8
6.2	3.39×10^{1}	1.9
7.3	4.94×10^{1}	2.9
8.4	6.20×10^{1}	3.3
9.4	7.32×10^{1}	3.8
10.5	6.61×10^{1}	3.5
11.6	6.14×10^{1}	3.2
12.7	4.49×10^{1}	2.4
13.8	3.37×10^{1}	1.8
14.8	2.18×10^{1}	1.2
15.9	1.73×10^{1}	9.4×10^{-1}
17.0	1.47×10^{1}	8.0×10^{-1}
18.1	1.73×10^{1}	9.3×10^{-1}

Table A.10: ^{12}C(α, α') inelastic, $E_x = 7.65$ MeV (0_2^+), $E_\alpha = 130$ MeV

$\theta_{c.m.}$ (deg)	$d\sigma/d\Omega$ (mb/sr)	error (mb/sr)
0.5	2.76×10^{1}	1.4
2.9	1.89×10^{1}	1.1
3.9	1.01×10^{1}	$6.3\text{n}\times10^{-1}$
5.0	3.69	2.4×10^{-1}
6.1	1.33	1.0×10^{-1}
6.2	1.19	8.8×10^{-2}
7.3	2.16	1.5×10^{-1}
8.4	4.20	2.5×10^{-1}
9.5	5.97	4.1×10^{-1}
10.6	6.30	3.7×10^{-1}
11.7	5.78	3.4×10^{-1}
12.7	3.84	2.3×10^{-1}
13.8	2.35	1.5×10^{-1}
14.9	1.35	8.9×10^{-2}
16.0	1.25	8.3×10^{-2}
17.1	1.45	9.1×10^{-2}
18.1	1.89	1.2×10^{-1}

Table A.11: ^{12}C(α, α') inelastic, $E_x = 9.64$ MeV (3_1^-), $E_\alpha = 130$ MeV

$\theta_{c.m.}$ (deg)	$d\sigma/d\Omega$ (mb/sr)	error (mb/sr)
0.5	1.88	1.5×10^{-1}
2.9	2.71	2.8×10^{-1}
3.9	3.06	3.1×10^{-1}
5.0	3.64	3.1×10^{-1}
6.1	4.40	3.5×10^{-1}
6.3	4.47	3.4×10^{-1}
7.3	5.32	4.0×10^{-1}
8.4	7.19	4.8×10^{-1}
9.5	9.49	6.1×10^{-1}
10.6	1.06×10^{1}	6.8×10^{-1}
11.7	1.13×10^{1}	7.1×10^{-1}
12.8	1.01×10^{1}	6.5×10^{-1}
13.9	9.20	6.0×10^{-1}
14.9	6.73	4.4×10^{-1}
16.0	4.98	3.4×10^{-1}
17.1	3.18	2.2×10^{-1}
18.2	2.76	2.0×10^{-1}

Table A.12: ^{12}C(α, α') inelastic, $E_x = 10.84$ MeV (1_1^-), $E_\alpha = 130$ MeV

$\theta_{c.m.}$ (deg)	$d\sigma/d\Omega$ (mb/sr)	error (mb/sr)
2.9	9.81×10^{-1}	1.2×10^{-1}
4.0	8.72×10^{-1}	1.1×10^{-1}
6.3	4.94×10^{-1}	5.8×10^{-2}
7.4	2.54×10^{-1}	4.1×10^{-2}
8.4	1.13×10^{-1}	2.5×10^{-2}
9.5	1.61×10^{-1}	2.9×10^{-2}
10.6	3.44×10^{-1}	4.7×10^{-2}
11.7	5.32×10^{-1}	5.5×10^{-2}
12.8	6.23×10^{-1}	6.2×10^{-2}
13.9	6.51×10^{-1}	6.4×10^{-2}
15.0	5.72×10^{-1}	5.6×10^{-2}
16.1	3.64×10^{-1}	4.3×10^{-2}
17.1	2.02×10^{-1}	2.8×10^{-2}
18.2	1.12×10^{-1}	2.1×10^{-2}

Table A.13: $^{16}O(\alpha,\alpha')$ inelastic, $E_x = 6.05$ MeV (0_2^+), $E_\alpha = 130$ MeV

$\theta_{c.m.}$ (deg)	$d\sigma/d\Omega$ (mb/sr)	error (mb/sr)
0.5	3.33	6.6×10^{-1}
2.7	2.38	9.9×10^{-1}

Table A.14: $^{16}O(\alpha,\alpha')$ inelastic, $E_x = 6.13$ MeV (3_1^-), $E_\alpha = 130$ MeV

$\theta_{c.m.}$ (deg)	$d\sigma/d\Omega$ (mb/sr)	error (mb/sr)
0.5	6.8	2.5
2.7	1.13×10^{1}	7.9×10^{-1}
3.7	1.40×10^{1}	9.5×10^{-1}
4.7	1.52×10^{1}	9.2×10^{-1}
5.7	1.77×10^{1}	1.1
5.8	1.85×10^{1}	1.0
6.8	2.26×10^{1}	1.3
7.8	2.57×10^{1}	1.5
8.9	3.33×10^{1}	1.8
9.9	3.56×10^{1}	1.9
10.9	3.89×10^{1}	2.1
11.9	3.47×10^{1}	1.9
12.9	3.08×10^{1}	1.7
13.9	2.18×10^{1}	1.2
14.9	1.55×10^{1}	8.6×10^{-1}
15.9	9.39	5.25×10^{-1}
16.9	7.47	4.23×10^{-1}

Table A.15: $^{16}O(\alpha,\alpha')$ inelastic, $E_x = 6.92$ MeV (2_1^+), $E_\alpha = 130$ MeV

$\theta_{c.m.}$ (deg)	$d\sigma/d\Omega$ (mb/sr)	error (mb/sr)
0.5	1.10×10^{1}	6.4×10^{-1}
2.7	1.30×10^{1}	8.9×10^{-1}
3.7	1.27×10^{1}	8.7×10^{-1}
4.7	1.54×10^{1}	9.3×10^{-1}
5.7	2.21×10^{1}	1.3
5.8	2.25×10^{1}	1.3
6.8	2.91×10^{1}	1.6
7.8	3.08×10^{1}	1.7
8.9	3.00×10^{1}	1.6
9.9	2.06×10^{1}	1.1
10.9	1.39×10^{1}	7.7×10^{-1}
11.9	6.99	4.0×10^{-1}
12.9	4.20	2.5×10^{-1}
13.9	3.58	2.6×10^{-1}
14.9	6.02	4.1×10^{-1}
15.9	7.76	4.9×10^{-1}
16.9	9.53	5.9×10^{-1}

Table A.16: $^{16}O(\alpha, \alpha')$ inelastic, $E_x = 7.12$ MeV (1_1^-), $E_\alpha = 130$ MeV

$\theta_{c.m.}$ (deg)	$d\sigma/d\Omega$ (mb/sr)	error (mb/sr)
0.5	2.10	1.4×10^{-1}
2.7	9.15	8.6×10^{-1}
3.7	1.17×10^{1}	1.0
4.7	1.07×10^{1}	8.0×10^{-1}
5.7	8.31	6.5×10^{-1}
5.8	8.16	5.6×10^{-1}
6.8	4.63	3.5×10^{-1}
7.9	1.45	1.3×10^{-1}
8.9	4.19×10^{-1}	6.9×10^{-2}
9.9	1.21	1.1×10^{-1}
10.9	2.48	1.9×10^{-1}
11.9	3.62	2.6×10^{-1}
12.9	4.05	2.9×10^{-1}
13.9	3.62	2.6×10^{-1}
14.9	2.87	2.2×10^{-1}
15.9	1.83	1.4×10^{-1}
16.9	1.25	1.1×10^{-1}

Table A.17: $^{16}O(\alpha, \alpha')$ inelastic, $E_x = 9.84$ MeV (2_2^+), $E_\alpha = 130$ MeV

$\theta_{c.m.}$ (deg)	$d\sigma/d\Omega$ (mb/sr)	error (mb/sr)
0.5	6.70×10^{-1}	8.9×10^{-2}
2.7	5.7×10^{-1}	1.8×10^{-1}
3.7	3.66×10^{-1}	6.9×10^{-2}
4.7	1.83×10^{-1}	6.5×10^{-2}
5.7	1.96×10^{-1}	4.7×10^{-2}
5.8	1.43×10^{-1}	2.4×10^{-2}
6.9	3.14×10^{-1}	6.1×10^{-2}
7.9	4.4×10^{-1}	1.3×10^{-1}
8.9	5.46×10^{-1}	5.2×10^{-2}
9.9	8.39×10^{-1}	8.7×10^{-2}
10.9	6.74×10^{-1}	6.4×10^{-2}
11.9	7.25×10^{-1}	7.9×10^{-2}
12.9	5.76×10^{-1}	8.6×10^{-2}
14.0	4.36×10^{-1}	4.7×10^{-2}
15.0	3.70×10^{-1}	4.2×10^{-2}
16.0	3.34×10^{-1}	3.8×10^{-2}
17.0	3.66×10^{-1}	4.1×10^{-2}

Table A.18: ^{16}O(α, α') inelastic, $E_x = 10.36$ MeV (4_1^+), $E_\alpha = 130$ MeV

$\theta_{c.m.}$ (deg)	$d\sigma/d\Omega$ (mb/sr)	error (mb/sr)
0.5	9.33×10^{-1}	5.8×10^{-2}
2.7	4.14×10^{-1}	7.0×10^{-2}
3.7	1.91×10^{-1}	4.0×10^{-2}
4.7	1.09×10^{-1}	2.3×10^{-2}
5.7	1.50×10^{-1}	2.8×10^{-2}
5.8	1.82×10^{-1}	2.9×10^{-2}
6.9	2.64×10^{-1}	3.8×10^{-2}
7.9	3.39×10^{-1}	4.0×10^{-2}
8.9	4.67×10^{-1}	5.1×10^{-2}
9.9	6.02×10^{-1}	7.9×10^{-2}
10.9	6.56×10^{-1}	6.9×10^{-2}
11.9	6.24×10^{-1}	6.0×10^{-2}
12.9	5.57×10^{-1}	5.5×10^{-2}
14.0	4.19×10^{-1}	4.7×10^{-2}
15.0	3.28×10^{-1}	4.1×10^{-2}
16.0	2.60×10^{-1}	3.4×10^{-2}
17.0	3.29×10^{-1}	3.9×10^{-2}

Table A.19: ^{16}O(α, α') inelastic, $E_x = 11.52$ MeV (2_3^+), $E_\alpha = 130$ MeV

$\theta_{c.m.}$ (deg)	$d\sigma/d\Omega$ (mb/sr)	error (mb/sr)
0.5	8.4	1.7
2.7	7.22	5.6×10^{-1}
3.7	7.21	5.6×10^{-1}
4.7	8.50	5.8×10^{-1}
5.7	1.06×10^{1}	7.1×10^{-1}
5.9	1.09×10^{1}	7.1×10^{-1}
6.9	1.30×10^{1}	8.3×10^{-1}
7.9	1.23×10^{1}	7.6×10^{-1}
8.9	1.23×10^{1}	7.6×10^{-1}
9.9	9.40	5.9×10^{-1}
10.9	6.58	4.4×10^{-1}
12.0	3.43	2.4×10^{-1}
13.0	2.29	1.7×10^{-1}
14.0	2.12	1.7×10^{-1}
15.0	2.78	2.1×10^{-1}
16.0	3.28	2.4×10^{-1}
17.0	4.16	2.9×10^{-1}

Table A.20: $^{16}O(\alpha,\alpha')$ inelastic, $E_x = 12.05$ MeV (0_3^+), $E_\alpha = 130$ MeV

$\theta_{c.m.}$ (deg)	$d\sigma/d\Omega$ (mb/sr)	error (mb/sr)
0.5	8.9	1.4
2.7	4.75	3.9×10^{-1}
3.7	2.42	2.4×10^{-1}
4.7	7.35×10^{-1}	8.9×10^{-2}
5.7	2.06×10^{-1}	3.9×10^{-2}
5.9	1.92×10^{-1}	3.8×10^{-2}
6.9	5.79×10^{-1}	7.2×10^{-2}
7.9	1.18	1.1×10^{-1}
8.9	1.49	1.3×10^{-1}
9.9	1.54	1.3×10^{-1}
10.9	1.41	1.3×10^{-1}
12.0	1.04	9.2×10^{-2}
13.0	6.29×10^{-1}	6.5×10^{-2}
14.0	1.51×10^{-1}	2.9×10^{-2}
15.0	3.13×10^{-1}	4.2×10^{-2}
16.0	7.80×10^{-1}	7.6×10^{-2}
17.0	8.84×10^{-1}	8.4×10^{-2}

Table A.21: $^{24}Mg(\alpha,\alpha')$ inelastic, $E_x = 1.37$ MeV (2_1^+), $E_\alpha = 130$ MeV

$\theta_{c.m.}$ (deg)	$d\sigma/d\Omega$ (mb/sr)	error (mb/sr)
0.5	1.20×10^{2}	6.4
2.5	8.80×10^{1}	4.8
3.4	6.71×10^{1}	4.1
4.3	9.20×10^{1}	4.9
5.3	1.43×10^{2}	7.6
5.4	1.49×10^{2}	7.9
6.3	1.97×10^{2}	1.0×10^{1}
7.3	1.93×10^{2}	1.0×10^{1}
8.2	1.74×10^{2}	9.0
9.1	1.08×10^{2}	5.6
10.1	5.81×10^{1}	3.1
11.0	1.90×10^{1}	1.1
12.0	1.19×10^{1}	6.7
12.9	2.46×10^{1}	1.3
13.8	4.46×10^{1}	2.4
14.8	5.48×10^{1}	2.9
15.7	5.70×10^{1}	3.0

Table A.22: ^{24}Mg(α,α') inelastic, $E_x = 4.12$ MeV (4_1^+), $E_\alpha = 130$ MeV

$\theta_{c.m.}$ (deg)	$d\sigma/d\Omega$ (mb/sr)	error (mb/sr)
7.3	5.0×10^{-1}	2.1×10^{-1}
8.2	7.00×10^{-1}	7.9×10^{-2}
9.2	8.2×10^{-1}	2.5×10^{-1}
10.1	1.12	2.7×10^{-1}
11.0	1.21	1.2×10^{-1}
12.0	1.32	9.1×10^{-2}
12.9	1.43	1.3×10^{-1}
13.9	1.29	1.2×10^{-1}
14.8	1.20	1.2×10^{-1}
15.7	1.13	1.2×10^{-1}

Table A.23: ^{24}Mg(α,α') inelastic, $E_x = 4.24$ MeV (2_2^+), $E_\alpha = 130$ MeV

$\theta_{c.m.}$ (deg)	$d\sigma/d\Omega$ (mb/sr)	error (mb/sr)
0.5	1.27×10^{1}	7.6×10^{-1}
2.5	1.76×10^{1}	1.1
3.4	1.18×10^{1}	7.3×10^{-1}
4.4	9.69	5.93×10^{-1}
5.3	1.14×10^{1}	6.9×10^{-1}
5.4	1.16×10^{1}	8.3×10^{-1}
6.3	1.49×10^{1}	1.1
7.3	1.50×10^{1}	8.8×10^{-1}
8.2	1.50×10^{1}	8.7×10^{-1}
9.2	1.05×10^{1}	6.3×10^{-1}
10.1	6.57	4.2×10^{-1}
11.0	2.71	1.9×10^{-1}
12.0	1.58	1.2×10^{-1}
12.9	1.87	1.4×10^{-1}
13.9	3.90	2.7×10^{-1}
14.8	5.31	3.5×10^{-1}
15.7	6.59	4.4×10^{-1}

Table A.24: ^{24}Mg(α,α') inelastic, $E_x = 6.01$ MeV (4_2^+), $E_\alpha = 130$ MeV

$\theta_{c.m.}$ (deg)	$d\sigma/d\Omega$ (mb/sr)	error (mb/sr)
0.5	5.99×10^{-1}	5.8×10^{-2}
2.5	7.65×10^{-1}	7.4×10^{-2}
3.4	1.04	9.3×10^{-2}
4.4	1.18	9.6×10^{-2}
5.3	1.64	1.3×10^{-1}
5.4	1.62	1.3×10^{-1}
6.4	2.16	1.6×10^{-1}
7.3	2.98	2.6×10^{-1}
8.2	4.30	2.6×10^{-1}
9.2	5.48	3.3×10^{-1}
10.1	7.12	4.2×10^{-1}
11.1	7.50	4.4×10^{-1}
12.0	7.69	4.5×10^{-1}
12.9	6.11	3.6×10^{-1}
13.9	4.56	2.8×10^{-1}
14.8	2.60	1.7×10^{-1}
15.7	1.60	1.1×10^{-1}

Table A.25: ^{24}Mg(α, α') inelastic, $E_x = 6.43$ MeV (0_2^+), $E_\alpha = 130$ MeV

$\theta_{c.m.}$ (deg)	$d\sigma/d\Omega$ (mb/sr)	error (mb/sr)
0.5	2.87×10^{1}	1.6
2.5	1.63×10^{1}	9.8×10^{-1}
3.4	6.57	4.3×10^{-1}
4.4	1.28	1.0×10^{-1}
5.3	5.46×10^{-1}	5.3×10^{-2}
5.4	7.38×10^{-1}	6.7×10^{-2}
6.4	2.81	2.0×10^{-1}
7.3	4.44	3.4×10^{-1}
8.2	4.92	3.5×10^{-1}
9.2	3.54	2.7×10^{-1}
10.1	2.53	1.6×10^{-1}
11.1	1.31	9.1×10^{-2}
12.0	1.31	9.1×10^{-2}
12.9	1.43	1.3×10^{-1}
13.9	2.45	1.6×10^{-1}
14.8	2.59	1.7×10^{-1}
15.8	2.39	1.6×10^{-1}

Table A.26: ^{24}Mg(α, α') inelastic, $E_x = 7.35$ MeV (2_3^+), $E_\alpha = 130$ MeV

$\theta_{c.m.}$ (deg)	$d\sigma/d\Omega$ (mb/sr)	error (mb/sr)
0.5	1.72	1.3×10^{-1}
2.5	2.45	1.8×10^{-1}
3.4	2.79	2.1×10^{-1}
4.4	3.96	2.7×10^{-1}
5.3	5.76	3.7×10^{-1}
5.4	5.85	3.8×10^{-1}
6.4	6.91	4.4×10^{-1}
7.3	5.52	3.9×10^{-1}
8.2	4.11	3.2×10^{-1}
9.2	1.96	1.3×10^{-1}
10.1	9.20×10^{-1}	6.7×10^{-2}
11.1	8.25×10^{-1}	6.1×10^{-2}
12.0	1.66	1.1×10^{-1}
12.9	2.28	1.5×10^{-1}
13.9	2.74	1.7×10^{-1}
14.8	2.18	1.4×10^{-1}
15.8	1.69	1.2×10^{-1}

Table A.27: ^{24}Mg(α,α') inelastic, $E_x = 7.62$ MeV (3_1^-), $E_\alpha = 130$ MeV

$\theta_{c.m.}$ (deg)	$d\sigma/d\Omega$ (mb/sr)	error (mb/sr)
0.5	3.33	2.3×10^{-1}
2.5	7.23	4.7×10^{-1}
3.4	8.32	5.3×10^{-1}
4.4	8.54	5.3×10^{-1}
5.3	8.85	5.5×10^{-1}
5.4	8.60	5.3×10^{-1}
6.4	9.06	5.6×10^{-1}
7.3	9.55	6.2×10^{-1}
8.2	1.16×10^{1}	7.5×10^{-1}
9.2	1.17×10^{1}	6.6×10^{-1}
10.1	1.12×10^{1}	6.4×10^{-1}
11.1	9.92	5.7×10^{-1}
12.0	7.83	4.5×10^{-1}
12.9	4.82	2.9×10^{-1}
13.9	3.32	2.1×10^{-1}
14.8	2.39	1.6×10^{-1}
15.8	2.69	1.7×10^{-1}

Table A.28: ^{24}Mg(α,α') inelastic, $E_x = 8.36$ MeV (3_2^-), $E_\alpha = 130$ MeV

$\theta_{c.m.}$ (deg)	$d\sigma/d\Omega$ (mb/sr)	error (mb/sr)
0.5	3.95	9.3×10^{-1}
2.5	4.60	5.8×10^{-1}
3.4	6.27	7.5×10^{-1}
4.4	6.67	7.5×10^{-1}
5.3	9.3	1.5
5.4	9.0	1.0
6.4	1.23×10^{1}	1.5
7.3	1.49×10^{1}	9.4×10^{-1}
8.3	1.85×10^{1}	1.0
9.2	1.81×10^{1}	9.6×10^{-1}
10.1	1.59×10^{1}	1.8
11.1	1.09×10^{1}	1.3
12.0	6.97	9.4×10^{-1}
13.0	3.24	4.7×10^{-1}
13.9	2.16	1.8×10^{-1}
14.8	2.53	2.9×10^{-1}
15.8	3.66	3.7×10^{-1}

Table A.29: ^{24}Mg(α,α') inelastic, $E_x = 9.00$ MeV (2_5^+), $E_\alpha = 130$ MeV

$\theta_{c.m.}$ (deg)	$d\sigma/d\Omega$ (mb/sr)	error (mb/sr)
2.5	6.78×10^{-1}	6.7×10^{-2}
3.4	6.68×10^{-1}	6.6×10^{-2}
4.4	8.64×10^{-1}	7.5×10^{-2}
5.3	1.18	9.6×10^{-2}
5.4	1.07	9.0×10^{-2}
6.4	1.19	9.8×10^{-2}
7.3	9.74×10^{-1}	7.1×10^{-2}
8.3	5.00×10^{-1}	7.0×10^{-2}
9.2	3.10×10^{-1}	6.4×10^{-2}
10.1	1.98×10^{-1}	2.0×10^{-2}
11.1	1.90×10^{-1}	1.9×10^{-2}
12.0	2.87×10^{-1}	2.6×10^{-2}
13.0	3.32×10^{-1}	3.0×10^{-2}
13.9	2.88×10^{-1}	4.1×10^{-2}
14.8	2.25×10^{-1}	2.2×10^{-2}
15.8	1.93×10^{-1}	2.0×10^{-2}

Table A.30: ^{24}Mg(α,α') inelastic, $E_x = 9.15$ MeV (1_1^-), $E_\alpha = 130$ MeV

$\theta_{c.m.}$ (deg)	$d\sigma/d\Omega$ (mb/sr)	error (mb/sr)
2.5	6.50×10^{-1}	6.5×10^{-2}
3.4	7.68×10^{-1}	7.4×10^{-2}
4.4	7.99×10^{-1}	7.0×10^{-2}
5.3	8.32×10^{-1}	7.3×10^{-2}
5.4	8.0×10^{-1}	1.1×10^{-1}
6.4	6.23×10^{-1}	9.2×10^{-2}
7.3	4.80×10^{-1}	3.9×10^{-2}
8.3	2.93×10^{-1}	4.9×10^{-2}
9.2	2.39×10^{-1}	6.1×10^{-2}
10.1	1.73×10^{-1}	1.8×10^{-2}
11.1	2.11×10^{-1}	2.1×10^{-2}
12.0	2.82×10^{-1}	4.0×10^{-2}
13.0	3.32×10^{-1}	3.0×10^{-2}
13.9	3.65×10^{-1}	4.9×10^{-2}
14.8	3.32×10^{-1}	3.0×10^{-2}
15.8	2.70×10^{-1}	2.6×10^{-2}

Table A.31: ^{24}Mg(α,α') inelastic, $E_x = 9.31$ MeV (0_3^+), $E_\alpha = 130$ MeV

$\theta_{c.m.}$ (deg)	$d\sigma/d\Omega$ (mb/sr)	error (mb/sr)
0.5	8.36	5.2×10^{-1}
2.5	4.71	3.2×10^{-1}
3.4	1.60	1.3×10^{-1}
4.4	4.57×10^{-1}	4.6×10^{-2}
5.3	3.62×10^{-1}	3.9×10^{-2}
5.4	4.19×10^{-1}	4.4×10^{-2}
6.4	9.52×10^{-1}	8.2×10^{-2}
7.3	1.36	9.4×10^{-2}
8.3	1.13	1.1×10^{-1}
9.2	7.66×10^{-1}	9.7×10^{-2}
10.1	4.62×10^{-1}	3.8×10^{-2}
11.1	3.60×10^{-1}	3.1×10^{-2}
12.0	6.42×10^{-1}	5.0×10^{-2}
13.0	1.06	7.6×10^{-2}
13.9	1.18	1.1×10^{-1}
14.8	1.32	9.3×10^{-2}
15.8	1.16	8.3×10^{-2}

Table A.32: ^{24}Mg(α,α') inelastic, $E_x = 10.36$ MeV (2_7^+), $E_\alpha = 130$ MeV

$\theta_{c.m.}$ (deg)	$d\sigma/d\Omega$ (mb/sr)	error (mb/sr)
0.5	1.18	9.8×10^{-2}
2.5	1.60	1.3×10^{-1}
3.4	1.52	1.3×10^{-1}
4.4	1.76	1.3×10^{-1}
5.3	2.10	1.5×10^{-1}
5.4	2.13	1.6×10^{-1}
6.4	2.32	1.7×10^{-1}
7.3	2.34	1.5×10^{-1}
8.3	2.13	1.4×10^{-1}
9.2	1.71	1.7×10^{-1}
10.1	1.08	1.1×10^{-1}

Table A.33: ^{28}Si(α, α') inelastic, $E_x = 1.78$ MeV (2_1^+), $E_\alpha = 130$ MeV

$\theta_{c.m.}$ (deg)	$d\sigma/d\Omega$ (mb/sr)	error (mb/sr)
0.5	1.28×10^{2}	6.7
2.4	1.30×10^{2}	7.4
3.3	9.08×10^{1}	5.3
4.3	9.01×10^{1}	5.0
5.2	1.32×10^{2}	7.2
5.3	1.38×10^{2}	7.3
6.2	1.82×10^{2}	9.5
7.1	1.82×10^{2}	9.4
8.0	1.61×10^{2}	8.4
9.0	1.01×10^{2}	5.3
9.9	5.20×10^{1}	2.8
10.8	1.58×10^{1}	8.9×10^{-1}
11.7	1.09×10^{1}	6.3×10^{-1}
12.6	2.46×10^{1}	1.4
13.5	4.47×10^{1}	2.4
14.5	5.45×10^{1}	2.9
15.4	5.62×10^{1}	3.0

Table A.34: ^{28}Si(α, α') inelastic, $E_x = 4.62$ MeV (4_1^+), $E_\alpha = 130$ MeV

$\theta_{c.m.}$ (deg)	$d\sigma/d\Omega$ (mb/sr)	error (mb/sr)
2.4	5.94×10^{-1}	9.3×10^{-2}
3.3	7.4×10^{-1}	1.1×10^{-1}
4.3	7.80×10^{-1}	8.4×10^{-2}
5.2	1.07	1.1×10^{-1}
5.3	1.01	8.3×10^{-2}
6.2	1.55	1.7×10^{-1}
7.1	2.06	1.4×10^{-1}
8.1	3.19	2.0×10^{-1}
9.0	3.96	2.5×10^{-1}
9.9	5.09	3.1×10^{-1}
10.8	4.98	3.0×10^{-1}
11.7	4.79	2.9×10^{-1}
12.6	3.37	2.2×10^{-1}
13.6	2.44	1.6×10^{-1}
14.5	1.47	1.0×10^{-1}
15.4	1.24	8.7×10^{-2}

Table A.35: ^{28}Si(α,α') inelastic, $E_x = 4.98$ MeV (0_2^+), $E_\alpha = 130$ MeV

$\theta_{c.m.}$ (deg)	$d\sigma/d\Omega$ (mb/sr)	error (mb/sr)
0.5	3.18×10^{1}	5.6
2.4	2.55×10^{1}	1.7
3.3	1.17×10^{1}	8.7×10^{-1}
4.3	2.68	2.2×10^{-1}
5.2	9.88×10^{-1}	9.9×10^{-2}
5.3	1.21	9.6×10^{-2}
6.2	4.04	3.4×10^{-1}
7.1	5.97	3.6×10^{-1}
8.1	6.23	3.7×10^{-1}
9.0	4.02	2.5×10^{-1}
9.9	2.21	1.5×10^{-1}
10.8	1.28	9.2×10^{-2}
11.7	2.28	1.5×10^{-1}
12.7	3.76	2.4×10^{-1}
13.6	5.42	3.3×10^{-1}
14.5	5.33	3.2×10^{-1}
15.4	4.81	2.9×10^{-1}

Table A.36: ^{28}Si(α,α') inelastic, $E_x = 6.69$ MeV (0_3^+), $E_\alpha = 130$ MeV

$\theta_{c.m.}$ (deg)	$d\sigma/d\Omega$ (mb/sr)	error (mb/sr)
0.5	3.18	4.9×10^{-1}
2.4	2.56	2.6×10^{-1}
3.3	1.39	1.7×10^{-1}
4.3	6.5×10^{-1}	1.5×10^{-1}
5.2	3.6×10^{-1}	1.4×10^{-1}
5.3	3.84×10^{-1}	3.9×10^{-2}
7.1	9.42×10^{-1}	7.1×10^{-2}
8.1	1.13	2.6×10^{-1}
9.0	8.4×10^{-1}	1.5×10^{-1}
9.9	6.5×10^{-1}	2.1×10^{-1}
10.8	2.56×10^{-1}	2.5×10^{-2}
12.7	1.51×10^{-1}	1.7×10^{-2}
13.6	1.83×10^{-1}	2.0×10^{-2}
14.5	2.14×10^{-1}	2.1×10^{-2}
15.4	1.94×10^{-1}	5.1×10^{-2}

Table A.37: ^{28}Si(α, α') inelastic, $E_x = 6.88$ MeV (3_1^-), $E_\alpha = 130$ MeV

$\theta_{c.m.}$ (deg)	$d\sigma/d\Omega$ (mb/sr)	error (mb/sr)
0.5	4.8	1.5
2.4	1.17×10^{1}	8.7×10^{-1}
3.3	1.56×10^{1}	1.1
4.3	1.94×10^{1}	1.2
5.2	2.41×10^{1}	1.5
5.3	2.48×10^{1}	1.4
6.2	3.25×10^{1}	1.8
7.1	4.08×10^{1}	2.2
8.1	4.97×10^{1}	2.7
9.0	4.94×10^{1}	2.7
9.9	4.63×10^{1}	2.5
10.8	3.29×10^{1}	1.8
11.7	2.29×10^{1}	1.3
12.7	1.23×10^{1}	7.0×10^{-1}
13.6	8.84	5.2×10^{-1}
14.5	8.69	5.0×10^{-1}
15.4	1.19×10^{1}	6.7×10^{-1}

Table A.38: ^{28}Si(α, α') inelastic, $E_x = 7.93$ MeV (2_2^+), $E_\alpha = 130$ MeV

$\theta_{c.m.}$ (deg)	$d\sigma/d\Omega$ (mb/sr)	error (mb/sr)
0.5	3.4	1.4
2.4	3.30	5.4×10^{-1}
3.3	2.60	2.6×10^{-1}
4.3	2.89	2.3×10^{-1}
5.2	3.81	2.9×10^{-1}
5.3	3.83	2.6×10^{-1}
6.2	4.38	2.9×10^{-1}
7.1	3.82	2.4×10^{-1}
8.1	3.37	2.2×10^{-1}
9.0	1.68	1.2×10^{-1}
9.9	8.44×10^{-1}	6.6×10^{-2}
10.8	3.81×10^{-1}	3.4×10^{-2}
11.8	5.50×10^{-1}	4.6×10^{-2}
12.7	8.56×10^{-1}	6.6×10^{-2}
13.6	1.25	9.1×10^{-2}
14.5	1.10	7.3×10^{-2}
15.4	9.69×10^{-1}	7.1×10^{-2}

Table A.39: ^{28}Si(α,α') inelastic, $E_x = 8.26$ MeV (2_3^+), $E_\alpha = 130$ MeV

$\theta_{c.m.}$ (deg)	$d\sigma/d\Omega$ (mb/sr)	error (mb/sr)
2.4	4.1×10^{-1}	1.6×10^{-1}
4.3	3.05×10^{-1}	4.3×10^{-2}
5.2	2.83×10^{-1}	4.1×10^{-2}
5.3	2.77×10^{-1}	3.1×10^{-2}
6.2	2.69×10^{-1}	3.0×10^{-2}
7.2	4.13×10^{-1}	3.7×10^{-2}
8.1	4.99×10^{-1}	6.5×10^{-2}
9.0	5.49×10^{-1}	4.7×10^{-2}
9.9	5.77×10^{-1}	4.9×10^{-2}
10.8	5.07×10^{-1}	4.3×10^{-2}
11.8	3.74×10^{-1}	3.4×10^{-2}
12.7	2.35×10^{-1}	2.4×10^{-2}
13.6	1.86×10^{-1}	2.0×10^{-2}
14.5	1.99×10^{-1}	2.0×10^{-2}
15.4	3.47×10^{-1}	3.1×10^{-2}

Table A.40: ^{28}Si(α,α') inelastic, $E_x = 8.90$ MeV (1_1^-), $E_\alpha = 130$ MeV

$\theta_{c.m.}$ (deg)	$d\sigma/d\Omega$ (mb/sr)	error (mb/sr)
0.5	1.61	2.2×10^{-1}
2.4	3.27	2.6×10^{-1}
3.3	3.31	2.6×10^{-1}
4.3	2.21	1.6×10^{-1}
5.2	1.05	8.4×10^{-2}
5.3	9.08×10^{-1}	7.4×10^{-2}
6.2	2.91×10^{-1}	3.1×10^{-2}
7.2	5.07×10^{-1}	4.2×10^{-2}
8.1	1.40	9.8×10^{-2}
9.0	2.04	1.5×10^{-1}
9.9	2.14	1.5×10^{-1}
10.8	1.68	1.2×10^{-1}
11.8	1.24	9.0×10^{-2}
12.7	8.12×10^{-1}	5.9×10^{-2}
13.6	9.69×10^{-1}	6.8×10^{-2}
14.5	1.27	8.9×10^{-2}
15.4	1.57	1.1×10^{-1}

Table A.41: ^{28}Si(α, α') inelastic, $E_x = 9.48$ MeV (2_4^+), $E_\alpha = 130$ MeV

$\theta_{c.m.}$ (deg)	$d\sigma/d\Omega$ (mb/sr)	error (mb/sr)
0.5	9.08×10^{-1}	7.1×10^{-2}
2.4	1.04	1.4×10^{-1}
3.4	1.15	1.5×10^{-1}
4.3	1.32	1.2×10^{-1}
5.2	1.73	1.5×10^{-1}
5.3	1.70	1.3×10^{-1}
6.2	1.97	1.4×10^{-1}
7.2	1.74	1.2×10^{-1}
8.1	1.51	1.1×10^{-1}
9.0	1.16	8.6×10^{-2}
9.9	6.29×10^{-1}	5.2×10^{-2}
10.8	4.56×10^{-1}	4.0×10^{-2}
11.8	4.39×10^{-1}	3.8×10^{-2}
12.7	6.64×10^{-1}	5.4×10^{-2}
13.6	7.80×10^{-1}	6.1×10^{-2}
14.5	6.57×10^{-1}	5.1×10^{-2}
15.4	5.42×10^{-1}	4.4×10^{-2}

Table A.42: ^{28}Si(α, α') inelastic, $E_x = 9.93$ MeV (1_2^-), $E_\alpha = 130$ MeV

$\theta_{c.m.}$ (deg)	$d\sigma/d\Omega$ (mb/sr)	error (mb/sr)
0.5	1.48	2.2×10^{-1}
2.4	5.61	4.0×10^{-1}
3.4	7.27	5.0×10^{-1}
4.3	6.69	5.0×10^{-1}
5.2	4.69	3.7×10^{-1}
5.3	4.08	3.3×10^{-1}
6.2	2.01	1.9×10^{-1}
7.2	7.26×10^{-1}	5.6×10^{-2}
8.1	6.27×10^{-1}	5.0×10^{-2}
9.0	1.47	1.1×10^{-1}
9.9	1.85	1.4×10^{-1}
10.8	1.83	1.2×10^{-1}
11.8	1.47	1.0×10^{-1}
12.7	7.75×10^{-1}	5.6×10^{-2}
13.6	3.24×10^{-1}	2.8×10^{-2}
14.5	2.30×10^{-1}	2.3×10^{-2}
15.4	4.02×10^{-1}	3.5×10^{-2}

Table A.43: ^{28}Si(α, α') inelastic, $E_x = 10.18$ MeV (3_2^-), $E_\alpha = 130$ MeV

$\theta_{c.m.}$ (deg)	$d\sigma/d\Omega$ (mb/sr)	error (mb/sr)
0.5	4.63	3.1×10^{-1}
2.4	6.78	6.1×10^{-1}
3.4	7.91	6.8×10^{-1}
4.3	8.38	6.0×10^{-1}
5.2	8.97	6.4×10^{-1}
5.3	8.59	6.1×10^{-1}
6.2	9.64	6.6×10^{-1}
7.2	1.01×10^{1}	6.5×10^{-1}
8.1	1.16×10^{1}	7.4×10^{-1}
9.0	1.15×10^{1}	7.9×10^{-1}
9.9	1.10×10^{1}	7.6×10^{-1}
10.8	7.83	5.2×10^{-1}
11.8	6.08	4.2×10^{-1}
12.7	3.33	2.4×10^{-1}
13.6	2.25	1.7×10^{-1}
14.5	2.06	1.7×10^{-1}
15.5	2.56	2.0×10^{-1}

Table A.44: ^{28}Si(α, α') inelastic, $E_x = 10.51$ MeV (2_5^+), $E_\alpha = 130$ MeV

$\theta_{c.m.}$ (deg)	$d\sigma/d\Omega$ (mb/sr)	error (mb/sr)
0.5	7.7×10^{-1}	4.4×10^{-1}
2.4	3.76×10^{-1}	8.5×10^{-2}
3.4	4.20×10^{-1}	9.3×10^{-2}
4.3	8.2×10^{-1}	1.0×10^{-1}
5.2	1.17	1.3×10^{-1}
5.3	1.27	1.4×10^{-1}
6.2	1.35	1.4×10^{-1}
7.2	1.22	1.1×10^{-1}
8.1	8.20×10^{-1}	8.7×10^{-2}
9.0	4.30×10^{-1}	7.1×10^{-2}
9.9	1.83×10^{-1}	4.2×10^{-2}
10.8	8.9×10^{-2}	2.3×10^{-2}
11.8	2.30×10^{-1}	3.6×10^{-2}
12.7	2.69×10^{-1}	3.8×10^{-2}
13.6	3.57×10^{-1}	4.4×10^{-2}
14.5	3.60×10^{-1}	4.7×10^{-2}
15.5	2.67×10^{-1}	4.0×10^{-2}

Table A.45: ^{40}Ca(α,α') inelastic, $E_x = 3.35$ MeV (0_2^+), $E_\alpha = 130$ MeV

$\theta_{c.m.}$ (deg)	$d\sigma/d\Omega$ (mb/sr)	error (mb/sr)
0.4	2.8×10^{-1}	1.5×10^{-1}
4.1	1.80×10^{-1}	2.6×10^{-2}
6.0	2.18×10^{-1}	5.4×10^{-2}
6.9	1.29×10^{-1}	1.6×10^{-2}
7.7	6.6×10^{-2}	2.4×10^{-2}
9.5	3.45×10^{-2}	6.6×10^{-3}
10.4	6.2×10^{-2}	1.4×10^{-2}
11.3	7.2×10^{-2}	1.6×10^{-2}
12.1	5.65×10^{-2}	7.9×10^{-3}
13.0	2.34×10^{-2}	6.8×10^{-3}
13.9	3.39×10^{-2}	6.6×10^{-3}
14.8	7.9×10^{-2}	1.2×10^{-2}

Table A.46: ^{40}Ca(α,α') inelastic, $E_x = 3.74$ MeV (3_1^-), $E_\alpha = 130$ MeV

$\theta_{c.m.}$ (deg)	$d\sigma/d\Omega$ (mb/sr)	error (mb/sr)
0.4	5.10	3.1×10^{-1}
2.3	3.02×10^{1}	1.7
3.2	3.97×10^{1}	2.3
4.1	4.22×10^{1}	2.4
5.0	4.60×10^{1}	3.0
5.1	4.68×10^{1}	3.0
6.0	5.29×10^{1}	3.3
6.9	6.43×10^{1}	3.4
7.7	8.02×10^{1}	4.2
9.5	6.76×10^{1}	3.6
10.4	3.96×10^{1}	2.1
11.3	2.08×10^{1}	1.2
12.2	7.77	4.5×10^{-1}
13.0	8.39	4.8×10^{-1}
13.9	1.41×10^{1}	8.1×10^{-1}
14.8	2.17×10^{1}	1.2

Table A.47: ^{40}Ca(α,α') inelastic, $E_x = 3.90$ MeV (2_1^+), $E_\alpha = 130$ MeV

$\theta_{c.m.}$ (deg)	$d\sigma/d\Omega$ (mb/sr)	error (mb/sr)
0.4	6.36	3.8×10^{-1}
2.3	1.01×10^{1}	6.4×10^{-1}
3.2	7.89	5.1×10^{-1}
4.1	1.19×10^{1}	7.3×10^{-1}
5.0	1.53×10^{1}	1.2
5.1	1.67×10^{1}	1.3
6.0	2.10×10^{1}	1.5
6.9	1.94×10^{1}	1.1
7.7	1.52×10^{1}	8.6×10^{-1}
8.6	6.08	3.7×10^{-1}
9.5	1.74	1.2×10^{-1}
10.4	1.46	1.0×10^{-1}
11.3	3.88	2.4×10^{-1}
12.2	5.97	3.5×10^{-1}
13.0	6.72	3.9×10^{-1}
13.9	4.90	3.0×10^{-1}
14.8	2.81	1.9×10^{-1}

Table A.48: ^{40}Ca(α, α') inelastic, $E_x = 4.49$ MeV (5_1^-), $E_\alpha = 130$ MeV

$\theta_{c.m.}$ (deg)	$d\sigma/d\Omega$ (mb/sr)	error (mb/sr)
0.4	4.54×10^{-1}	3.8×10^{-2}
4.1	8.71×10^{-1}	8.0×10^{-2}
5.0	9.18×10^{-1}	8.3×10^{-2}
5.1	8.4×10^{-1}	1.4×10^{-1}
6.0	1.01	3.0×10^{-1}
6.9	1.46	1.1×10^{-1}
7.7	2.16	1.5×10^{-1}
8.6	2.95	1.9×10^{-1}
9.5	4.34	2.7×10^{-1}
10.4	5.11	3.1×10^{-1}
11.3	5.97	3.6×10^{-1}
12.2	5.95	3.5×10^{-1}
13.0	5.63	3.3×10^{-1}
13.9	4.02	2.6×10^{-1}
14.8	2.79	1.8×10^{-1}

Table A.49: ^{40}Ca(α, α') inelastic, $E_x = 5.90$ MeV (1_1^-), $E_\alpha = 130$ MeV

$\theta_{c.m.}$ (deg)	$d\sigma/d\Omega$ (mb/sr)	error (mb/sr)
0.4	3.49×10^{-1}	3.1×10^{-2}
2.3	3.61	2.6×10^{-1}
3.2	3.65	2.6×10^{-1}
4.1	3.11	2.2×10^{-1}
5.0	1.84	1.5×10^{-1}
5.1	1.60	1.3×10^{-1}
6.0	4.91×10^{-1}	9.5×10^{-2}
6.9	2.5×10^{-1}	1.3×10^{-1}
7.7	5.43×10^{-1}	4.7×10^{-2}
8.6	9.13×10^{-1}	7.1×10^{-2}
9.5	1.10	8.3×10^{-2}
10.4	7.86×10^{-1}	6.1×10^{-2}
11.3	4.93×10^{-1}	4.2×10^{-2}
12.2	1.64×10^{-1}	1.7×10^{-2}
13.0	1.49×10^{-1}	1.6×10^{-2}
13.9	4.17×10^{-1}	3.8×10^{-2}
14.8	4.40×10^{-1}	4.0×10^{-2}

Table A.50: ^{40}Ca(α,α') inelastic, $E_x = 6.29$ MeV (3^-_2), $E_\alpha = 130$ MeV

$\theta_{c.m.}$ (deg)	$d\sigma/d\Omega$ (mb/sr)	error (mb/sr)
0.4	1.20	8.5×10^{-2}
2.3	5.53	3.8×10^{-1}
3.2	6.57	4.4×10^{-1}
4.1	8.72	5.5×10^{-1}
5.0	1.00×10^{1}	6.2×10^{-1}
5.1	1.02×10^{1}	6.4×10^{-1}
6.0	1.25×10^{1}	7.7×10^{-1}
6.9	1.19×10^{1}	8.7×10^{-1}
7.7	1.27×10^{1}	8.3×10^{-1}
8.6	1.18×10^{1}	6.8×10^{-1}
9.5	9.54	5.6×10^{-1}
10.4	5.17	3.2×10^{-1}
11.3	2.36	1.6×10^{-1}
12.2	1.12	7.9×10^{-2}
13.0	1.64	1.1×10^{-1}
13.9	2.70	1.8×10^{-1}
14.8	3.58	2.3×10^{-1}

Table A.51: ^{40}Ca(α,α') inelastic, $E_x = 8.09$ MeV (2^+_2), $E_\alpha = 130$ MeV

$\theta_{c.m.}$ (deg)	$d\sigma/d\Omega$ (mb/sr)	error (mb/sr)
0.4	2.57	1.7×10^{-1}
2.3	3.01	3.0×10^{-1}
3.2	3.15	3.2×10^{-1}
4.1	5.11	3.4×10^{-1}
5.0	6.27	4.1×10^{-1}
5.1	6.58	4.3×10^{-1}
6.0	6.81	4.4×10^{-1}
6.9	5.00	3.1×10^{-1}
7.8	2.55	3.0×10^{-1}
8.6	1.37	9.9×10^{-2}
9.5	6.61×10^{-1}	5.4×10^{-2}
10.4	1.03	7.7×10^{-2}
11.3	1.79	1.2×10^{-1}
12.2	2.10	1.4×10^{-1}
13.1	1.92	1.3×10^{-1}
13.9	1.33	9.7×10^{-2}
14.8	9.41×10^{-1}	7.3×10^{-2}

Table A.52: ^{40}Ca(α,α') inelastic, $E_x = 8.28$ MeV (0_3^+), $E_\alpha = 130$ MeV

$\theta_{c.m.}$ (deg)	$d\sigma/d\Omega$ (mb/sr)	error (mb/sr)
0.4	9.54	5.5×10^{-1}
2.3	4.52	3.2×10^{-1}
3.2	1.21	1.1×10^{-1}
4.1	1.62×10^{-1}	2.4×10^{-2}
5.0	4.75×10^{-1}	5.1×10^{-2}
5.1	4.62×10^{-1}	5.0×10^{-2}
6.0	1.07	9.5×10^{-2}
6.9	1.19	8.8×10^{-2}
7.8	9.4×10^{-1}	2.0×10^{-1}
8.6	6.33×10^{-1}	7.3×10^{-2}
9.5	3.37×10^{-1}	6.0×10^{-2}
10.4	1.52×10^{-1}	1.7×10^{-2}
11.3	4.24×10^{-1}	3.7×10^{-2}
12.2	5.23×10^{-1}	4.2×10^{-2}
13.1	5.24×10^{-1}	4.2×10^{-2}
13.9	3.20×10^{-1}	3.1×10^{-2}
14.8	1.59×10^{-1}	1.9×10^{-2}

Table A.53: ^{40}Ca(α,α') inelastic, $E_x = 8.37$ MeV (4_1^+), $E_\alpha = 130$ MeV

$\theta_{c.m.}$ (deg)	$d\sigma/d\Omega$ (mb/sr)	error (mb/sr)
0.4	1.03	3.9×10^{-1}
2.3	7.75×10^{-1}	7.6×10^{-2}
3.2	5.84×10^{-1}	6.1×10^{-2}
4.1	8.12×10^{-1}	7.6×10^{-2}
5.0	1.05	9.3×10^{-2}
5.1	1.08	9.5×10^{-2}
6.0	1.55	1.3×10^{-1}
6.9	1.85	1.3×10^{-1}
7.8	2.25	2.9×10^{-1}
8.6	2.53	2.2×10^{-1}
9.5	3.13	2.0×10^{-1}
10.4	2.74	1.8×10^{-1}
11.3	2.37	1.6×10^{-1}
12.2	1.60	1.1×10^{-1}
13.1	9.78×10^{-1}	7.0×10^{-2}
13.9	4.75×10^{-1}	4.2×10^{-2}
14.8	3.94×10^{-1}	3.7×10^{-2}

Table A.54: ^{40}Ca(α, α') inelastic,
$E_x = 8.58$ MeV (2_3^+),
$E_\alpha = 130$ MeV

$\theta_{c.m.}$ (deg)	$d\sigma/d\Omega$ (mb/sr)	error (mb/sr)
0.4	1.23	8.7×10^{-2}
2.3	1.68	1.4×10^{-1}
3.2	2.11	1.7×10^{-1}
4.1	2.70	2.0×10^{-1}
5.0	3.54	2.5×10^{-1}
5.1	3.74	2.6×10^{-1}
6.0	4.26	3.0×10^{-1}
6.9	3.44	2.2×10^{-1}
7.8	2.42	2.9×10^{-1}
8.6	1.03	1.2×10^{-1}
9.5	4.97×10^{-1}	4.3×10^{-2}
10.4	4.80×10^{-1}	4.1×10^{-2}
11.3	7.67×10^{-1}	6.0×10^{-2}
12.2	1.09	7.7×10^{-2}
13.1	1.20	8.4×10^{-2}
13.9	9.24×10^{-1}	7.2×10^{-2}
14.8	5.21×10^{-1}	4.5×10^{-2}

A.2.2 $E_\alpha = 386$ MeV

Table A.55: ^{12}C(α, α') inelastic, $E_x = 4.44$ MeV (2_1^+), $E_\alpha = 386$ MeV

$\theta_{c.m.}$ (deg)	$d\sigma/d\Omega$ (mb/sr)	error (mb/sr)
0.4	7.55×10^{1}	8.5
1.0	7.76×10^{1}	5.1
1.8	7.31×10^{1}	4.1
2.5	6.43×10^{1}	1.0
3.0	6.13×10^{1}	1.0
3.5	6.47×10^{1}	1.0
4.0	7.41×10^{1}	1.1
4.9	1.00×10^{2}	5.0
5.4	1.04×10^{2}	5.2
5.9	1.06×10^{2}	5.3
6.2	1.12×10^{2}	5.6
6.7	1.06×10^{2}	5.3
7.3	8.80×10^{1}	4.4
7.8	6.75×10^{1}	3.4
8.6	4.55×10^{1}	2.3
9.1	3.17×10^{1}	1.6
9.6	2.12×10^{1}	1.1
10.2	1.60×10^{1}	8.0×10^{-1}
11.0	1.39×10^{1}	7.0×10^{-1}
11.5	1.64×10^{1}	8.2×10^{-1}
12.1	1.92×10^{1}	9.6×10^{-1}
12.6	2.04×10^{1}	1.0
13.4	2.16×10^{1}	1.1
14.0	1.98×10^{1}	9.9×10^{-1}
14.5	1.72×10^{1}	8.6×10^{-1}

Table A.55: (Continued)

$\theta_{c.m.}$ (deg)	$d\sigma/d\Omega$ (mb/sr)	error (mb/sr)
15.0	1.36×10^{1}	6.8×10^{-1}
15.8	1.02×10^{1}	5.1×10^{-1}
16.4	7.27	3.7×10^{-1}
16.9	5.07	2.6×10^{-1}
17.5	3.46	1.7×10^{-1}
18.3	1.98	1.0×10^{-1}
18.8	1.71	8.7×10^{-2}
19.3	1.60	8.2×10^{-2}
19.9	1.52	7.8×10^{-2}
20.7	1.44	8.0×10^{-2}
21.2	1.29	7.3×10^{-2}
21.8	1.10	6.3×10^{-2}
22.3	9.26×10^{-1}	5.4×10^{-2}
22.5	8.20×10^{-1}	2.5×10^{-2}
23.1	6.68×10^{-1}	2.1×10^{-2}
23.6	5.26×10^{-1}	1.6×10^{-2}
24.2	3.71×10^{-1}	1.1×10^{-2}
24.7	2.95×10^{-1}	9.1×10^{-3}
25.2	2.34×10^{-1}	7.2×10^{-3}
25.8	1.85×10^{-1}	5.8×10^{-3}
26.3	1.32×10^{-1}	4.0×10^{-3}
26.8	1.15×10^{-1}	3.5×10^{-3}
27.4	9.95×10^{-2}	3.1×10^{-3}
27.9	8.46×10^{-2}	2.6×10^{-3}
28.5	6.45×10^{-2}	2.0×10^{-3}
29.0	5.72×10^{-2}	1.8×10^{-3}
29.5	4.80×10^{-2}	1.5×10^{-3}

Table A.56: $^{12}C(\alpha,\alpha')$ inelastic, $E_x = 7.65$ MeV (0_2^+), $E_\alpha = 386$ MeV

$\theta_{c.m.}$ (deg)	$d\sigma/d\Omega$ (mb/sr)	error (mb/sr)
0.4	8.27×10^{1}	1.6
1.0	7.32×10^{1}	9.0×10^{-1}
1.8	5.14×10^{1}	6.0×10^{-1}
2.5	3.27×10^{1}	7.0×10^{-1}
3.0	1.96×10^{1}	6.0×10^{-1}
3.5	9.10	4.0×10^{-1}
4.1	2.80	2.0×10^{-1}
4.3	9.01×10^{-1}	5.8×10^{-2}
4.9	1.07	6.7×10^{-2}
5.4	2.78	1.5×10^{-1}
5.9	4.46	2.4×10^{-1}
6.2	6.01	3.2×10^{-1}
6.7	6.82	3.6×10^{-1}
7.3	5.93	3.1×10^{-1}
7.8	4.49	2.4×10^{-1}
8.6	2.51	1.3×10^{-1}
9.1	1.44	7.3×10^{-2}
9.6	1.01	5.2×10^{-2}
10.2	1.02	5.2×10^{-2}
11.0	1.50	7.6×10^{-2}

Table A.56: (Continued)

$\theta_{c.m.}$ (deg)	$d\sigma/d\Omega$ (mb/sr)	error (mb/sr)
11.5	1.90	9.6×10^{-2}
12.1	2.08	1.1×10^{-1}
12.6	1.99	1.0×10^{-1}
13.4	1.71	8.6×10^{-2}
14.0	1.38	7.0×10^{-2}
14.5	9.59×10^{-1}	4.9×10^{-2}
15.0	6.04×10^{-1}	3.1×10^{-2}
15.9	3.45×10^{-1}	1.9×10^{-2}
16.4	2.43×10^{-1}	1.4×10^{-2}
16.9	1.93×10^{-1}	1.1×10^{-2}
17.5	2.11×10^{-1}	1.2×10^{-2}
18.3	2.03×10^{-1}	1.2×10^{-2}
18.8	1.92×10^{-1}	1.1×10^{-2}
19.4	1.77×10^{-1}	1.0×10^{-2}
19.9	1.56×10^{-1}	9.1×10^{-3}
20.7	1.24×10^{-1}	1.2×10^{-2}
21.3	7.80×10^{-2}	9.0×10^{-3}
21.8	6.62×10^{-2}	8.2×10^{-3}
22.3	3.91×10^{-2}	6.1×10^{-3}

Table A.57: ^{12}C(α,α') inelastic, $E_x = 9.64$ MeV (3_1^-), $E_\alpha = 386$ MeV

$\theta_{c.m.}$ (deg)	$d\sigma/d\Omega$ (mb/sr)	error (mb/sr)
0.4	2.55	3.4×10^{-1}
1.0	3.24	2.5×10^{-1}
1.5	2.86	2.6×10^{-1}
2.1	4.04	2.6×10^{-1}
2.7	5.50	7.4×10^{-2}
3.3	6.80	7.7×10^{-2}
3.8	8.55	8.2×10^{-2}
4.3	1.07×10^{1}	8.9×10^{-2}
4.3	1.01×10^{1}	1.1×10^{-1}
4.9	1.28×10^{1}	1.2×10^{-1}
5.4	1.50×10^{1}	1.3×10^{-1}
5.9	1.69×10^{1}	1.4×10^{-1}
6.1	2.05×10^{1}	3.9×10^{-1}
6.7	2.06×10^{1}	3.9×10^{-1}
7.2	2.12×10^{1}	3.9×10^{-1}
7.8	1.94×10^{1}	3.7×10^{-1}
8.5	1.59×10^{1}	3.9×10^{-2}
9.0	1.29×10^{1}	3.5×10^{-2}
9.6	9.43	3.0×10^{-2}
10.1	6.71	2.6×10^{-2}
10.9	3.77	1.9×10^{-2}
11.5	3.04	1.7×10^{-2}
12.0	2.83	1.7×10^{-2}
12.5	2.84	1.6×10^{-2}
13.4	3.27	1.7×10^{-2}

Table A.57: (Continued)

$\theta_{c.m.}$ (deg)	$d\sigma/d\Omega$ (mb/sr)	error (mb/sr)
13.9	3.40	1.8×10^{-2}
14.4	3.26	1.7×10^{-2}
15.0	2.96	1.6×10^{-2}
15.8	2.20	1.5×10^{-2}
16.3	1.73	1.3×10^{-2}
16.9	1.29	1.1×10^{-2}
17.4	8.74×10^{-1}	9.2×10^{-3}
18.2	4.26×10^{-1}	6.8×10^{-3}
18.8	3.19×10^{-1}	5.9×10^{-3}
19.3	2.41×10^{-1}	5.2×10^{-3}
19.9	2.01×10^{-1}	4.8×10^{-3}
20.7	1.38×10^{-1}	1.0×10^{-2}
21.2	1.24×10^{-1}	9.9×10^{-3}
21.8	1.21×10^{-1}	9.7×10^{-3}
22.3	9.24×10^{-2}	8.7×10^{-3}
23.1	9.54×10^{-2}	8.0×10^{-3}
23.7	7.60×10^{-2}	7.1×10^{-3}
24.2	6.36×10^{-2}	6.5×10^{-3}
24.7	4.53×10^{-2}	5.5×10^{-3}
25.5	2.66×10^{-2}	3.5×10^{-3}
26.1	1.85×10^{-2}	3.0×10^{-3}
26.6	1.59×10^{-2}	2.7×10^{-3}
27.2	1.30×10^{-2}	2.5×10^{-3}

Table A.58: $^{16}O(\alpha,\alpha')$ inelastic, $E_x = 6.13$ MeV (3^-_1), $E_\alpha = 386$ MeV

$\theta_{c.m.}$ (deg)	$d\sigma/d\Omega$ (mb/sr)	error (mb/sr)
2.4	1.91×10^{1}	1.2
2.9	2.15×10^{1}	1.3
3.4	2.40×10^{1}	1.5
3.9	2.86×10^{1}	1.7
4.0	2.91×10^{1}	1.8
4.4	3.85×10^{1}	2.3
4.9	4.72×10^{1}	2.7
5.4	5.31×10^{1}	3.1
5.6	5.43×10^{1}	3.1
6.1	6.08×10^{1}	3.5
6.6	6.14×10^{1}	3.5
7.1	6.06×10^{1}	3.4

Table A.59: $^{16}O(\alpha,\alpha')$ inelastic, $E_x = 6.92$ MeV (2^+_1), $E_\alpha = 386$ MeV

$\theta_{c.m.}$ (deg)	$d\sigma/d\Omega$ (mb/sr)	error (mb/sr)
2.4	2.49×10^{1}	1.5
2.9	3.24×10^{1}	2.0
3.4	4.18×10^{1}	2.5
3.9	5.40×10^{1}	3.1
4.0	5.11×10^{1}	3.0
4.4	5.98×10^{1}	3.4
4.9	6.75×10^{1}	3.8
5.4	6.44×10^{1}	3.7
5.6	6.21×10^{1}	3.5
6.1	5.52×10^{1}	3.2
6.6	3.95×10^{1}	2.3
7.1	2.84×10^{1}	1.7

Table A.60: $^{16}O(\alpha,\alpha')$ inelastic, $E_x = 11.52$ MeV (2^+_3), $E_\alpha = 386$ MeV

$\theta_{c.m.}$ (deg)	$d\sigma/d\Omega$ (mb/sr)	error (mb/sr)
1.0	1.25×10^{1}	1.8
2.4	1.56×10^{1}	1.0
2.9	1.91×10^{1}	1.2
3.4	2.43×10^{1}	1.5
3.9	3.00×10^{1}	1.8
4.0	3.39×10^{1}	2.0
4.9	3.45×10^{1}	2.1
5.4	3.26×10^{1}	2.0
5.6	3.19×10^{1}	1.9
6.1	2.73×10^{1}	1.6
6.6	2.37×10^{1}	1.4
7.1	1.57×10^{1}	9.9×10^{-1}

Table A.61: $^{16}O(\alpha,\alpha')$ inelastic, $E_x = 12.05$ MeV (0^+_3), $E_\alpha = 386$ MeV

$\theta_{c.m.}$ (deg)	$d\sigma/d\Omega$ (mb/sr)	error (mb/sr)
1.0	1.63×10^{1}	1.0
2.4	4.84	4.2×10^{-1}
2.9	1.81	2.0×10^{-1}
3.4	2.80×10^{-1}	5.4×10^{-2}
3.9	2.80×10^{-1}	5.4×10^{-2}
4.4	8.6×10^{-1}	1.1×10^{-1}
4.9	1.75	2.0×10^{-1}
5.4	2.12	2.3×10^{-1}
5.6	2.24	2.2×10^{-1}
6.1	2.25	2.2×10^{-1}
6.6	2.13	2.2×10^{-1}
7.1	1.02	1.3×10^{-1}

Table A.62: ^{20}Ne(α,α') inelastic, $E_x = 1.63$ MeV (2_1^+), $E_\alpha = 386$ MeV

$\theta_{c.m.}$ (deg)	$d\sigma/d\Omega$ (mb/sr)	error (mb/sr)
2.9	1.94×10^{2}	9.7
3.4	2.51×10^{2}	1.2×10^{1}
3.9	2.86×10^{2}	1.4×10^{1}
4.1	3.25×10^{2}	1.6×10^{1}
4.6	3.25×10^{2}	1.6×10^{1}
5.1	2.93×10^{2}	1.4×10^{1}
5.6	2.29×10^{2}	1.1×10^{1}
7.3	3.14×10^{1}	2.3
7.8	2.89×10^{1}	2.1
8.3	3.41×10^{1}	2.4
8.8	4.18×10^{1}	2.9
9.0	4.27×10^{1}	2.6
9.5	4.58×10^{1}	2.7
10.0	4.14×10^{1}	2.5

Table A.63: ^{20}Ne(α,α') inelastic, $E_x = 4.25$ MeV (4_1^+), $E_\alpha = 386$ MeV

$\theta_{c.m.}$ (deg)	$d\sigma/d\Omega$ (mb/sr)	error (mb/sr)
4.6	3.47	2.8×10^{-1}
5.1	5.73	4.1×10^{-1}
5.6	7.04	4.8×10^{-1}
7.3	8.76	8.6×10^{-1}
7.8	7.63	7.7×10^{-1}
8.3	5.53	6.1×10^{-1}
8.8	3.72	4.7×10^{-1}
9.0	3.18	3.2×10^{-1}
9.5	2.24	2.6×10^{-1}
10.0	2.03	2.4×10^{-1}
10.5	2.29	2.5×10^{-1}
10.7	2.61	2.3×10^{-1}
11.2	3.39	2.8×10^{-1}
11.7	3.57	2.9×10^{-1}
12.2	3.55	2.9×10^{-1}
12.4	3.50	2.4×10^{-1}
12.9	3.19	2.2×10^{-1}
13.4	2.58	1.8×10^{-1}
13.9	1.87	1.4×10^{-1}

Table A.64: ^{20}Ne(α,α') inelastic, $E_x = 5.62$ MeV (3^-_1), $E_\alpha = 386$ MeV

$\theta_{c.m.}$ (deg)	$d\sigma/d\Omega$ (mb/sr)	error (mb/sr)
2.4	1.33×10^{1}	8.6×10^{-1}
2.9	1.54×10^{1}	9.6×10^{-1}
5.1	2.45×10^{1}	1.4
5.6	2.56×10^{1}	1.4
7.3	1.99×10^{1}	1.6
7.8	1.36×10^{1}	1.2
12.4	5.01	3.3×10^{-1}
12.9	4.25	2.9×10^{-1}
13.4	3.07	2.2×10^{-1}
13.9	2.38	1.8×10^{-1}

Table A.65: ^{20}Ne(α,α') inelastic, $E_x = 6.73$ MeV (0^+_2), $E_\alpha = 386$ MeV

$\theta_{c.m.}$ (deg)	$d\sigma/d\Omega$ (mb/sr)	error (mb/sr)
0.5	8.02×10^{1}	5.3
2.4	3.30	2.7×10^{-1}
2.9	7.9×10^{-1}	1.1×10^{-1}
3.4	1.05	1.5×10^{-1}

Table A.66: ^{24}Mg(α,α') inelastic, $E_x = 1.37$ MeV (2^+_1), $E_\alpha = 386$ MeV

$\theta_{c.m.}$ (deg)	$d\sigma/d\Omega$ (mb/sr)	error (mb/sr)
2.2	2.27×10^{2}	1.2×10^{1}
2.7	2.09×10^{2}	1.2×10^{1}
3.2	3.94×10^{2}	2.1×10^{1}
3.6	5.23×10^{2}	2.7×10^{1}
3.7	5.35×10^{2}	3.2×10^{1}
4.1	6.19×10^{2}	3.6×10^{1}
4.6	6.45×10^{2}	3.8×10^{1}
5.1	5.96×10^{2}	3.5×10^{1}
5.1	5.47×10^{2}	2.9×10^{1}
5.6	4.37×10^{2}	2.3×10^{1}
6.1	3.25×10^{2}	1.7×10^{1}
6.5	2.00×10^{2}	1.1×10^{1}
6.9	1.23×10^{2}	6.8
7.4	8.09×10^{1}	4.6
7.8	7.48×10^{1}	4.2
8.3	9.35×10^{1}	5.2
8.6	1.18×10^{2}	6.5
9.1	1.42×10^{2}	7.7
9.6	1.52×10^{2}	8.3
10.0	1.41×10^{2}	7.7
10.4	1.20×10^{2}	6.6
10.8	9.78×10^{1}	5.4
11.3	6.72×10^{1}	3.8
11.8	4.60×10^{1}	2.6

Table A.67: ^{24}Mg(α,α') inelastic, $E_x = 6.43$ MeV (0_2^+), $E_\alpha = 386$ MeV

$\theta_{c.m.}$ (deg)	$d\sigma/d\Omega$ (mb/sr)	error (mb/sr)
2.2	1.83×10^{1}	9.3×10^{-1}
2.7	6.84	3.5×10^{-1}
3.2	1.62	8.7×10^{-2}
3.6	1.41	7.7×10^{-2}
3.7	1.76	1.1×10^{-1}
4.1	4.24	2.7×10^{-1}
4.6	8.17	4.9×10^{-1}
5.1	8.27	4.7×10^{-1}
5.1	8.50	4.4×10^{-1}
5.6	7.51	3.9×10^{-1}
6.1	5.52	2.9×10^{-1}
6.5	3.17	1.7×10^{-1}
6.9	1.74	9.3×10^{-2}
7.4	1.07	5.9×10^{-2}
7.8	1.04	5.7×10^{-2}
8.3	1.55	8.4×10^{-2}
8.6	1.90	1.0×10^{-1}
9.1	2.11	1.1×10^{-1}
9.6	1.93	1.0×10^{-1}
10.0	1.46	7.9×10^{-2}
10.4	1.09	5.9×10^{-2}
10.8	6.70×10^{-1}	3.8×10^{-2}
11.3	3.60×10^{-1}	2.1×10^{-2}
11.8	3.00×10^{-1}	1.7×10^{-2}

Table A.68: ^{24}Mg(α,α') inelastic, $E_x = 7.35$ MeV (2_3^+), $E_\alpha = 386$ MeV

$\theta_{c.m.}$ (deg)	$d\sigma/d\Omega$ (mb/sr)	error (mb/sr)
0.7	7.18	2.5×10^{-1}
1.0	6.54	2.6×10^{-1}
2.4	5.19	2.4×10^{-1}
2.8	7.85	2.4×10^{-1}
3.3	8.76	2.5×10^{-1}
3.8	1.01×10^{1}	2.7×10^{-1}
3.5	1.07×10^{1}	3.4×10^{-1}
4.0	1.02×10^{1}	3.8×10^{-1}
4.5	9.53	4.3×10^{-1}
4.9	7.42	5.5×10^{-1}
5.3	6.51	4.0×10^{-1}
5.7	3.33	5.1×10^{-1}
6.2	1.14	1.3×10^{-1}
6.7	7.31×10^{-1}	9.7×10^{-2}
7.0	4.95×10^{-1}	7.0×10^{-2}
7.5	1.16	8.8×10^{-2}
8.0	1.50	2.0×10^{-1}
8.4	1.95	1.1×10^{-1}
8.8	1.96	4.7×10^{-2}
9.3	1.43	3.7×10^{-2}
9.7	9.40×10^{-1}	3.0×10^{-2}
10.2	5.18×10^{-1}	2.2×10^{-2}
10.6	3.14×10^{-1}	1.8×10^{-2}
11.0	2.40×10^{-1}	1.6×10^{-2}
11.5	3.52×10^{-1}	1.9×10^{-2}
12.0	3.29×10^{-1}	2.1×10^{-2}

Table A.69: ^{24}Mg(α,α') inelastic, $E_x = 7.62$ MeV (3_1^-), $E_\alpha = 386$ MeV

$\theta_{c.m.}$ (deg)	$d\sigma/d\Omega$ (mb/sr)	error (mb/sr)
0.7	4.90	2.9×10^{-1}
1.0	6.76	3.3×10^{-1}
2.4	9.91	3.3×10^{-1}
2.8	1.06×10^{1}	2.8×10^{-1}
3.3	1.13×10^{1}	2.8×10^{-1}
3.8	1.18×10^{1}	2.8×10^{-1}
3.5	1.22×10^{1}	3.5×10^{-1}
4.0	1.32×10^{1}	4.4×10^{-1}
4.5	1.59×10^{1}	5.1×10^{-1}
4.9	1.91×10^{1}	6.5×10^{-1}
5.3	2.06×10^{1}	3.3×10^{-1}
5.7	2.03×10^{1}	3.3×10^{-1}
6.2	1.89×10^{1}	3.2×10^{-1}
6.7	1.53×10^{1}	2.9×10^{-1}
7.0	1.30×10^{1}	2.1×10^{-1}
7.5	9.79	1.9×10^{-1}
8.0	6.35	1.6×10^{-1}
8.4	3.95	1.4×10^{-1}
8.8	2.16	8.7×10^{-2}
9.3	1.77	6.4×10^{-2}
9.7	1.98	2.1×10^{-1}
10.2	2.63	8.9×10^{-2}
10.6	3.29	8.9×10^{-2}
11.0	3.70	8.1×10^{-2}
11.5	3.77	8.3×10^{-2}
12.0	3.65	7.7×10^{-2}

Table A.70: ^{24}Mg(α,α') inelastic, $E_x = 8.36$ MeV (3_2^-), $E_\alpha = 386$ MeV

$\theta_{c.m.}$ (deg)	$d\sigma/d\Omega$ (mb/sr)	error (mb/sr)
0.7	4.57	2.3×10^{-1}
1.0	5.47	2.8×10^{-1}
2.4	7.10	3.1×10^{-1}
2.8	8.94	3.0×10^{-1}
3.3	1.18×10^{1}	3.3×10^{-1}
3.8	1.53×10^{1}	3.7×10^{-1}
3.5	1.51×10^{1}	5.0×10^{-1}
4.0	2.18×10^{1}	7.0×10^{-1}
4.5	2.65×10^{1}	7.4×10^{-1}
4.9	3.01×10^{1}	9.0×10^{-1}
5.3	3.29×10^{1}	5.6×10^{-1}
5.7	3.12×10^{1}	5.3×10^{-1}
6.2	2.89×10^{1}	5.2×10^{-1}
6.7	2.14×10^{1}	5.4×10^{-1}
7.0	1.86×10^{1}	3.2×10^{-1}
7.5	1.30×10^{1}	2.5×10^{-1}
8.0	7.46	1.9×10^{-1}
8.4	5.01	1.6×10^{-1}
8.8	3.67	7.0×10^{-2}
9.3	3.73	6.7×10^{-2}
9.7	4.30	7.3×10^{-2}
10.2	4.79	7.7×10^{-2}
10.6	4.67	8.9×10^{-2}
11.0	4.47	8.5×10^{-2}
11.5	3.62	7.6×10^{-2}
12.0	2.82	6.8×10^{-2}

Table A.71: ^{24}Mg(α,α') inelastic, $E_x = 9.00$ MeV (2^+_5), $E_\alpha = 386$ MeV

$\theta_{c.m.}$ (deg)	$d\sigma/d\Omega$ (mb/sr)	error (mb/sr)
0.8	9.2×10^{-1}	1.2×10^{-1}
1.0	1.30	1.2×10^{-1}
2.4	1.84	1.4×10^{-1}
2.8	2.39	1.3×10^{-1}
3.3	3.20	1.6×10^{-1}
3.8	3.37	1.6×10^{-1}
3.5	3.88	2.1×10^{-1}
4.0	4.24	2.6×10^{-1}
4.5	3.77	2.4×10^{-1}
4.9	2.78	2.7×10^{-1}
5.3	2.24	2.4×10^{-1}
5.7	1.57	1.0×10^{-1}
6.2	8.57×10^{-1}	7.8×10^{-2}
6.7	7.34×10^{-1}	7.6×10^{-2}
7.0	6.13×10^{-1}	5.0×10^{-2}
7.5	5.72×10^{-1}	4.8×10^{-2}
8.0	5.80×10^{-1}	4.8×10^{-2}
8.4	6.14×10^{-1}	4.9×10^{-2}
8.8	5.85×10^{-1}	2.6×10^{-2}
9.3	4.67×10^{-1}	2.2×10^{-2}
9.7	3.77×10^{-1}	2.0×10^{-2}
10.2	2.15×10^{-1}	1.5×10^{-2}
10.6	2.06×10^{-1}	1.6×10^{-2}
11.0	1.68×10^{-1}	1.4×10^{-2}
11.5	1.07×10^{-1}	1.2×10^{-2}
12.0	1.17×10^{-1}	1.2×10^{-2}

Table A.72: ^{24}Mg(α,α') inelastic, $E_x = 9.15$ MeV (1^-_1), $E_\alpha = 386$ MeV

$\theta_{c.m.}$ (deg)	$d\sigma/d\Omega$ (mb/sr)	error (mb/sr)
0.8	5.6×10^{-1}	1.1×10^{-1}
1.0	5.78×10^{-1}	9.4×10^{-2}
2.4	8.3×10^{-1}	1.0×10^{-1}
2.8	9.96×10^{-1}	9.7×10^{-2}
3.3	9.63×10^{-1}	8.9×10^{-2}
3.8	1.17	1.0×10^{-1}
3.5	1.18	1.3×10^{-1}
4.0	7.9×10^{-1}	1.4×10^{-1}
4.5	6.1×10^{-1}	1.3×10^{-1}
4.9	1.1×10^{-1}	1.5×10^{-1}
5.3	1.3×10^{-1}	2.1×10^{-1}
5.7	2.07×10^{-1}	6.1×10^{-2}
6.2	1.78×10^{-1}	5.1×10^{-2}
6.7	1.31×10^{-1}	4.5×10^{-2}
7.0	9.9×10^{-2}	2.8×10^{-2}
7.5	1.20×10^{-1}	2.9×10^{-2}
8.0	1.87×10^{-1}	3.3×10^{-2}
8.4	2.60×10^{-1}	3.7×10^{-2}
8.8	2.11×10^{-1}	1.8×10^{-2}
9.3	1.32×10^{-1}	1.3×10^{-2}
9.7	1.08×10^{-1}	1.2×10^{-2}
10.2	1.30×10^{-1}	1.3×10^{-2}
10.6	3.03×10^{-2}	8.9×10^{-3}
11.0	3.58×10^{-2}	8.4×10^{-3}
11.5	6.70×10^{-2}	9.8×10^{-3}
12.0	7.8×10^{-2}	1.1×10^{-2}

Table A.73: ^{24}Mg(α,α') inelastic, $E_x = 9.31$ MeV (0_3^+), $E_\alpha = 386$ MeV

$\theta_{c.m.}$ (deg)	$d\sigma/d\Omega$ (mb/sr)	error (mb/sr)
0.8	1.84×10^{1}	3.9×10^{-1}
1.0	1.69×10^{1}	3.7×10^{-1}
2.4	3.09	1.7×10^{-1}
2.8	9.20×10^{-1}	8.5×10^{-2}
3.3	4.74×10^{-1}	6.3×10^{-2}
3.8	1.29	1.0×10^{-1}
3.5	7.8×10^{-1}	1.0×10^{-1}
4.0	1.88	1.6×10^{-1}
4.5	2.75	2.0×10^{-1}
4.9	2.67	2.1×10^{-1}
5.3	2.20	2.4×10^{-1}
5.7	1.92	1.1×10^{-1}
6.2	8.98×10^{-1}	7.9×10^{-2}
6.7	5.23×10^{-1}	6.4×10^{-2}
7.0	5.26×10^{-1}	4.6×10^{-2}
7.5	6.22×10^{-1}	5.0×10^{-2}
8.0	8.71×10^{-1}	5.8×10^{-2}
8.4	1.12	6.6×10^{-2}
8.8	1.44	3.9×10^{-2}
9.3	1.33	3.6×10^{-2}
9.7	1.09	3.3×10^{-2}
10.2	7.42×10^{-1}	2.7×10^{-2}
10.6	5.81×10^{-1}	2.5×10^{-2}
11.0	4.32×10^{-1}	2.2×10^{-2}
11.5	3.48×10^{-1}	1.9×10^{-2}
12.0	3.95×10^{-1}	2.1×10^{-2}

Table A.74: ^{28}Si(α,α') inelastic, $E_x = 1.78$ MeV (2_1^+), $E_\alpha = 386$ MeV

$\theta_{c.m.}$ (deg)	$d\sigma/d\Omega$ (mb/sr)	error (mb/sr)
2.2	1.78×10^{2}	9.7
2.7	1.82×10^{2}	9.9
3.1	2.24×10^{2}	1.2×10^{1}
3.5	2.64×10^{2}	1.4×10^{1}
3.6	2.85×10^{2}	1.5×10^{1}
4.0	3.27×10^{2}	1.7×10^{1}
4.5	3.24×10^{2}	1.7×10^{1}
4.9	2.93×10^{2}	1.6×10^{1}
5.1	2.88×10^{2}	1.5×10^{1}
5.6	2.19×10^{2}	1.2×10^{1}
6.0	1.41×10^{2}	7.8
6.5	8.30×10^{1}	4.8

Table A.75: ^{28}Si(α,α') inelastic, $E_x = 4.98$ MeV (0_2^+), $E_\alpha = 386$ MeV

$\theta_{c.m.}$ (deg)	$d\sigma/d\Omega$ (mb/sr)	error (mb/sr)
2.2	1.77×10^{1}	1.0
2.7	6.60	4.2×10^{-1}
3.1	1.80	1.4×10^{-1}
3.5	2.40	1.9×10^{-1}
3.6	2.70	2.1×10^{-1}
4.0	5.90	3.9×10^{-1}
4.5	9.40	5.7×10^{-1}
4.9	1.03×10^{1}	6.2×10^{-1}
5.1	1.02×10^{1}	6.2×10^{-1}
5.6	9.20	5.6×10^{-1}
6.0	5.90	3.8×10^{-1}
6.5	2.60	1.8×10^{-1}

Table A.76: ^{40}Ca(α, α') inelastic, $E_x = 3.74$ MeV (3_1^-), $E_\alpha = 386$ MeV

$\theta_{c.m.}$ (deg)	$d\sigma/d\Omega$ (mb/sr)	error (mb/sr)
2.1	7.51×10^{1}	4.4
2.6	8.55×10^{1}	5.0
3.0	8.56×10^{1}	5.1
3.3	1.09×10^{2}	6.4
3.4	1.12×10^{2}	6.5
3.8	1.36×10^{2}	7.8
4.3	1.56×10^{2}	8.9
4.7	1.78×10^{2}	1.0×10^{1}
4.9	1.84×10^{2}	1.0×10^{1}
5.3	1.79×10^{2}	1.0×10^{1}
5.8	1.60×10^{2}	9.1
6.2	1.12×10^{2}	6.5

Table A.77: ^{40}Ca(α, α') inelastic, $E_x = 3.90$ MeV (2_1^+), $E_\alpha = 386$ MeV

$\theta_{c.m.}$ (deg)	$d\sigma/d\Omega$ (mb/sr)	error (mb/sr)
2.1	2.50×10^{1}	1.6
2.6	3.29×10^{1}	2.1
3.0	4.08×10^{1}	2.6
3.3	5.35×10^{1}	3.4
3.4	5.97×10^{1}	3.7
3.8	6.38×10^{1}	3.9
4.3	6.36×10^{1}	3.9
4.7	4.46×10^{1}	2.8
4.9	4.59×10^{1}	2.9
5.3	2.66×10^{1}	1.8
5.8	1.50×10^{1}	1.1
6.2	8.38	6.7×10^{-1}

References

[1] H. J. Lu, S. Brandenburg, R. De Leo, M. N. Harakeh, T. D. Poelhekken, and A. van der Woude, Phys. Rev. C **33**, 1116 (1986).

[2] M. M. Sharma, W. T. Borghols, S. Brandenburg, S. Crona, A. Van Der Woude, and M. N. Harakeh, Phys. Rev C **38**, 2562 (1988).

[3] D. H. Youngblood, Y.-W. Lui, and H. L. Clark, Phys. Rev. C **55**, 2811 (1997).

[4] D. H. Youngblood, Y.-W. Lui, and H. L. Clark, Phys. Rev. C **60**, 014304 (1999).

[5] D. H. Youngblood, H. L. Clark, and Y.-W. Lui, Phys. Rev. Lett. **82**, 691 (1999).

[6] M. Uchida, H. Sakaguchi, M. Itoh, M. Yosoi, T. Kawabata, Y. Yasuda, H. Takeda, T. Murakami, S. Terashima, S. Kishi, U. Garg, P. Boutachkov, M. Hedden, B. Kharraja, M. Koss, B. K. Nayak, S. Zhu, M. Fujiwara, H. Fujimura, H. P. Yoshida, K. Hara, H. Akimune, and M. N. Harakeh, Phys. Rev. C **69**, 051301 (2004).

[7] T. Li, U. Garg, Y. Liu, R. Marks, B. K. Nayak, P. V. M. Rao, M. Fujiwara, H. Hashimoto, K. Kawase, K. Nakanishi, S. Okumura, M. Yosoi, M. Itoh, M. Ichikawa, R. Matsuo, T. Terazono, M. Uchida, T. Kawabata, H. Akimune, Y. Iwao, T. Murakami, H. Sakaguchi, S. Terashima, Y. Yasuda, J. Zenihiro, and M. N. Harakeh, Phys. Rev. Lett. **99**, 162503 (2007).

[8] Y. K. Gupta, U. Garg, J. Hoffman, J. Matta, P. V. M. Rao, D. Patel, T. Peach, K. Yoshida, M. Itoh, M. Fujiwara, K. Hara, H. Hashimoto, K. Nakanishi, M. Yosoi, H. Sakaguchi, S. Terashima, S. Kishi, T. Murakami, M. Uchida, Y. Yasuda, H. Akimune, T. Kawabata, and M. N. Harakeh, Phys. Rev. C **93**, 044324 (2016).

[9] T. Peach, U. Garg, Y. K. Gupta, J. Hoffman, J. T. Matta, D. Patel, P. V. M. Rao, K. Yoshida, M. Itoh, M. Fujiwara, K. Hara, H. Hashimoto, K. Nakanishi,

M. Yosoi, H. Sakaguchi, S. Terashima, S. Kishi, T. Murakami, M. Uchida, Y. Yasuda, H. Akimune, T. Kawabata, M. N. Harakeh, and G. Colò, Phys. Rev. C **93**, 064325 (2016).

[10] M. Itoh, H. Sakaguchi, M. Uchida, T. Ishikawa, T. Kawabata, T. Murakami, H. Takeda, T. Taki, S. Terashima, N. Tsukahara, Y. Yasuda, M. Yosoi, U. Garg, M. Hedden, B. Kharraja, M. Koss, B. K. Nayak, S. Zhu, H. Fujimura, M. Fujiwara, K. Hara, H. P. Yoshida, H. Akimune, M. N. Harakeh, and M. Volkerts, Phys. Lett. B **549**, 58 (2002).

[11] T. Kawabata, T. Adachi, M. Fujiwara, K. Hatanaka, Y. Ishiguro, M. Itoh, Y. Maeda, H. Matsubara, H. Miyasako, Y. Nozawa, T. Saito, S. Sakaguchi, Y. Sasamoto, Y. Shimizu, T. Takahashi, A. Tamii, S. Terashima, H. Tokieda, N. Tomida, T. Uesaka, M. Uchida, Y. Yasuda, N. Yokota, H. P. Yoshida, and J. Zenihiro, J. Phys. Conf. Ser. **321**, 012012 (2011).

[12] T. Wakasa, E. Ihara, K. Fujita, Y. Funaki, K. Hatanaka, H. Horiuchi, M. Itoh, J. Kamiya, G. Röpke, H. Sakaguchi, N. Sakamoto, Y. Sakemi, P. Schuck, Y. Shimizu, M. Takashina, S. Terashima, A. Tohsaki, M. Uchida, H. P. Yoshida, and M. Yosoi, Phys. Lett. B **653**, 173 (2007).

[13] Y. Sasamoto, T. Kawabata, T. Uesaka, K. Suda, Y. Maeda, S. Sakaguchi, K. Itoh, K. Hatanaka, M. Fujiwara, A. Tamii, Y. Shimizu, K. Nakanishi, K. Kawase, H. Hashimoto, Y. Tameshige, H. Matsubara, M. Itoh, H. P. Yoshida, and M. Uchida, Mod. Phys. Lett. A **21**, 2393 (2006).

[14] J. Heisenberg and H. P. Blok, Ann. Rev. Nucl. Part. Sci. **33**, 569 (1983).

[15] M. N. Harakeh and A. van der Woude, *Giant Resonaces : Fundamental High-Freaquency Modes of Nuclear Excitation* (Oxford Univ. Press, 2001).

[16] M. Itoh, H. Akimune, M. Fujiwara, U. Garg, N. Hashimoto, T. Kawabata, K. Kawase, S. Kishi, T. Murakami, K. Nakanishi, Y. Nakatsugawa, B. K. Nayak, S. Okumura, H. Sakaguchi, H. Takeda, S. Terashima, M. Uchida, Y. Yasuda, M. Yosoi, and J. Zenihiro, Phys. Rev. C **84**, 054308 (2011).

[17] M. Itoh, S. Kishi, H. Sakaguchi, H. Akimune, M. Fujiwara, U. Garg, K. Hara, H. Hashimoto, J. Hoffman, T. Kawabata, K. Kawase, T. Murakami, K. Nakanishi,

B. K. Nayak, S. Terashima, M. Uchida, Y. Yasuda, and M. Yosoi, Phys. Rev. C **88**, 064313 (2013).

[18] M. Uchida, *Isoscalar giant dipole resonance and nuclear incompressibility*, Ph.D. thesis, Kyoto University (2003).

[19] M. Uchida, H. Sakaguchi, M. Itoh, M. Yosoi, T. Kawabata, H. Takeda, Y. Yasuda, T. Murakami, T. Ishikawa, T. Taki, N. Tsukahara, S. Terashima, U. Garg, M. Hedden, B. Kharraja, M. Koss, B. K. Nayak, S. Zhu, M. Fujiwara, H. Fujimura, K. Hara, E. Obayashi, H. P. Yoshida, H. Akimune, M. N. Harakeh, and M. Volkerts, Phys. Lett. B **557**, 12 (2003).

[20] B. John, Y. Tokimoto, Y.-W. Lui, H. L. Clark, X. Chen, and D. H. Youngblood, Phys. Rev. C **68**, 014305 (2003).

[21] H. Sagawa, S. Yoshida, G. M. Zeng, J. Z. Gu, and X. Z. Zhang, Phys. Rev. C **76**, 2 (2007), 0706.0966 .

[22] J. P. Blaizot, Phys. Rep. **64**, 171 (1980).

[23] J. P. Blaizot, J. F. Berger, J. Dechargé, and M. Girod, Nucl. Phys. A **591**, 435 (1995).

[24] G. Colò, U. Garg, and H. Sagawa, Eur. Phys. J. A **50**, 1 (2014), arXiv:arXiv:1209.0681v1 .

[25] G. Colò, N. Van Giai, J. Meyer, K. Bennaceur, and P. Bonche, Phys. Rev. C **70**, 1 (2004).

[26] B. G. Todd-Rutel and J. Piekarewicz, Phys. Rev. Lett. **95**, 1 (2005), arXiv:0504034 [nucl-th] .

[27] J. Piekarewicz, Eur. Phys. J. A **50**, 25 (2014).

[28] Y. K. Gupta, U. Garg, K. B. Howard, J. T. Matta, M. enyiit, M. Itoh, S. Ando, T. Aoki, A. Uchiyama, S. Adachi, M. Fujiwara, C. Iwamoto, A. Tamii, H. Akimune, C. Kadono, Y. Matsuda, T. Nakahara, T. Furuno, T. Kawabata, M. Tsumura, M. N. Harakeh, and N. Kalantar-Nayestanaki, Phys. Lett. Sec. B **760**, 482 (2016), arXiv:arXiv:1607.02198v1 .

[29] S. Bagchi, J. Gibelin, M. N. Harakeh, N. Kalantar-Nayestanaki, N. L. Achouri, H. Akimune, B. Bastin, K. Boretzky, H. Bouzomita, M. Caamaño, L. Càceres, S. Damoy, F. Delaunay, B. Fernández-Domínguez, M. Fujiwara, U. Garg, G. F. Grinyer, O. Kamalou, E. Khan, A. Krasznahorkay, G. Lhoutellier, J. F. Libin, S. Lukyanov, K. Mazurek, M. A. Najafi, J. Pancin, Y. Penionzhkevich, L. Perrot, R. Raabe, C. Rigollet, T. Roger, S. Sambi, H. Savajols, M. Senoville, C. Stodel, L. Suen, J. C. Thomas, M. Vandebrouck, and J. Van de Walle, Phys. Lett. B **751**, 371 (2015).

[30] M. Vandebrouck, J. Gibelin, E. Khan, N. L. Achouri, H. Baba, D. Beaumel, Y. Blumenfeld, M. Caamaño, L. Càceres, G. Colò, F. Delaunay, B. Fernandez-Dominguez, U. Garg, G. F. Grinyer, M. N. Harakeh, N. Kalantar-Nayestanaki, N. Keeley, W. Mittig, J. Pancin, R. Raabe, T. Roger, P. Roussel-Chomaz, H. Savajols, O. Sorlin, C. Stodel, D. Suzuki, and J. C. Thomas, Phys. Rev. C **92**, 024316 (2015).

[31] G. Gamow, Proc. Roy. Soc. A **126**, 632 (1930).

[32] D. M. Brink, J. Phys. Conf. Ser. **111**, 012001 (2008).

[33] D. Brink, *Proc. International School of Physics "Enrico Fermi" course 36(1965)*, edited by C. Bloch (Academic Press, 1966) p. 247.

[34] H. Margenau, Phys. Rev. **59**, 37 (1941).

[35] K. Ikeda, N. Takigawa, and H. Horiuchi, Prog. Theor. Phys. Suppl. **E68**, 464 (1968).

[36] M. Freer and H. O. U. Fynbo, Prog. Part. Nucl. Phys. **78**, 1 (2014).

[37] F. Hoyle, Astrophys. J. Suppl. Ser. **1**, 121 (1954).

[38] H. Morinaga, Phys. Rev. **101**, 254 (1956).

[39] H. Morinaga, Phys. Lett. **21**, 78 (1966).

[40] M. Kamimura, Nucl. Phys. A **351**, 456 (1981).

[41] R. De Leo, G. D'Erasmo, A. Pantaleo, M. N. Harakeh, E. Cereda, S. Micheletti, and M. Pignanelli, Phys. Rev. C **28**, 1443 (1983).

[42] H. O. U. Fynbo, C. A. Diget, U. C. Bergmann, M. J. G. Borge, J. Cederkäll, P. Dendooven, L. M. Fraile, S. Franchoo, V. N. Fedosseev, B. R. Fulton, W. Huang, J. Huikari, H. B. Jeppesen, A. S. Jokinen, P. Jones, B. Jonson, U. Köster, K. Langanke, M. Meister, T. Nilsson, G. Nyman, Y. Prezado, K. Riisager, S. Rinta-Antila, O. Tengblad, M. Turrion, Y. Wang, L. Weissman, K. Wilhelmsen, and J. Äystö, Nature **433**, 136 (2005).

[43] M. Freer, H. Fujita, Z. Buthelezi, J. Carter, R. W. Fearick, S. V. Förtsch, R. Neveling, S. M. Perez, P. Papka, F. D. Smit, J. A. Swartz, and I. Usman, Phys. Rev. C **80**, 041303 (2009).

[44] T. Kawabata, H. Akimune, H. Fujita, Y. Fujita, M. Fujiwara, K. Hara, K. Hatanaka, M. Itoh, Y. Kanada-En'yo, S. Kishi, K. Nakanishi, H. Sakaguchi, Y. Shimbara, A. Tamii, S. Terashima, M. Uchida, T. Wakasa, Y. Yasuda, H. Yoshida, and M. Yosoi, Phys. Lett. B **646**, 6 (2007).

[45] B. F. Bayman and A. Bohr, Nucl. Phys. **9**, 596 (1958).

[46] T. Yamada, Y. Funaki, H. Horiuchi, K. Ikeda, and A. Tohsaki, Prog. Theor. Phys. **120**, 1139 (2008).

[47] P. M. Endt, At. Data Nucl. Data Tables **55**, 171 (1993).

[48] Y. Chiba and M. Kimura, Phys. Rev. C **91**, 061302 (2015).

[49] A. Tohsaki, H. Horiuchi, P. Schuck, and G. Röpke, Phys. Rev. Lett. **87**, 192501 (2001).

[50] Y. Funaki, H. Horiuchi, W. Von Oertzen, G. Röpke, P. Schuck, A. Tohsaki, and T. Yamada, Phys. Rev. C **80**, 1 (2009).

[51] T. Yamada and P. Schuck, Phys. Rev. C **69**, 024309 (2004).

[52] Y. Funaki, H. Horiuchi, A. Tohsaki, P. Schuck, and G. Ropke, Prog. Theor. Phys. **108**, 297 (2002).

[53] L. Pauling, J. Chem. Phys **1**, 280 (1933).

[54] Y. Kanada-En'yo, H. Horiuchi, and A. Doté, Phys Rev. C **60**, 064304 (1999).

[55] Y. Kanada-En'yo, M. Kimura, and A. Ono, Prog. Theor. Exp. Phys. **2012**, 01A202 (2012).

[56] P. Strehl, Z. Phys **234**, 416 (1970).

[57] M. Chernykh, H. Feldmeier, T. Neff, P. von Neumann-Cosel, and A. Richter, Phys. Rev. Lett. **105**, 1 (2010).

[58] D. T. Khoa and D. C. Cuong, Phys. Lett. B **660**, 331 (2007).

[59] N. Anantaraman, H. Toki, and G. F. Bertsch, Nucl. Phys. A **398**, 269 (1983).

[60] G. R. Satchler, Nucl. Phys. A **472**, 215 (1987).

[61] M. N. Harakeh and A. E. L. Dieperink, Phys. Rev. C **23**, 2329 (1981).

[62] M. Fujiwara, H. Akimune, I. Daito, H. Fujimura, Y. Fujita, K. Hatanaka, H. Ikegami, I. Katayama, K. Nagayama, N. Matsuoka, S. Morinobu, T. Noro, M. Yoshimura, H. Sakaguchi, Y. Sakemi, A. Tamii, and M. Yosoi, Nucl. Instrm. Methods Phys. Res., Sect A **422**, 484 (1999).

[63] Y. Fujita, K. Hatanaka, G. P. A. Berg, K. Hosono, N. Matsuoka, S. Morinobu, T. Noro, M. Sato, K. Tamura, and H. Ueno, Nucl. Instrm. Methods Phys Res., Sect A **126**, 274 (1997).

[64] T. Wakasa, K. Hatanaka, Y. Fujita, G. P. A. Berg, H. Fujimura, H. Fujita, M. Itoh, J. Kamiya, T. Kawabata, K. Nagayama, T. Noro, H. Sakaguchi, Y. Shimbara, H. Takeda, K. Tamura, H. Ueno, M. Uchida, M. Uraki, and M. Yosoi, Nucl. Instrm. Methods Phys Res., Sect A **482**, 79 (2002).

[65] H. Fujita, Y. Fujita, G. P. A. Berg, A. D. Bacher, C. C. Foster, K. Hara, K. Hatanaka, T. Kawabata, T. Noro, H. Sakaguchi, Y. Shimbara, T. Shinada, E. J. Stephenson, H. Ueno, and M. Yosoi, Nucl. Instrm. Methods Phys Res., Sect A **484**, 17 (2002).

[66] T. Kawabata, H. Akimune, H. Fujimura, H. Fujita, Y. Fujita, M. Fujiwara, K. Hara, K. Hatanaka, K. Hosono, T. Ishikawa, M. Itoh, J. Kamiya, M. Nakamura, T. Noro, E. Obayashi, H. Sakaguchi, Y. Shimbara, H. Takeda, T. Taki,

A. Tamii, H. Toyokawa, N. Tsukahara, M. Uchida, H. Ueno, T. Wakasa, K. Yamasaki, Y. Yasuda, H. P. Yoshida, and M. Yosoi, Nucl. Instrm. Methods Phys. Res. Sect A **459**, 171 (2001).

[67] H. Matsubara, A. Tamii, Y. Shimizu, K. Suda, Y. Tameshige, and J. Zenihiro, Nucl. Instrm. Methods Phys. Res., Sect A **678**, 122 (2012).

[68] A. Tamii, Y. Fujita, H. Matsubara, T. Adachi, J. Carter, M. Dozono, H. Fujita, K. Fujita, H. Hashimoto, K. Hatanaka, T. Itahashi, M. Itoh, T. Kawabata, K. Nakanishi, S. Ninomiya, A. B. Perez-Cerdan, L. Popescu, B. Rubio, T. Saito, H. Sakaguchi, Y. Sakemi, Y. Sasamoto, Y. Shimbara, Y. Shimizu, F. D. Smit, Y. Tameshige, M. Yosoi, and J. Zenhiro, Nucl. Instrm. Methods Phys. Res., Setc. A **605**, 326 (2009).

[69] H. P. Yoshida, T. Baba, T. Noro, M. Kawabata, H. Akimune, H. Sakaguchi, A. Tamii, H. Takeda, and T. Kawabata, RCNP annual report , 164 (1996).

[70] T. Katabata, H. Sakaguchi, A. Tamii, H. Takeda, T. Taki, and H. Yoshida, RCNP annual report , 161 (1996).

[71] M. Itoh, H. Sakaguchi, M. Uchida, T. Ishikawa, T. Kawabata, T. Murakami, H. Takeda, T. Taki, S. Terashima, N. Tsukahara, Y. Yasuda, M. Yosoi, U. Garg, M. Hedden, B. Kharraja, M. Koss, B. K. Nayak, S. Zhu, H. Fujimura, M. Fujiwara, K. Hara, H. P. Yoshida, H. Akimune, M. N. Harakeh, and M. Volkerts, Phys. Rev. C **68**, 064602 (2003).

[72] P. M. Endt, At. Data Nucl. Data Tables **23**, 3 (1979).

[73] P. M. Endt, Nucl. Phys. A **521**, 1 (1990).

[74] D. R. Tilley, H. R. Weller, and C. M. Chevesyc, Nucl. Phys. A **565**, 1 (1993).

[75] D. R. Tilley, C. M. Cheves, J. H. Kelley, S. Raman, and H. R. Weller, Nucl. Phys. A **636**, 249 (1998).

[76] J. Kelley, J. Purcell, and C. Sheu, Nuclear Physics A **968**, 71 (2017).

[77] J. Raynal, "Computer Program : ECIS-95," (1995), old version of ECIS-12 NEA-0850/19.

[78] G. R. Satchler and D. T. Khoa, Phys. Rev. C **55**, 285 (1997).

[79] H. De Vries, C. W. De Jager, and C. De Vries, At. Data Nucl. Data Tables **36**, 495 (1987).

[80] E. A. Knight, R. P. Singhal, R. G. Arthur, and M. W. S. Macauley, J. Phys. G : Nucl. Phys. **7**, 1115 (1981).

[81] J. J. Kelly, Phys. Rev. C **70**, 0682021 (2004).

[82] S. Terashima, *Systematic study of neutron density distributions of Sn isotopes by proton elastic scattering*, Ph.D. thesis, Kyoto University (2008).

[83] S. Terashima, H. Sakaguchi, H. Takeda, T. Ishikawa, M. Itoh, T. Kawabata, T. Murakami, M. Uchida, Y. Yasuda, M. Yosoi, J. Zenihiro, H. P. Yoshida, T. Noro, T. Ishida, S. Asaji, and T. Yonemura, Phys. Rev. C **77**, 1 (2008).

[84] R. G. Sachs, Phys. Rev. **126**, 2256 (1962).

[85] "Computer program : unfold," Unpublished.

[86] L. E. Price, J. R. Dunning, M. Goitein, K. Hanson, T. Kirk, and R. Wilson, Phys. Rev. D **4**, 45 (1971).

[87] G. G. Simon, C. Schmitt, F. Borkowski, and V. H. Walther, Nucl. Phys. A **333**, 381 (1980).

[88] L. Andivahis, P. E. Bosted, A. Lung, L. M. Stuart, J. Alster, R. G. Arnold, C. C. Chang, F. S. Dietrich, W. Dodge, R. Gearhart, J. Gomez, K. A. Grikoen, R. S. Hicks, C. E. Hyde-Wright, C. Keppel, S. E. Kuhn, J. Lichtenstadt, R. A. Miskimen, G. A. Peterson, G. G. Petratos, S. E. Rock, S. Rokni, W. K. Sakumoto, M. Spengos, K. Swartz, Z. Szalata, and L. H. Tao, Phys. Rev. D **50**, 5491 (1994).

[89] G. R. Satchler, Nucl. Phys. A **195**, 1 (1972).

[90] G. R. Satchler, Nucl. Phys. A **3**, 596 (1974).

[91] G. R. Satchler, *Direct nuclear reaction* (Oxford Univ. Press, 1983).

[92] M. Takashina and Y. Sakuragi, Phys. Rev. C **74**, 054606 (2006).

[93] M. Takashina, Phys. Rev. C **78**, 014602 (2008).

[94] M. Tomita, M. Iwasaki, R. Otani, and M. Ito, in *proceedings of "The 26th International Nuclear Physics Conference" PoS(INPC2016)210* (2016).

[95] B. Bonin, N. Alamanos, B. Berthier, G. Bruge, H. Faraggi, J. C. Lugol, W. Mittig, L. Papineau, A. I. Yavin, J. Arvieux, L. Farvacque, M. Buenerd, and W. Bauhoff, Nucl. Phys. A **445**, 381 (1985).

[96] K. Minomo and K. Ogata, Phys. Rev. C **93**, 051601 (2016).

[97] Y. Funaki, A. Tohsaki, H. Horiuchi, P. Schuck, and G. Röpke, Eur. Phys. J. A **24**, 321 (2005), 0410097 .

[98] Y. Funaki, A. Tohsaki, H. Horiuchi, P. Schuck, and G. Röpke, Eur. Phys. J. A **28**, 259 (2006), 0601035 .

[99] K. Amos, P. J. Dortmans, H. V. von Geramb, S. Karataglidis, and J. Raynal, *in Advanced Nucler Physics*, edited by J. W. Negele and E. Vogt, Vol. 25 (Plenum, New York, 2000) p. 275.

[100] E. Uegaki, S. Okabe, Y. Abe, and H. Tanaka, Prog. Theor. Phys. **57**, 1262 (1977).

List of Tables